



**DESIGN OF A LIGHTER THAN AIR VEHICLE THAT ACHIEVES POSITIVE  
BUOYANCY IN AIR USING A VACUUM**

THESIS

Trent T. Metlen, Captain, USMC

AFIT-ENY-13-J-02

**DEPARTMENT OF THE AIR FORCE  
AIR UNIVERSITY**

***AIR FORCE INSTITUTE OF TECHNOLOGY***

**Wright-Patterson Air Force Base, Ohio**

APPROVED FOR PUBLIC RELEASE; DISTRIBUTION UNLIMITED

The views expressed in this thesis are those of the author and do not reflect the official policy or position of the United States Air Force, Department of Defense, or the United States Government.

AFIT-ENY-13-J-02

**DESIGN OF A LIGHTER THAN AIR VEHICLE THAT ACHIEVES POSITIVE  
BUOYANCY IN AIR USING A VACUUM**

THESIS

Presented to the Faculty

Department of Aeronautics and Astronautics

Graduate School of Engineering and Management

Air Force Institute of Technology

Air University

Air Education and Training Command

In Partial Fulfillment of the Requirements for the  
Degree of Master of Science in Aeronautical Engineering

Trent T. Metlen, BS

Captain, USMC

June 2012

APPROVED FOR PUBLIC RELEASE; DISTRIBUTION UNLIMITED.

**DESIGN OF A LIGHTER THAN AIR VEHICLE THAT ACHIEVES POSITIVE  
BUOYANCY IN AIR USING A VACUUM**

Trent T. Metlen, BS  
Captain, USMC

Approved:

\_\_\_\_\_  
Dr. Anthony Palazotto (Chairman)

\_\_\_\_\_  
Date

\_\_\_\_\_  
Dr. Jeremy Agte, Lt Col, USAF (Member)

\_\_\_\_\_  
Date

\_\_\_\_\_  
Dr. Mark Reeder (Member)

\_\_\_\_\_  
Date

## Abstract

Three designs for a Lighter Than Air (LTA) structure that achieve positive buoyancy using a vacuum in place of a lifting gas were proposed and evaluated. Before the first human flight it was predicted that LTA flight was possible through the use of a light weight structure maintaining an internal vacuum. Since that time LTA flight has been used to accomplish various missions through the use of lifting gases. This study was conducted in response to an anticipated shortage of helium, the danger of hydrogen, and the possibility of using LTA vehicles as a means of passenger or cargo transportation. The improvements required of traditional LTA vehicles to become viable methods of transportation were examined and found to be buoyancy control, ground handling, and efficiency. Efficiency was evaluated using von Karman efficiency which enabled comparison between vehicles of different types and missions based on velocity, payload and power required. Von Karman efficiency was also used to compare theoretical LTA vehicles of constant size over a range of engine sizes. Vacuum LTA structures were evaluated based on their ratio of structure weight to the weight of displaced air and termed Weight/Buoyant Force ( $W/B$ ) where a  $W/B < 1$  corresponds to positive buoyancy.

Two methods of geometrically stiffening a sphere were investigated. A thin shelled sphere stiffened with an isogrid of blade type stiffeners using Ultra High Modulus (UHM) carbon epoxy was predicted to give a  $W/B = 0.81$  which would enable LTA flight. The same design with a beryllium skin and UHM carbon epoxy stiffeners was predicted to have a  $W/B = 0.79$ . A geodesic sphere composed of a frame of cylindrical, UHM, carbon epoxy, pultruded rods with a thin membrane stretched over it was evaluated using

Finite Element Analysis with the frame modeled as clamped, cylindrical beam elements. A  $W/B=0.57$  was calculated for the frame. The skin was predicted to add approximately 0.37 to the  $W/B$  if Zylon was used to reinforce a Mylar membrane, which would result in a structure with an overall  $W/B=0.94$ . If a material as strong as graphene were used for the skin the skin would have a  $W/B=0.001$ , resulting in an overall  $W/B=0.57$ . These structures were optimized using a non-linear programming optimization routine in Matlab.

A unique LTA vehicle concept composed of twin counter-rotating cylinders that made use of a virtual elliptical body to reduce drag and maintain structural integrity with a vacuum was also investigated and found to be infeasible.

*To my beautiful wife and adorable son, who's love and support made it possible for me to lock myself in my office for days at a time to complete research, course work, and professional work, and still have a family when I emerged. To God, for all the miraculous coincidences that make life fall perfectly into place.*

## **Acknowledgments**

Thank you Dr. Anthony Palazotto, for the long hours you spent grading and prepping classes, reviewing my research and helping me put it together in a way that made sense. I suspect you remember more than you forgot, and that you forgot more than most of us will ever know about engineering. Thank you for listening to my wild ideas and for encouraging me to research them. Thank you LtCol Jeremy Agte for greatly contributing to my understanding of engineering and for giving me the tools to complete this project. Thank you Matt Johnson for being the creative and financial spark behind this research, who refused to listen to those of us that advised a more conventional approach, and for daring to explore the regions outside of the proverbial box. Thank you Dr. David Stargel, for taking an interest in our research and providing much needed funding. For the professionals at AFRL and NASA; in particular George Studor, thank you for your time, interest, and support for our project.

Trent T. Metlen

## Table of Contents

	Page
Abstract.....	iv
Acknowledgments.....	vii
Table of Contents.....	viii
List of Figures.....	x
List of Tables.....	xiii
Nomenclature.....	xiv
I. Introduction.....	1
1.1 Motivation.....	1
1.2 Background.....	2
1.3 Research Objective.....	4
1.4 Thesis Overview.....	6
II. Literature Review.....	7
2.1 Chapter Overview.....	7
2.2 Historical LTA Vehicles.....	8
2.2.1 <i>Airship Structures</i> .....	8
2.2.2 <i>Missions</i> .....	14
2.2.3 <i>Design Challenges</i> .....	15
2.3 Thin Shelled Sphere.....	34
2.4 Isogrid.....	45
2.5 Geodesic Sphere.....	45
2.6 Summary.....	53
III. Methodology.....	54
3.1 Chapter Overview.....	54
3.2 Rotating Cylinder Vacuum LTA Vehicle Concept.....	54
3.2.1 <i>Buoyancy and Weight</i> .....	56
3.2.2 <i>Aerodynamics</i> .....	62
3.2.3 <i>Power Requirements</i> .....	64
3.2.4 <i>Engine and Fuel Weight</i> .....	67
3.3 Isogrid Stiffened Sphere.....	70
3.4 Geodesic Sphere.....	75
3.4.1 <i>Geometry</i> .....	84

3.4.2 Optimization .....	87
3.5 Summary .....	90
IV. Analysis and Results .....	90
4.1 Chapter Overview .....	90
4.2 Minor Investigations .....	91
4.3 Rotating Cylinder Vacuum LTA Vehicle .....	96
4.4 Isogrid Stiffened Sphere.....	101
4.5 Geodesic Sphere.....	109
4.6 Potential Missions .....	119
4.7 Summary .....	126
V. Conclusions and Recommendations .....	128
5.1 Chapter Overview .....	128
5.2 Conclusions of Research .....	128
5.3 Significance of Research.....	130
5.4 Recommendations for Future Research .....	130
Appendix A: Matlab Code .....	132
A.1 Optimization Routine (LTA_opt.m) .....	132
A.2 Optimization Sub-Routine: Cost Function (Cost.m).....	133
A.3 Optimization Sub-Routine: Sphere Parameters (Sphere_parameters.m) .....	133
A.4 Optimization Sub-Routine: Constraints (Constraints.m) .....	134
A.5 Optimization Sub-Routine: Finite Element Program .....	134
A.6 Optimization Sub-Routine: Datcreate (Datcreate.m) .....	139
A.7 Optimization Sub-Routine: Geodesic Sphere Geometry (LTAgeod2.m) .....	141
A.8 Optimization Sub-Routine: .dat File Reader (Datread_beam.m).....	147
A.9 Von Karman Efficiency for Rotating Cylinder (LTAheliumcylinder.m) .....	152
A.10 Optimization of Isogrid Stiffened Sphere (LTAsphere.m) .....	156
A.11 Partial Vacuum Study (LTApherepv.m).....	158
A.12 Altitude Effect on W/B (LTApherealt.m) .....	159
A.13 Optimization of Isogrid (LTAisogrid_opt.m) .....	160
A.14 Optimization of Isogrid Sub-Routine: (LTAisogrid_constraints.m).....	161
A.15 Optimization of Isogrid Sub-Routine: (LTAisogrid_cost.m).....	162

## List of Figures

	Page
Figure 1: Lana’s Flying Boat [3] .....	3
Figure 2: USS Shenandoah Rigid Construction [9].....	10
Figure 3: ZMC-2 Metal Clad Airship ca. 1930 [12].....	12
Figure 4: Semirigid, Nonrigid, Rigid Airships [14].....	14
Figure 5: Causes of 29 Helium and 27 Hydrogen Airship Mishaps.....	18
Figure 6: Ground Handling [9] .....	20
Figure 7: Comparison Between Lifting Gases.....	22
Figure 8: Griffith Airfoil [24] .....	26
Figure 9: Von Karman Efficiency of BLC Vehicles .....	29
Figure 10: Buckled Sphere [29].....	36
Figure 11: Prolate Sphere [30].....	38
Figure 12: Laminate Stiffness as a Function of Orientation.....	44
Figure 13: Grid Stiffened Sphere, $f=10$ .....	45
Figure 14: Geodesic Sphere $f=1$ (Icosahedron).....	47
Figure 15: Geodesic Sphere $f=2$ .....	47
Figure 16: Spherical to Cartesian Conversion in Matlab [38].....	48
Figure 17: Icosahedron-Cutting.....	51
Figure 18: Icosahedron-Cut .....	51
Figure 19: Icosahedron-Top View .....	52
Figure 20: Rotating Cylinder Vehicle.....	56
Figure 21: Rotating Cylinder Loads .....	59

Figure 22: Formation of Virtual Elliptical Body at Critical Velocity [45] .....	63
Figure 23: Reduction in Moment and Drag at Critical Rotational Velocity [45] .....	67
Figure 24: Isogrid Geometry [36] .....	70
Figure 25: UHM Carbon Epoxy Isogrid Optimization .....	74
Figure 26: Geodesic Sphere Representation .....	75
Figure 27: Geodesic Sphere – Volume Calculation .....	81
Figure 28: Workflow Diagram .....	84
Figure 29: Geodesic Sphere Generation-Top Pentagon Cap .....	86
Figure 30: Geodesic Sphere Generation-Center Band of 10 Major Triangles .....	87
Figure 31: Effect of Density on W/B .....	92
Figure 32: Effect of Young’s Modulus of Elasticity on W/B .....	93
Figure 33: Effect of Increasing Internal Pressure .....	95
Figure 34: Power Required by RCVLTAV at 75% Drag Torque at 19.8km MSL .....	98
Figure 35: Power Required by RCVLTAV at 1% Drag Torque at 19.8km MSL .....	99
Figure 36: RCVLTAV at 1% Drag Torque at 19.8km MSL .....	100
Figure 37: Beryllium Isogrid Optimization .....	102
Figure 38: UHM Carbon Epoxy Isogrid Optimization .....	105
Figure 39: Isogrid Visualization $f=85$ .....	106
Figure 40: Effect of Geometric Frequency on Run Time .....	110
Figure 41: Effect of Geometric Frequency on Feasible Design Space .....	111
Figure 42: Effect of Geometric Frequency on $\sigma$ .....	112
Figure 43: Graphical Representation of Geodesic Sphere Design Space .....	114
Figure 44: Optimal Geometry for $r_s=0.33$ m Geodesic Sphere .....	115

Figure 45: FEA of Vectran Triangular Plate With Clamped Edges .....	117
Figure 46: Payload Capability for $W/B=0.94$ .....	118
Figure 47: Effect of Increasing Designed Deployment Elevation .....	121
Figure 48: Effect of Altitude on $W/B$ .....	122
Figure 49: Conceptual Design of BLC Vacuum LTA Vehicle [24] .....	123
Figure 50: von Karman Efficiency at $W/B=0.8$ $CD = 0.0169$ .....	124
Figure 51: von Karman Efficiency at $W/B=0.8$ $CD = 0.1$ .....	125

## List of Tables

	Page
Table 1: C-27J Specifications [7] .....	5
Table 2: Research Questions.....	6
Table 3: BLC LTA Vehicle Assumptions .....	33
Table 4: Material Properties-Monocoque Shell.....	43
Table 5: Icosahedron Vertex Locations .....	49
Table 6: Material Properties-Skin.....	76
Table 7: Material Properties-Frame .....	82
Table 8: Rotating Cylinder Vehicle Assumptions .....	97
Table 9: Isogrid Results .....	109
Table 10: Research Questions Revisited.....	128

## Nomenclature

<b>Symbol</b>	<b>Description</b>
$a$	triangle leg length
$a_c$	cylinder area
$a_{circ}$	area of great circle of sphere
$a_g$	gondola cross-sectional area
$a_{gs}$	geodesic sphere surface area
$a_p$	propeller area
$a_s$	sphere area
$a_{skin}$	cross sectional area of sphere skin
$b$	stiffener thickness
BLC	Boundary Layer Control
$C_D$	drag coefficient
$C_{Dc}$	rotating cylinder drag coefficient
$C_{dg}$	gondola drag coefficient
$C_{fb}$	bearing friction coefficient
$C_{m_s}$	spherical endcap rotational drag coefficient
$CP_D$	drag power coefficient
$CP_M$	moment power coefficient
$d$	stiffener depth
$D$	drag force
$D_g$	gondola drag
$E$	Young's modulus of elasticity
$E^*$	stiffness equivalent Young's modulus of elasticity
$e_{VK}$	von Karman efficiency
$f$	geometric frequency of geodesic sphere
$F_a$	axial load on cylinder
$F_b$	bearing load
$F_c$	centripetal force
$F_p$	force due to atmospheric pressure
FEA	Finite Element Analysis
ft	feet
$g$	acceleration due to gravity
$g_1$	material compressive strength constraint
$g_2$	cylindrical beam buckling load constraint
$g_3$	cylindrical beam maximum thickness constraint
$g_4$	cylindrical beam maximum radius constraint

$h$	triangle height
HALED	High Altitude Long Endurance Demonstrator
$I_{cb}$	cylindrical beam area moment of inertia
$k_{ee}$	engine efficiency
kg	kilogram
KIAS	knots indicate air speed
km	kilometers
$k_{pe}$	propeller efficiency
KTAS	knots true air speed
$l$	airship length
lb	pound
$L_b$	buoyant force
$L_{bc}$	buoyant force of cylinder with spherical endcaps
$l_c$	cylinder length
$\bar{l}_{cb}$	average cylindrical beam length
LTA	Lighter Than Air
m	meter
$M$	rotating cylinder drag moment
$m_c$	cylinder mass
$m_e$	engine mass
$m_b$	bearing mass
MB	Mega Bytes
$m_g$	gondola mass
$m_s$	sphere mass
MSL	Mean Sea Level
$n_e$	number of edges
nm	nautical miles
$n_t$	number of triangular faces
$n_v$	number of vertices
$p_a$	atmospheric pressure
$P_b$	power required due to bearing friction
$p_{crit}$	critical pressure
$P_e$	Euler load on cylindrical beam
$P_r$	power required to rotate cylinder
$P_{req}$	power required
$P_s$	power required due to spherical end-cap drag
$P_{tot}$	total power required
$P_x$	power required to maintain translational velocity
$r_b$	bearing radius
$Re$	Reynold's number
$p_{lg}$	pressure of lifting gas
$r$	radius
RAM	Random Access Memory
$r_c$	cylinder radius

$r_{cb}$	cylindrical beam radius
$r_s$	sphere radius
R	specific gas constant
SHP	Shaft Horse Power
T	temperature
$\bar{t}$	smearred skin thickness of isogrid
$t_{cb}$	cylindrical beam thickness
$t^*$	stiffness equivalent thickness
$t_{skin}$	skin thickness
$t_{skin_c}$	cylinder skin thickness
$t_{skin_s}$	sphere skin thickness
$u$	velocity
UHM	Ultra High Modulus
$u_m$	maximum velocity
$u_R$	rotating cylinder surface speed
USS	United States Ship
$v$	volume
$v_c$	volume of cylinder
$v_{gs}$	geodesic sphere volume
$v_s$	volume of sphere
$v_s$	volume of structure
$W$	useful lift
W/B	weight/buoyant force of structure
ZMC	Metal Clad Airship
$\alpha$	non-dimensional value for isogrid calculations see equation (70)
$\beta$	non-dimensional value for isogrid calculations see equation (69)
$\zeta$	energy density of fuel
$\lambda$	fineness ratio
$\mu$	air dynamic viscosity
$\nu$	Poisson's ratio
$\rho_{air}$	density of air
$\rho_{cb}$	cylindrical beam material density
$\rho_{He}$	density of helium
$\rho_s$	skin density
$\sigma_a$	axial stress
$\sigma_{cb_{cy}}$	cylindrical beam compressive yield stress
$\sigma_{crit}$	critical stress
$\sigma_{crb}$	rib buckling critical stress
$\sigma_{csb}$	skin buckling critical stress
$\sigma_{cy}$	material compressive yield strength
$\sigma_r$	radial stress
$\omega$	rotational velocity
$\Omega$	relative velocity of cylinder surface to free-stream velocity

$\Omega_{\text{crit}}$

relative velocity at which virtual elliptical body forms

# **DESIGN OF A LIGHTER THAN AIR VEHICLE THAT ACHIEVES POSITIVE BUOYANCY IN AIR USING A VACUUM**

## **I. Introduction**

### **1.1 Motivation**

Lighter Than Air (LTA) vehicles have historically used lifting gases to achieve positive buoyancy in air. Buoyancy is defined as the force exerted on an object by the fluid in which it is submerged. This force is due to the difference in pressure at the top of an object vs. the bottom of the object. There is a difference in pressure because of the weight of the column of fluid surrounding the object. Positive buoyancy is defined as the weight of an object being less than the weight of the fluid it displaces. Negative buoyancy is defined as the weight of an object being more than the weight of the fluid it displaces, in other words, it tends to sink. Neutrally buoyant means the object is the same weight as the fluid it displaces, so that the force of buoyancy is equal to the object's weight [1]. A vehicle could theoretically achieve positive buoyancy through the use of a vacuum in place of a lifting gas. The difficulty of designing a vacuum LTA structure has prevented it from being used in the past. The primary advantage of a vacuum LTA structure would be the elimination of the requirement to purchase or transport a lifting gas.

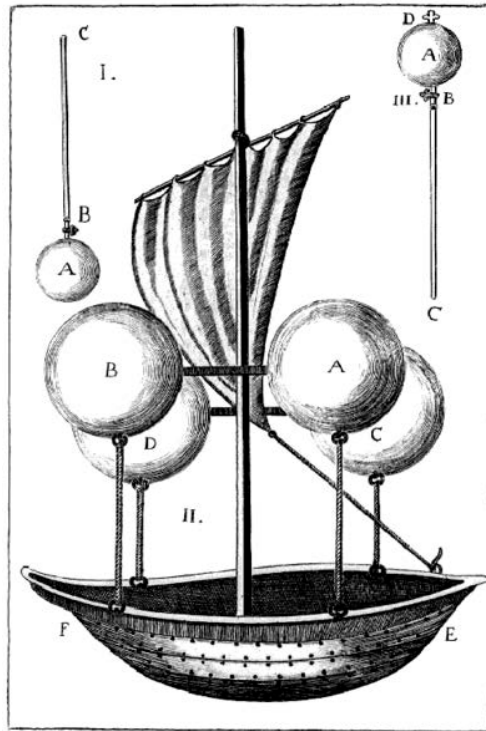
If a vacuum could be used to replace lifting gas, it would require a suitable mission to make it more than just an expensive parlor trick. There are various niche missions currently filled by LTA vehicles, but they are currently unable to compete with the mainstream modes of transportation. The vacuum LTA vehicle was evaluated to determine missions for which it was suited. One such mission motivated the first sponsor

of this research to investigate the following line of reasoning: Small, regional airports are largely underused while major airports are often congested. A vehicle capable of efficiently carrying cargo while operating out of small airports would fill a niche transportation market. This would require a vehicle that could land on short runways with large payloads. Could the vacuum LTA vehicle possibly be a solution to this challenge?

## **1.2 Background**

In 1670 Francesco Lana de Terzi published a book titled, “Prodromo dell'Arte Maestra” in which he proposed the design of a LTA vehicle that he theorized would attain positive buoyancy in air using a vacuum [2]. His structure resembled a ship and was suspended from four thin-shelled copper spheres as shown in Figure 1 [3] . Unfortunately copper does not have a high enough specific stiffness to achieve positive buoyancy in air using a smooth shell, as will be shown in the theory section of this thesis. Nevertheless, Lana correctly understood that the principal of buoyancy could be applied to air and that the sphere was the ideal shape for a LTA vacuum enclosure. The sphere is the ideal shape for a vacuum enclosure because it requires the minimum thickness to achieve the stiffness required to prevent buckling of any shape. It also has the minimum surface area per volume of any shape, which maximizes buoyancy, minimizes pressure loading, and minimizes weight.

**Figure 1: Lana's Flying Boat [3]**



During the course of this research it was not uncommon to find blogs and even published papers musing about the possibility of vacuum LTA structures. Most of the authors did not apply engineering principles to the problem. The most common misconception was that if a sphere was made big enough the problem would get easier because of the squared cube law. The idea behind the squared cube law is that the area of the sphere grows at a rate of radius squared, while the displaced volume of air grows at a rate of radius cubed. This is true, but the fallacy of this argument is in not understanding that the thickness of the sphere must grow as well. The tendency for a thin shelled sphere to buckle under external pressure is a function of the thickness of the shell as shown by equation (14) [4, p. 1292]. To prevent buckling, the thickness must grow proportionally

with the surface area of the sphere, so that no matter how big it is, the weight of the sphere remains proportional to the weight of the air displaced.

Akhmeteli and Gavrilin claimed that a vacuum LTA structure could be constructed using layered shell sandwich construction [5]. Their approach to the vacuum sphere formed the basis for equation (23) which not only shows why copper cannot be used to form a thin shelled, positively buoyant vacuum sphere, but why no material available today could either. Only a geometrically stiffened shell, such as the sandwich construction investigated by Akhmeteli and Gavrilin, could possibly achieve this feat.

### **1.3 Research Objective**

For a theoretical vehicle to be operationally viable, it must achieve performance comparable to or better than existing vehicles with similar mission types. The C-27J was designed to transport cargo to small airports relatively efficiently. One purpose of this thesis was to determine whether a vacuum LTA vehicle could effectively perform the same mission as the C-27J. Therefore it became necessary to evaluate the C-27J capabilities and compare it to any proposed vacuum LTA vehicle design. The C-27J specifications are listed in Table 1, [6].

**Table 1: C-27J Specifications [7]**



**Dimensions**

Span	28.70 m	94.16ft
Length	22.70 m	74.48 ft
Height	9.65 m	31.6 ft
Wing area	81.94 m	882 ft

**Weights**

Normal Landing Weight	27,500 kg	60,627 lb
Maximum Takeoff	31,800 kg	70,107 lb

**Power Plant**

Engine	Rolls-Royce AE 2100-D2
Engine Power	4637 Shaft Horse Power
Propeller	Dowty R-391 six-blade

**Performance (clean, ISA)**

Maximum Service Ceiling	9,144 m	30,000ft
Maximum Cruise Speed	315 KTAS	
Landing Ground Roll	340 m	1,115 ft
(Maximum Landing Weight, Sea Level)		

LTA vehicles are generally stable, limited in speed, have long loiter times, large payloads, and poor handling qualities in the landing environment. These characteristics have largely relegated them to niche markets such as surveillance, communication relays, and advertisement. Table 2 lists key questions that must be answered in order to determine whether a vacuum LTA vehicle is a feasible concept.

**Table 2: Research Questions**

1	Can positive buoyancy be achieved by a structure in air using a vacuum?
2	Is a vacuum LTA structure a feasible platform for any existing missions?
3	What is the ideal internal pressure of a partial vacuum LTA structure?
4	What is the ideal operating altitude of a vacuum LTA structure?
5	Are there viable geometric shapes for a vacuum LTA structure?
6	Do construction techniques exist which can construct the required geometric shapes?
7	What are the critical material properties for a vacuum LTA structure?
8	Do materials exist from which a vacuum LTA structure can be constructed?

#### **1.4 Thesis Overview**

Is LTA flight possible using a vacuum? During the course of this investigation von Karman's efficiency was used to compare theoretical vehicle design spaces to existing vehicles. A unique vehicle consisting of counter-rotating cylinders that take advantage of a virtual elliptical body to minimize drag was proposed and evaluated for its energetic feasibility. A program was developed in Matlab that optimized the geometry of a geodesic sphere through the use of built in optimization functions and finite element analysis. All of these investigations attempted to answer the research questions posed in Table 2.

The literature review section examines historical LTA vehicles to determine the criterion for a successful LTA vehicle. It further defines the problem of constructing a vacuum sphere through the study of thin shelled spheres under pressure. Finally, it introduces the two methods of geometrically improving upon a thin shelled sphere that were used in this study. These are stiffening of a thin shell using blade type stiffeners arranged in an isogrid and a geodesic sphere of cylindrical beams supporting a thin membrane.

The methodology section introduces the counter-rotating cylinder LTA vehicle and explains the methods used to evaluate its feasibility. It explains the methods used to evaluate an isogrid design. Finally, it describes how the geometry of a geodesic sphere was calculated, evaluated, and optimized.

The results section gives an answer to the viability of each of the proposed methods for achieving positive buoyancy using a vacuum. The vehicle design spaces are plotted on a von Karman efficiency graph. The design spaces of the isogrid stiffened sphere and geodesic spheres are graphed for a visual representation of the optimization performed on each structure. The thesis concludes by answering the questions posed in the objective section along with recommendations for further study. The appendix contains samples of the Matlab code used to perform each part of this study.

## **II. Literature Review**

### **2.1 Chapter Overview**

There is a scarcity of literature available on vacuum LTA vehicles, which is not surprising considering none have yet been built. However, each of the components required for a successful vacuum LTA vehicle have been extensively studied and published. The focus of this section is to introduce LTA vehicles, their structures, missions, and potential areas for improvement.

Although a vacuum LTA structure has apparently never been built, there has been extensive research into the buckling of pressure vessels under external pressure. This section examines the empirically derived formulas for failure of a sphere and applies

them to the problem of achieving positive buoyancy in air. After establishing that a thin shelled sphere constructed of contemporary materials cannot achieve positive buoyancy in air using a vacuum, this section presents two possible methods of geometrically stiffening a sphere to prevent buckling without adding too much weight. These methods are an isogrid stiffened sphere and a geodesic sphere.

## **2.2 Historical LTA Vehicles**

LTA vehicles have a long history of impressive achievements and yet have been relegated to filling niche mission profiles. These achievements include the first human flight, accomplished in a hot air balloon by Jacques-Étienne Montgolfier in 1782 [8, p. 2] and the first passenger airline *Deutsche Luftschiffahrts-Aktiengesellschaft* (DELAG) in 1909 [9]. In 1917 the L-59 “Africa Ship” proved the feasibility of intercontinental zeppelin travel by carrying 15 tons of cargo and 22 persons on a 4,225 mile flight during a supply mission to German East Africa [9]. The qualities of LTA vehicles enabled them to accomplish missions unsuitable for other vehicles, but also historically prevented them from competing against mainstream methods of transportation. Of primary importance to this study is airship structure, mission profiles, and potential for improvement on historical designs.

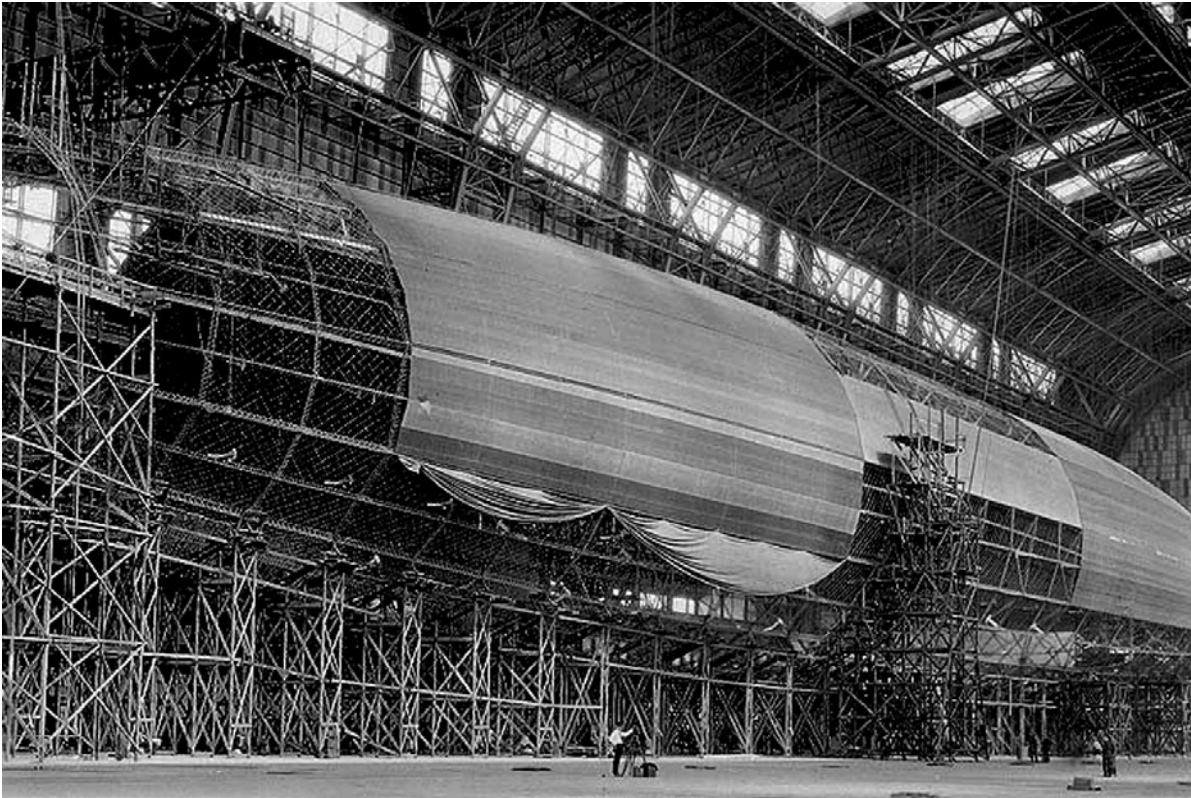
### ***2.2.1 Airship Structures***

Airship structures can be organized into three primary categories; rigid, semi-rigid, and non-rigid. Each of these structures have qualities that significantly impact operational capabilities.

### 2.2.1.1 Rigid

Rigid structures consist of a rigid frame with a skin stretched over the outside as shown in Figure 2 [10]. The frame distributes loads throughout the ship. The original Zeppelins consisted of an aluminum frame surrounded by a permeable cloth skin. Hydrogen lifting gas was contained within animal skin ballonets inside the structure. Weight/Buoyancy (W/B) for these structures was poor, requiring large volume to achieve useful designs. Modern material and construction technologies can significantly decrease the weight of rigid frames and skins through the use of carbon composites and advanced fabrics and membranes. A modern example of a rigid airship is the experimental Aeroscraft created by the Aeros company [11]. Rigid structures are able to maintain their shape because of the rigid nature of their structures. This enables the design of lifting bodies as well as the ability to withstand large aerodynamic loads without significant warping. Rigid structures also transmit loads throughout the structure which enables mounting of engines, gondolas, and control surfaces. This enables improved controllability by side mounted, vectored thrust engines, reduced drag by internally placing payloads, and optional hybrid lift by taking advantage of a lifting body shape. Hybrid lift is the use of aerodynamic lift in addition to buoyant lift. Although aerodynamic lift incurs significant drag in the case of a LTA vehicle, it allows take off and landing in a heavier than air configuration which improves ground handling.

**Figure 2: USS Shenandoah Rigid Construction [9]**



Disadvantages to the rigid airship design include increased weight for the frame [8, p. 22] and poor damage tolerance due to the rigidity of the structure [9, p. 150]. Whereas a non-rigid structure can bend without damaging the structure when design bending moments are exceeded, a rigid structure will be damaged when bending moments are exceeded.

An interesting variation of the rigid airship design is the metal-clad airship as shown in Figure 3 [12]. The US Navy Metal Clad Airship (ZMC)-2 consisted of an aluminum skin with aluminum stringers riveted together. The ZMC-2 was notable for its ability to retain the helium lifting gas much longer than contemporary LTA vehicles [12]. This was due to the low permeability of the aluminum skin. It was also notable for its low

fineness ratio ( $\lambda$ ), which is defined by equation (11) and is the ratio of length to diameter, which was chosen to add strength to the structure [8, p. 57]. The low  $\lambda$  strengthened the ZMC-2 by decreasing bending moments and increasing the resistance to bending [13, p. 163], [12]. There are published equations for calculating moments on an airship in [13, p. 163], but a simplified explanation as to why low  $\lambda$  decreases moments and increases resistance to moments can be made by picturing the LTA vehicle as a cylinder. The longer the cylinder, and thus the higher  $\lambda$ , the higher the bending moments the LTA vehicle will experience simply due to a longer moment arm. For a given volume, a higher  $\lambda$  corresponds to a lower radius, which in terms of a cylinder would mean less resistance to bending. Also, as length increases and volume remains the same, cross sectional area also increases, thus increasing loading due to gusts. A low  $\lambda$  decreases stability because of the lower rotational inertia and moment arm when compared to a higher  $\lambda$ , requiring relatively large stabilizers on the ZMC-2.

**Figure 3: ZMC-2 Metal Clad Airship ca. 1930 [12]**



#### 2.2.1.2 Semi-Rigid

Semi-rigid airships consist of a rigid internal frame surrounded by an inflated skin that maintains shape through the use of internal pressure. These structures carry the advantages of both the rigid and non-rigid designs. The rigid internal frame distributes loads throughout the ship and enables freedom to mount engines, payloads, and control surfaces anywhere on the airship. The pressure supported skin enables a smaller internal frame that is strength, not shape, oriented, thus reducing weight.

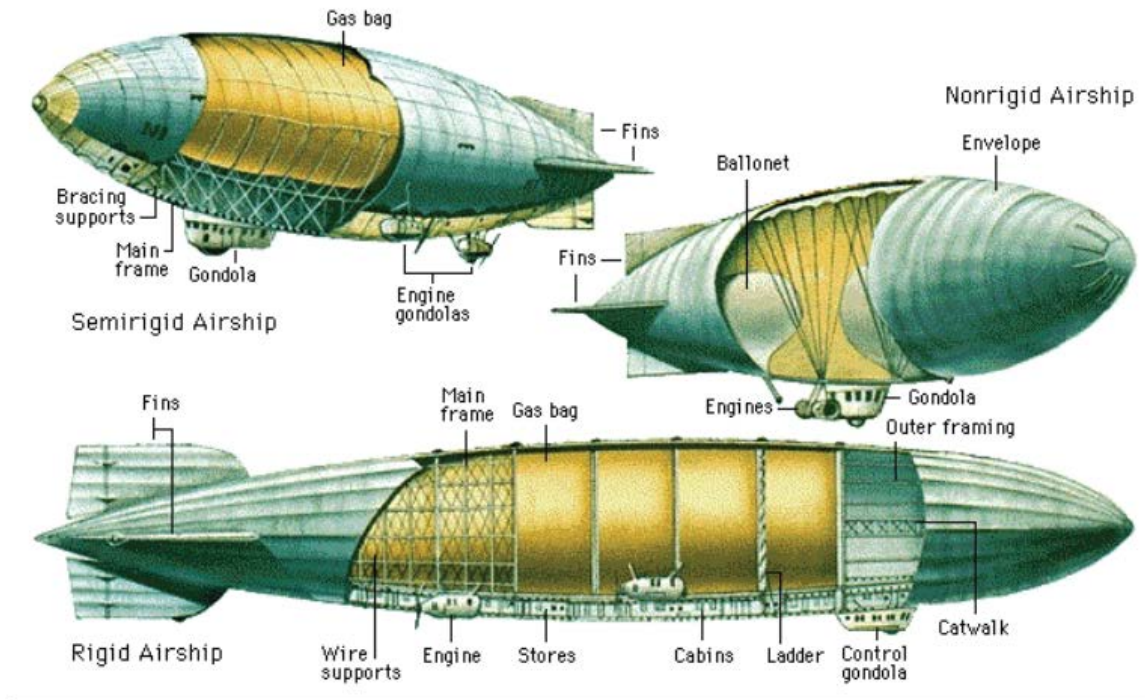
A modern example of the semi-rigid airship is the Zeppelin-NT, which has an internal frame as shown in Figure 4 [14]. The Zeppelin-NT rigid frame is composed of triangular trusses that run the length of the airship. The skin touches the frame at specific points but maintains its shape through internal pressure. This airship can conduct ground handling with a crew of three people using vectored thrust [15]. Vectored thrust is made

possible by the side mounting of its engines, which is made possible by the internal frame.

### 2.2.1.3 Non-Rigid

Non-rigid airships consist of an inflated gas envelope that maintains shape through internal pressure. These structures are popularly referred to as “blimps”. In order to withstand mooring and aerodynamic forces, the bows of non-rigid airships generally have rigid caps. There is also usually a rigid structure at the stern for mounting the stabilizers. The gondola generally hangs externally from a canopy that distributes forces over a large portion of the gas envelope as shown in Figure 4 [14]. A modern example of a non-rigid airship is the 1960s era Goodyear Blimp as shown in Figure 4. Non-rigid airships do not require significant structures and therefore can achieve low W/B and high altitude such as the Lockheed Martin High Altitude Long Endurance Demonstrator. They also have the added advantage of being resilient. If the design bending moment of a non-rigid airship is exceeded, the skin may temporarily kink, but unlike the rigid airship, it will not be damaged[13, p. 164]. This is because internal gas pressure provides structural support as opposed to a rigid structure.

**Figure 4: Semirigid, Nonrigid, Rigid Airships [14]**



### **2.2.2 Missions**

The original mission of the LTA vehicle was aerial reconnaissance. In 1806 Frenchman Jean Coutelle was lifted 450 meters in a tethered balloon to observe enemy formations and movements in the French Revolution [8, p. 2]. Airships were used in the American Civil War, the Franco-Prussian Wars, World War I and World War II [8, p. 2]. During that time Airships conducted passenger and cargo transportation, reconnaissance, and bombing. As heavier than air flight technology matured, LTA vehicles were replaced by heavier than air vehicles for many of these missions. Today LTA vehicles, to include unmanned airships and aerostats, are primarily used as sensor platforms and communications relays [16]. Airships in particular are used for product recognition, advertising, tourism, and as commercial aerial photography platforms [17]. The

endurance, lift capacity, and stability of LTA vehicles makes them well suited for these missions, but there are aspects of LTA vehicles that prevent them from being used for cargo or passenger transportation. These aspects are design challenges that must be overcome if the LTA vehicle is to become a viable competitor in the transportation establishment.

### ***2.2.3 Design Challenges***

The first design challenge of LTA vehicles is ground handling, which historically requires robust hangars and mooring capabilities. A related design challenge is buoyancy control which significantly affects mooring and taxiing. Lifting gases pose unique supply and operational problems that must be addressed. Efficiency, as it relates to velocity and fuel requirements, is the final design challenge.

An important aspect of LTA history is written in the mishap record. The mishap record has recurring themes that shed light on the design challenges of LTA vehicles. It is the duty of the operator to recognize these themes in order to avoid repeating the mistakes of the past, and the duty of the engineer to prevent future loss of life and property through the improvement of design. Because this is a design oriented study, it proved fruitful to study the mishap record. The mishap study gave clear answers to several of the questions posed in the objective section about how to make the LTA vehicle competitive as a cargo or passenger transportation platform.

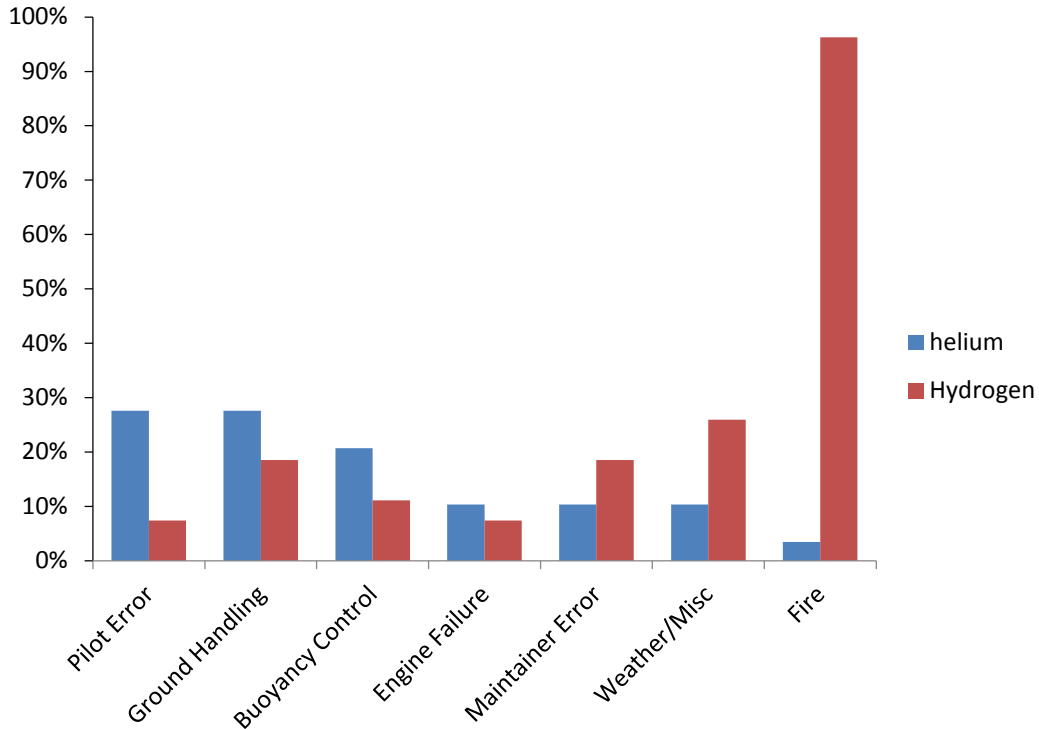
A review of mishap records for LTA vehicles over the previous century revealed an interesting trend as shown in Figure 5 [9], [18]. Mishap causal factors for LTA vehicles are shown by percent of total reported mishaps for both hydrogen and helium airships over the past century. It is interesting to note that pilot error accounted for far

less mishaps in hydrogen airships than in helium airships. The reason for this trend is possibly twofold. Pilots of hydrogen airships flew at a time when airships were far more prevalent, and training was much more robust in the form of master and apprentice [9]. Pilots of helium airships were flying during a time where airships were one of a kind, experimental aircraft with inexperienced crew, resulting in a higher probability of pilot error (with the exception of the Goodyear Blimps, which have an impressive safety record and experience pilots). The most staggering statistic is that 96% of reported hydrogen airship mishaps involved fire. It is likely that there were many unreported mishaps and that those mishaps not resulting in fire were often not important enough to be included in the historical reports used for this study. The helium airship mishap statistics come from modern aircraft mishap reporting requirements, which include a high number of minor incidents. This skews the statistics towards making reported hydrogen airship mishaps seem more catastrophic on average than reported helium airship mishaps. That being said, the number of hydrogen airship mishaps resulting in death is a staggering 41%. Even more devastating, 15% of Hydrogen mishaps resulted in 100% loss of life onboard. Even when a helium airship mishap resulted in death, it was usually only one or two people with the vast majority of those involved surviving with little or no injury. In addition to the loss of life, every hydrogen airship mishap involving fire resulted in a complete destruction of the airship, which represents significant monetary loss, often including buildings on the ground.

Another skew to the statistics is that many of the mishaps involving maintenance did not involve people on board the airships, so that the number of hydrogen airship mishaps not resulting in death or injury was increased. The potential for destruction by

hydrogen explosions and fire was so great that in one incident four airships were destroyed in a single hangar fire. Goodyear Blimps stopped using hydrogen as a lifting gas after the Wingfoot Air Express crashed into the Chicago Trust and Savings Building killing 13 people and injuring 27 in 1919 [9]. The US government stopped using hydrogen as a lifting gas after the US Army airship Roma hit power lines, ignited and killed 34 out of 45 people on board in 1922 [9]. The infamous Hindenburg was actually designed to carry helium, but due to the US policy of hoarding helium in anticipation of World War II, the US refused to sell helium to Nazi Germany [9]. This decision resulted in the most widely publicized airship disaster. Interestingly, the USS Akron, the airship with the most deadly airship crash in history, was a helium airship. In the Akron disaster, it was hypothermia and drowning in the ocean due to a lack of life boats that resulted in the deaths of 73 out of 76 crewmembers [9].

**Figure 5: Causes of 29 Helium and 27 Hydrogen Airship Mishaps**



The study of mishaps enables the airship designer to avoid past mistakes and mitigate risk. The primary cause of death and destruction in airship history is unequivocally fire as a result of using hydrogen as a lifting gas. The simple solution to this problem is to use an inert lifting gas such as helium. Unfortunately, if helium is unavailable as in the case of the Hindenburg, there are few lifting gas alternatives. This is a strong argument for the investigation of a vacuum in place of a lifting gas.

Weather, pilot error, and maintainer error are all mishap causes that can be mitigated through modern aviation practices. This leaves ground handling and buoyancy control as the primary safety concerns for the designer of LTA vehicles. These two issues are actually closely related and can both be mitigated by buoyancy control.

#### 2.2.4.1 Ground Handling and Buoyancy Control

The problem with ground handling of LTA vehicles is that they are large and therefore experience great forces due to wind gusts that can push them into obstacles, damage their structure and break mooring lines. In addition to large wind loads, LTA vehicles are generally close to neutral buoyancy, which results in very little force anchoring them to the ground, requiring significant mooring measures. Ground handling of the large airships built during the early 20th century required crews as large as 700 men [19, p. 300] to hold the mooring lines as shown in Figure 6, [9]. These operations were so labor intensive that airships had to land or take off in the early morning or late evening when the mooring crews were off work [9]. The problem was that the ground crews were not full time airship handlers, they had full time jobs and were part time airship handlers. Many airships were damaged during mooring operations, especially when being moved in and out of hangars. As shown in Figure 5 about a quarter of mishaps occurred during ground handling. To reduce the chance of mishaps, anchor airships for servicing between flights, and decrease manpower requirements, fixed and portable mooring masts were constructed. Portable mooring towers were originally trains on tracks that could safely move the airships in and out of their hangars. Today's smaller LTA vehicles are moored by trucks with towers attached. The Zeppelin NT, through the use of vectored thrust and portable mooring towers, can moor with a crew as small as three people [15].

**Figure 6: Ground Handling [9]**



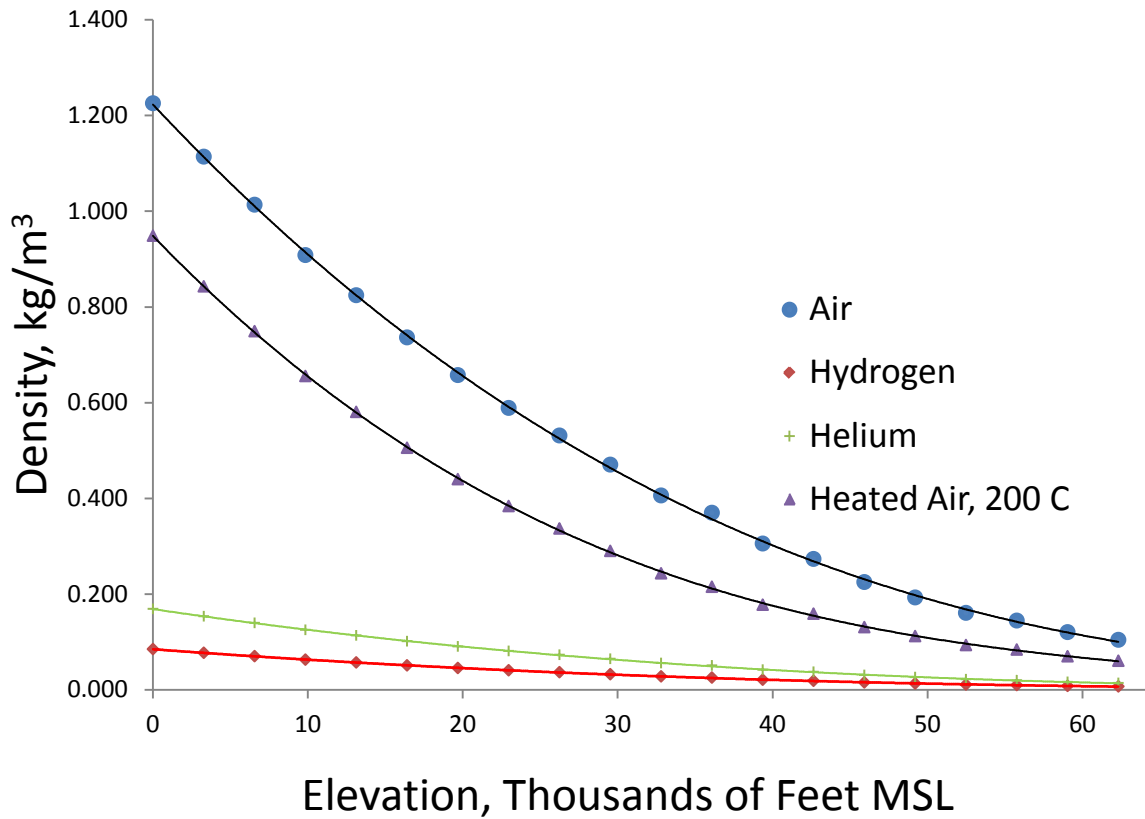
In order for LTA vehicles to become more practical they would require the ability to land at small, unimproved airfields without mooring facilities. This could be accomplished with the ability to land and taxi heavier than air. This would be possible with advanced buoyancy control through the use of onboard compressors coupled with hybrid lift for landing heavier than air. If the buoyancy of a LTA vehicle could be precisely and rapidly adjusted, it would enable vertical take offs and landings without significant ground crew involvement or mooring equipment. This would enable use of LTA vehicles at unimproved landing sites, greatly increasing their usefulness. This point was not lost on Pasternak, owner of the Aeros company, who is currently focusing on

designing the next generation of LTA vehicles. Aeros' primary technological improvement over traditional designs is buoyancy control [20].

#### 2.2.4.2 Lifting Gas

All methods of achieving LTA flight to date have relied upon lifting gas. Common lifting gases are heated air, helium, and hydrogen. Lifting gases serve to displace the ambient air and thus achieve positive buoyancy. LTA flight is possible due to buoyancy, which is defined by the Archimedes principal which states, "the buoyant force on a submerged object is equal to the weight of the fluid displaced by the object." [8, p. 14]. If a structure will float in air the weight of the air displaced must be greater than the weight of the structure that displaces the air. The weight of the structure will include any gas contained inside the structure, so that a structure will be more likely to float if it contains a gas with a density lower than the air it displaces. The densities of the most common lifting gases are plotted in Figure 7. Hydrogen has the lowest density of any lifting gas. Helium is a close second, while heated air is only slightly less dense than air at standard atmospheric temperatures. In the case of an absolute vacuum there is no lifting gas so only the weight of the structure is considered to determine whether there is positive buoyancy.

**Figure 7: Comparison Between Lifting Gases**



The first human flight was conducted in a LTA vehicle using heated air as a lifting gas [8, p. 2]. Today heated air is only used as a lifting gas for recreational purposes due to its relatively low buoyancy and high energy requirements. The high energy requirement stems from the need to keep adding energy to the lifting gas to keep the temperature elevated.

Hydrogen has the lowest density of any lifting gas and was used as early as the civil war due to its high availability [8, p. 16]. Unfortunately hydrogen tends to produce violent chemical reactions with oxygen in the presence of a flame or spark, which generally results in catastrophic mishaps in LTA vehicles as shown in Figure 5, [9]. For

this reason hydrogen is seldom used as a lifting gas today. In order for hydrogen to be a viable lifting gas, the hydrogen airship would have to be designed in such a way that even in a mishap the hydrogen would not be ignited. It is possible that an airship could be designed with crash resistant, internal ballonets of hydrogen that could reduce the chances of catastrophic failure to an acceptable level. Modern buoyancy control would negate the need to valve off hydrogen during flight which would prevent dangerous mixtures of hydrogen and oxygen. Non-flammable membranes could also be used to prevent fire from spreading from an engine to the lifting gas. A cost benefit analysis would need to be performed to determine whether these additional design constraints would make hydrogen a reasonable substitute for helium. Regardless of how many safety measures are in place, hydrogen always has the potential to burn, which may prohibit it from ever being a viable lifting gas where human life is at risk.

Helium has become the lifting gas of choice for LTA vehicles because it is chemically inert and has the second lowest density of any gas [8, p. 16]. Problems with helium as a lifting gas are primarily the small size of the helium molecule, which tends to pass through the thin membranes used to enclose it [21, p. 3], as well as mining and shipping costs. These problems do not generally pose a functional obstacle to the use of helium as a lifting gas, but do pose economic and supply challenges. Furthermore, the cost of helium is forecast to rise significantly in the next few years due to increased global demand and reduced supply [22]. Right now helium is widely available and costs about five times that of hydrogen [23]. Helium is a nonrenewable resource that is the product of radioactive decay, and unlike hydrogen, can not be manufactured. At current consumption rates it appears helium will continue to be available for at least a couple

more decades, however costs are forecast to rise significantly in the immediate future when the Bureau of Land Management stops selling helium to the public [23], [22].

#### 2.2.4.3 Efficiency

The efficiency of any vehicle has a strong influence on whether or not it is economically feasible. Even if the handling characteristics of LTA vehicles are improved, the velocity, payload and efficiency of LTA vehicles will have to be comparable to vehicles with similar missions. For example, if the LTA vehicle travels the same velocity as a truck, lands at the same distribution centers as a truck, moves the same payload as a truck, but uses twice as much fuel, it will not be considered a viable alternative. Drag reduction, weight reduction, and increased propulsion efficiency all have the potential to improve LTA vehicle efficiency.

Drag reduction can be accomplished through selection of optimal fineness ratio, Boundary Layer Control (BLC), and a clean profile. Fineness ratio ( $\lambda$ ) is defined in equation (11) as airship Length/Maximum Diameter [8, p. 44]. The longer a ship, the less pressure drag it experiences for a given volume, but the more skin friction drag it incurs. Therefore, there is an optimal  $\lambda$  where the sum of skin friction drag and pressure drag is a minimum. A  $\lambda = 4.62$  was found to result in the lowest total drag for C- Class airships during wind tunnel testing [8, p. 57], but the ideal  $\lambda$  will change with various design factors such as aircraft shape, BLC devices, and propulsion location.

BLC can be used to reduce pressure drag and thereby enable a lower  $\lambda$  which will in turn decrease skin friction drag. A Griffith airfoil which was designed to achieve laminar flow through BLC is shown in Figure 8 [24]. Laminar flow is negligible in

Reynolds Numbers ( $Re$ )  $> 10^7$  even with BLC, but BLC in the case of an airship can prevent flow separation and thereby decrease pressure drag.  $Re$  is a non-dimensional number calculated according to equation (1), where  $Re$  is the ratio of inertial forces to viscous forces [25, p. 350]. An airship the volume of the Zeppelin NT at  $8,297 m^3$  with a  $\lambda = 2.5$  would be 47 meters long. If it was travelling at a  $u_\infty=36$  m/s, in a standard sea level atmosphere, the  $Re$  would be about  $1.15 \cdot 10^8$ , meaning a Griffith airfoil would not achieve laminar flow. Goldschmied [24] conducted wind tunnel testing on bodies of revolution based on the Griffith airfoil where he showed that this concept for a submerged body resulted in a  $C_D=0.0162$ . In comparison, the Akron Airship model had a  $C_D=0.0235$  at the same Reynolds number. In addition to drag reductions, he also showed there would be a decrease in propulsive power required by 45% when using a stern mounted propeller. His design consisted of a combination of a body of revolution designed after a Griffith airfoil with a  $\lambda \cong 2.5$ , which maintained a positive velocity gradient along the body of the airfoil until approximately 80% chord, followed by an abrupt velocity discontinuity. A slot was placed just aft of the point of discontinuity which prevented the flow from separating using suction pumps. These pumps then discharged the fluid at near zero velocity into a stern mounted propeller, thus increasing the propeller's efficiency above that of conventional stern mounted propellers.

$$Re = \frac{\rho_{air} \cdot u_\infty \cdot l}{\mu} \quad (1)$$

Where:

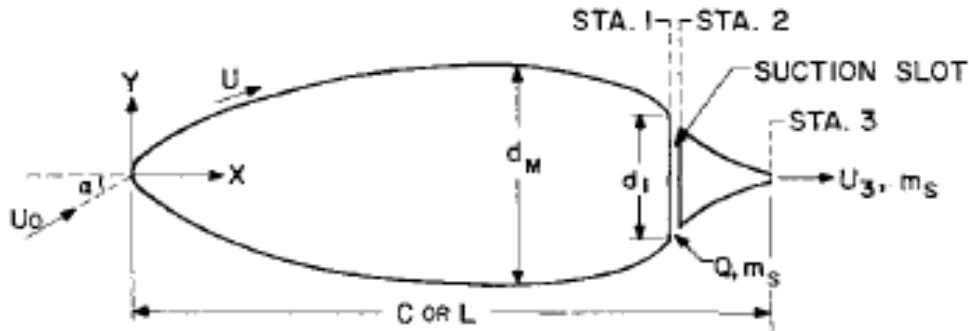
$l$  = airship length

$u_{\infty}$  = freestream velocity

$\mu$  = dynamic viscosity

$\rho_{air}$  = air density

Figure 8: Griffith Airfoil [24]



A clean profile can result in drag coefficient reductions by as much as half. The drag coefficients by Goldschmied [24] were for a clean body of revolution and did not include a gondola, control surfaces, mooring lines, cables, landing gear, antennas etc... Through the use of modern materials most of those objects could be placed inside the envelope of the airship, significantly decreasing drag. Control surfaces, however, will most likely be required unless control can be achieved through a creative use of the suction slots and/or vectored thrust.

Weight reduction is important in any aircraft design. In the case of the airship it is useful to minimize the ratio of Weight/Buoyant Force ( $W/B$ ). A  $W/B=1$  would be a neutrally buoyant structure that neither rises nor falls. A  $W/B<1$  would be positively buoyant and float. A  $W/B>1$  would be negatively buoyant and sink. The lower the  $W/B$

of an airship, the more payload it can carry for a given volume, which translates in to greater transportation efficiency. Modern materials enable the construction of vehicles with much lower W/B than in the past. Modern airships often achieve  $W/B < 0.3$  [13, p. 418], The Zeppelin NT has an estimated skin plus frame  $W/B \cong 0.18$  [15].

Improved propulsion efficiency can be accomplished through propeller placement and improved engine efficiency. Stern mounted propellers have been shown to reduce power required by about 26% by placing the propeller in the wake of the airship [24]. There is an additional drag savings by eliminating the need for fins on the side of the airship for mounting propellers. A stern mounted ducted fan or propeller in conjunction with a BLC suction slot on a Griffith airfoil was predicted to reduce power required by as much as 50% [24]. The tradeoff with stern mounted propulsion is a loss in maneuverability. If the airship gains 50% efficiency, but loses the ability to land at unimproved airfields it may not be a viable design. Therefore maneuverability would need to be considered in engine placement. A possible solution is to use propulsion similar to naval ships, which often have both bow and stern vectored thrust [13, p. 369]. By also placing an engine near the bow of the airship, controllability would be greater than with side mounted propulsion due to increased moment arms.

Engine efficiency can possibly be improved on airships through the use of high efficiency engines such as diesel instead of high specific power engines such as turboprops. An optimization would have to be performed which took into account the specific mission for which the airship was being designed to make a correct judgment on engine type. A high specific power engine would be ideal for short mission durations, but

a high efficiency engine might be preferable for long missions due to a decreased fuel weight.

Efficiency comparisons between vehicles of different types can be difficult. A vehicle designed for carrying a large amount of cargo can be expected to require more power than a vehicle designed for carrying a few passengers. Also, a vehicle designed for high velocities can be expected to require more energy than one designed for low velocity. Gabrielli and von Karman defined von Karman efficiency ( $e_{VK}$ ) according to equation (2) [26]. Von Karman efficiency enables side by side comparisons of different vehicles by calculating efficiency based on the power required to move the maximum payload at the maximum velocity attainable by that vehicle. Note that  $e_{VK}$  is a non-dimensional quantity that essentially gives a ratio of power required to useful power output. In the business of transporting cargo useful work would be defined as moving cargo, and useful power can be defined as moving cargo at a given velocity. Increasing velocity is desirable for some missions, but there is an associated cost of lost efficiency. This relationship between efficiency and velocity is shown in Figure 9. The cost of increasing velocity was shown by the Gabrielli-von Karman limit defined by equation (3). A plot of the Gabrielli-von Karman limit, as well as  $e_{VK}$  for various vehicles is shown in Figure 9.

$$e_{VK} = \frac{P_{req}}{W \cdot u_m} \quad (2)$$

$$e_{VK_{LIMIT}} = 0.000175 \cdot u \quad (3)$$

Where:

$e_{VK}$  = Von Karman Efficiency

$P_{req}$  = Power Required

$u$  = velocity mph

$u_m$  = Maximum Velocity

$W$  = Useful Lift

Figure 9: Von Karman Efficiency of BLC Vehicles

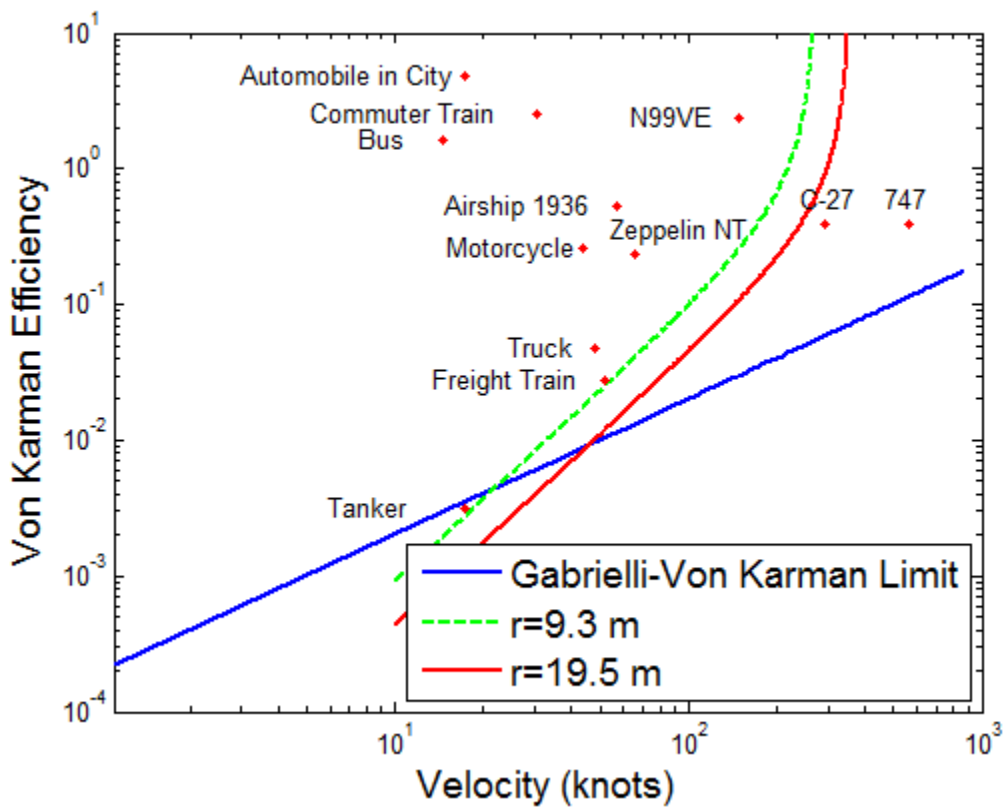


Figure 9 uses data for various vehicles operating with their typical payload and velocity [26]. Larger values of  $e_{VK}$  mean less efficient modes of transportation so that to

move up on the y axis is to be less efficient, and to move right on the x axis is to achieve higher velocity. The dotted line on Figure 9 represents the Gabrielli-von Karman Limit, (3). This limit can be used to compare the relative efficiency of different vehicles. A vehicle that falls near the Gabrielli-von Karman limit can be considered a high efficiency vehicle in comparison to other vehicles that operate at the same velocity. The Gabrielli-von Karman limit is based on viscous drag and vehicle data available in 1950. This limit can be broken by highly efficient modes of transportation such as trains and tankers, and so should be thought of as a guideline more than as a limit.

The dashed curve in Figure 9 is of an idealized airship with an internal volume of  $8,297 m^3$ , the same as the Zeppelin NT [15]. The solid line is the same idealized airship design with an internal volume of  $77,956 m^3$ . The larger version can carry a payload of 13,617 kg at 120 Knots Indicated Air Speed (KIAS) at 10k ft for 1852 km which is the range for the C-27J carrying 10,000 kg of cargo. The smaller airship represented by the dashed curve can only carry 1,361 kg to 10k ft at 100 KIAS for 1852 km. This is a simplified scenario which does not take into account the requirement for the structure to compensate for larger engines and higher aerodynamic loads. It includes increased engine and fuel weight according to equations (6) and (7). It also assumes a completely clean aerodynamic profile where the landing gear and control car are shrouded inside the airship to reduce drag. The curve does not represent the performance of one vehicle at various velocities as was done in [26], but instead the performance of one vehicle at its maximum velocity for hundreds of different sized engines. This approach was taken to explore the potential design space of a theoretical LTA vehicle in order to determine a suitable maximum velocity. At the top right of the solid and dashed curves the airship has

an engine so big it can not carry any payload in addition to the required fuel and engine, at the bottom left an engine so small it can only propel the vehicle at 10 kts. The solid and dashed curves are meant to represent the limit of what can be expected from an airship with suction type BLC that is completely optimized for a given volume for weight, drag, and propulsion efficiency. This shows that the larger the airship, the more efficient it becomes. It also shows how the ideal airship compares to other modes of transportation. Notice that the von Karman efficiency of the Zeppelin NT is shown in Figure 9. The potential improvement between the Zeppelin NT and the idealized BLC airship with a volume equal to the Zeppelin NT is enormous. The actual Zeppelin NT has an external gondola, fin mounted propellers, and no BLC. It cannot be reasonably expected that an actual vehicle will perform as well as the solid and dashed curves. Instead these curves are meant to represent the limit of conventional airship technology. The usefulness of the curves is that they show the advantage of designing airships for low velocities, the cost of higher velocities, and the upper limit of design velocities. This limit shows that above certain design velocities an increase in engine power only serves to decrease efficiency.

Von Karman efficiency was calculated for the idealized airships in Figure 9 using Equations (4) - (11). The assumptions used for these calculations are listed in Table 3. The payload weight is used in equation (2) and calculated using equation (4). The payload weight is the buoyant force of the airship minus the weight of the structure, engine, and fuel. Equations (6) [13, pp. 225-226] and (7) [25, p. 233] give the engine and fuel mass which are based on the power requirements of equation (8) [25, p. 238]. Engine mass in equation (6) is based on average specific power of conventional aircraft turbine engines after they have been installed on the aircraft. Power is a function of volume and

velocity. The plots of von Karman efficiency vs. velocity were made possible by solving for power required and maximum payload weight as functions of velocity for a given mission range. It was important to select a mission range because this determined how much fuel needed to be carried, which affected the payload capacity. Ranges in this case were based on the C-27J in order to make a comparison between C-27J capabilities and conceptual aircraft designs. The drag of an airship as shown in equation (9) is based on the volumetric drag coefficient. It is a function of airship volume instead of frontal area [27, p. 4] making the assumption that airships have the classical prolate spheroid shape. The volume of an airship, which makes the same basic shape assumptions as equation (9), is shown in equation (10) and is a function of fineness ratio  $\lambda$ .

$$W = L_b - g \cdot (m_s + m_e + m_f) \quad (4)$$

$$L_b = V \cdot (\rho_{air} - \rho_{tg}) \cdot g \quad (5)$$

$$m_e = P_{tot} \cdot 0.00201 \frac{\text{kg}}{\text{watt}} \quad (6)$$

$$m_f = \text{range} \cdot \frac{P_x}{k_{ee} \cdot u_x \cdot \zeta} \quad (7)$$

$$P_x = k_{pe} \cdot \frac{D^2}{2 \cdot \rho_{air} \cdot a_p \cdot u_\infty} \quad (8)$$

$$D = \frac{1}{2} \cdot \rho_{air} \cdot u_{\infty}^2 \cdot V^{\frac{2}{3}} \cdot C_D \quad (9)$$

$$V = \frac{4}{3} \cdot \pi \cdot r^3 \cdot \lambda \quad (10)$$

$$\lambda = \frac{l}{2 \cdot r} \quad (11)$$

Where:

$a_p$  = propeller area

$C_D$  = Volumetric Drag Coefficient

$D$  = drag force

$k_{ee}$  = 1/engine efficiency

$k_{pe}$  = 1/propeller efficiency

$l$  = length

$L_b$  = buoyant force

$m_e$  = engine mass

$m_f$  = fuel mass

$P_x$  = power required to maintain translational velocity

$r$  = radius

$V$  = volume of airship

$W$  = useful load assuming W/B=0.3

$\zeta$  = energy density of fuel

$\lambda$  = fineness ratio

$\rho_{air}$  = density of air

$\rho_{lg}$  = density of lifting gas

**Table 3: BLC LTA Vehicle Assumptions**

$a_p$  = 12.5 m<sup>2</sup> Zeppelin NT sized airship [15]

$a_p$  = 56 m<sup>2</sup> size required to carry 10,000kg, to 10k ft, 1852 km

$C_D$  = 0.0169 based on hull plus tail fins [24]

$k_{ee}$  = 0.33 33% efficient turboshaft engines [13, p. 105]

$$k_{pe} = \frac{1}{0.85} \text{ assuming stern mounted suction slot and ducted fan [24]}$$

$$r = 9.3, \text{ m Zeppelin NT sized airship [15]}$$

$$r = 19.5, \text{ m size required to carry 10,000kg, to 10k ft, 1852 km}$$

$$v = 8,297 \text{ m}^3 \text{ volume of Zeppelin NT [15]}$$

$$v = 77,956 \text{ m}^3 \text{ size required to carry 10,000kg, to 10k ft, 1852 km}$$

$$m_s = 30\% \text{ of } \frac{L_b}{g} \text{ assuming } W/B = 0.3 \text{ [15]}$$

$$\lambda = 2.5 \text{ based on Griffith Airfoil [24]}$$

$$\rho_{air} = 0.889 \text{ kg/m}^3 \text{ at 10k ft MSL standard atmosphere [28]}$$

### 2.3 Thin Shelled Sphere

LTA structures are traditionally composed of thin membranes filled with a lifting gas. If the density of the lifting gas,  $\rho_{lg}$ , is less than the density of the air it displaces,  $\rho_{air}$ , the lifting gas is said to have positive buoyancy. If the buoyant force,  $L_b$ , of an object as calculated by equation (5) [8, p. 15], is greater than the weight of that object, then the object is said to have positive buoyancy. In order to build a LTA vehicle, the weight of the structure, to include fuel and engines, must be less than  $L_b$  as shown in equation (4), otherwise the vehicle will not have positive buoyancy. The dominant weight in equation (4) is due to the mass of the structure,  $m_s$ . The design of a vacuum LTA structure is primarily concerned with reducing the weight of the structure as far below  $L_b$  as possible. In order to determine  $m_s$ , the geometric and material properties of the structure must be evaluated such as geometric stability and material failure.

A vacuum LTA structure is one in which a partial vacuum is used instead of a lifting gas. Considering equation (5), the density of the lifting gas would be determined by the ideal gas law, (12) [1].

$$\rho_{lg} = \frac{p_{lg}}{R \cdot T} \quad (12)$$

Where:

$R$  = specific gas constant

$T$  = temperature

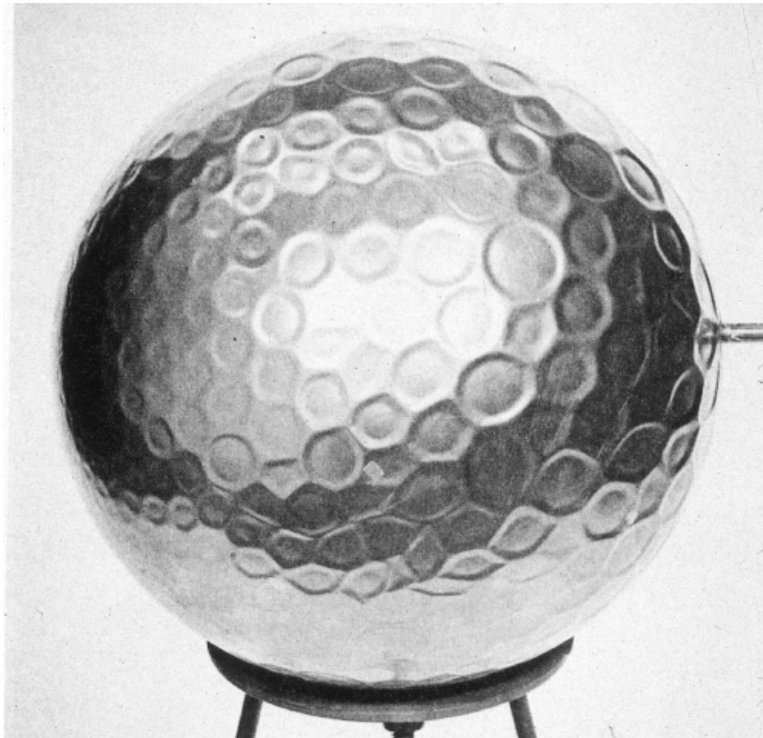
$p_{lg}$  = lifting gas pressure

As lifting gas pressure  $p_{lg}$  approaches zero, lifting gas density  $\rho_{lg}$  also approaches zero. The pressure of the lifting gas in a traditional LTA structure is generally greater than the ambient air pressure [13, pp. 160-170]. This results in skin tension which adds stability to the structure. The reverse is true in the case of a structure that contains a vacuum. In this case the external pressure on the structure places the skin under compression, which destabilizes the structure. Structural failure, in the case of an externally loaded thin shell, can occur in two ways. Buckling is the first, and exceeding the material elastic limit is the second.

Buckling is defined as an inordinately large displacement under conditions of unstable equilibrium [4, p. 134]. A thin shell in compression is a condition of unstable equilibrium because the shell has the potential to snap through locally as shown in Figure 10 [29]. Figure 10 has multiple regions of local buckling instead of one large region due to artificial stability provided by a solid internal mandrel. After buckling, a structure will continue to displace under lower loads than the critical load at which buckling first occurred. If buckling occurs there will be two primary consequences. One is material failure, to be discussed subsequently. The other is decreased internal volume, which will reduce buoyancy. This buoyancy reduction can be sudden if buckling occurs and could

result in instant loss of positive buoyancy. Therefore the structure must avoid buckling if it is to continue to accomplish its mission.

**Figure 10: Buckled Sphere [29]**



The critical buckling pressure  $p_{crit}$  of a homogeneous, thin walled, sphere under uniform external pressure, is shown in equation (13) [30, p. 5] which is based on classical buckling theory. In practice a knockdown factor is used in conjunction with equation (13) to match experimental results. This is necessary because any deviation from a perfect sphere, as shown in Figure 11 [30, p. 11], results in a lower  $p_{crit}$  than theory predicts. Figure 11 [30, p. 11] shows the knockdown factor for the buckling pressure of a prolate spheroid plotted against fineness ratio. A prolate spheroid is a body of revolution similar in shape to a blimp in which one axis of the spheroid is longer than the other, and the

long axis is the axis of revolution. An absolutely perfect sphere would match classical buckling theory, but even minor deviations cause a rapid drop off in  $p_{crit}$  as shown in Figure 11. Classical buckling theory was also used in equation (14) [4, p. 1292], but with the addition of an empirical knockdown factor of about 0.7 that gives a more conservative prediction of  $p_{crit}$ . A knockdown factor of 0.7 was recommended by Krenzke [31, p. 14] after experimental analysis of near perfect spherical caps gave a knockdown factor of 0.73 and 0.9 of that predicted by classical theory [31, p. 9].

$$p_{crit} = 2 \cdot \frac{E}{\sqrt{3(1-\nu^2)}} \cdot \left(\frac{t_{skin_s}}{r_s}\right)^2 \quad (13)$$

$$p_{crit} = 0.8 \cdot \frac{E}{\sqrt{1-\nu^2}} \cdot \left(\frac{t_{skin_s}}{r_s}\right)^2 \quad (14)$$

Where:

$E$  = Young's Modulus of Elasticity

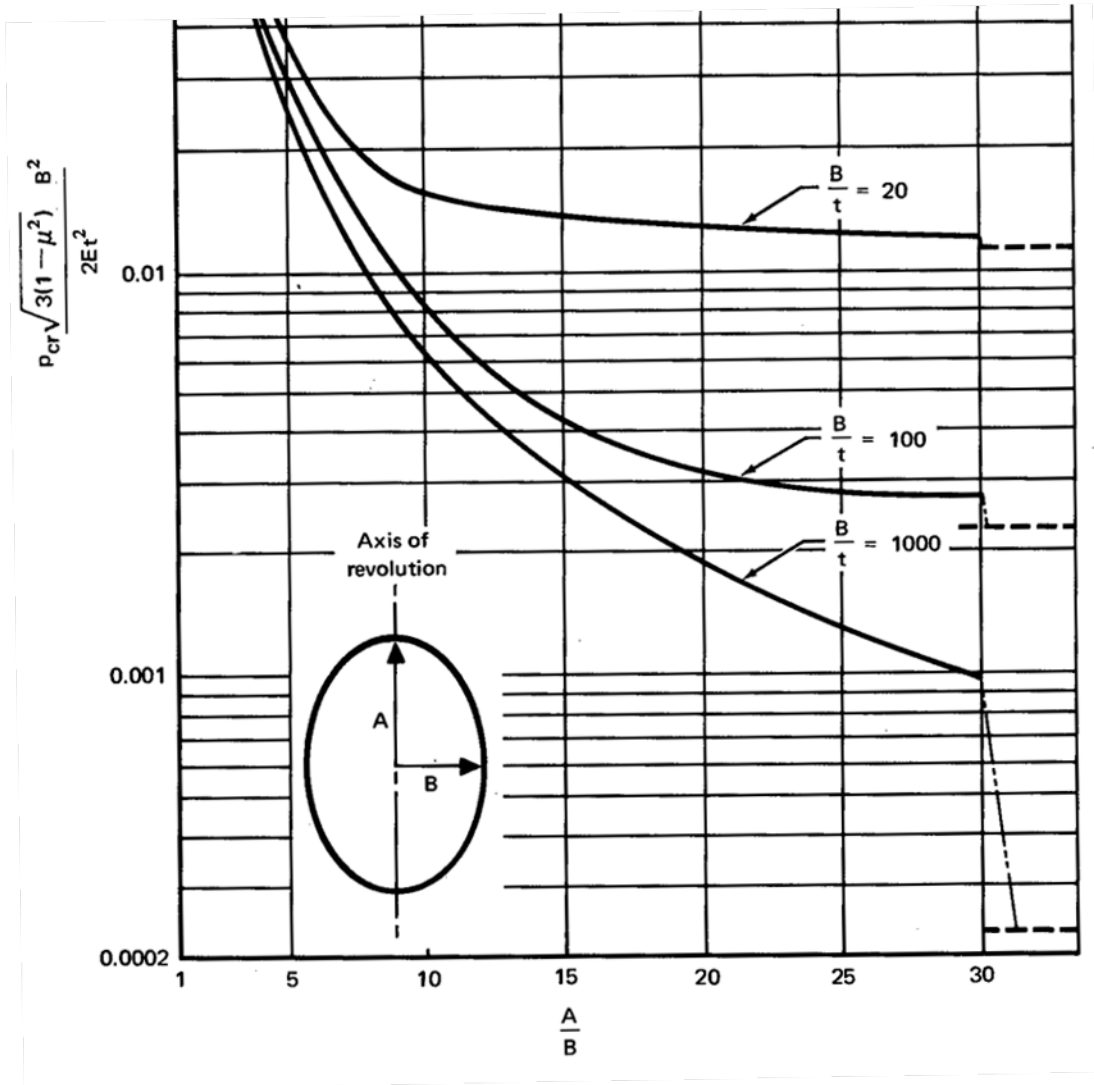
$t_{skin_s}$  = sphere skin thickness

$p_{crit}$  = critical pressure

$r_s$  = sphere radius

$\nu$  = Poisson's Ratio

Figure 11: Prolate Sphere [30]



The second way in which structural failure can occur is when the elastic limit of a material is exceeded. In order to ensure a sphere will not collapse due to material failure, equation (15) [4, p. 124] must also be satisfied. This was derived by setting the compressive yield strength of the sphere equal to the load divided by the cross sectional area as shown in equation (16).

$$p_{crit} \approx \frac{2 \cdot \sigma_{cy} \cdot t_{skin_s}}{r_s} \quad (15)$$

$$\sigma_{cy} = \frac{p_{crit} \cdot a_{circ}}{a_{skin}} \quad (16)$$

$$a_{circ} = \pi \cdot (r_s + t_{skin_s})^2 \approx \pi \cdot r_s^2 \quad (17)$$

$$a_{skin} = 2 \cdot \pi \cdot r_s \cdot t_{skin_s} \quad (18)$$

Where:

$a_{circ}$  = cross sectional area of great circle of sphere

$a_{skin}$  = cross sectional area of sphere skin

$\sigma_{cy}$  = material compressive yield strength

A sphere that can achieve positive buoyancy using a vacuum must have a mass less than the air it displaces, and satisfy the thickness and material property requirements of equations (14) and (15). The mass of a spherical, homogeneous structure can be determined by multiplying the density of the skin by the volume of its skin. Equation (19) gives the mass of a spherical structure and is the area of a sphere multiplied by its thickness and density.

$$m_s = \rho_s \cdot t_{skin} \cdot a_s \quad (19)$$

$$a_s = 4 \cdot \pi \cdot r^2 \quad (20)$$

Where:

$a_s$  = surface area of sphere

$m_s$  = mass of structure

$t_{skin}$  = skin thickness

$\rho_s$  = density of sphere wall

The volume of a sphere is shown in equation (21) [5]. Inequality (22) is based on a combination of equations (14), (19), and (21), by setting the  $W/B \leq 1$ . This gives the required material properties for a homogeneous, thin walled sphere to achieve positive buoyancy in air.

$$v_s = \frac{4}{3} \cdot \pi \cdot r_s^3 \quad (21)$$

$$\frac{E}{\rho_s^2} \geq 11.25 \cdot p_{air} \cdot \frac{\sqrt{1 - \nu^2}}{\rho_{air}^2} \quad (22)$$

$$\frac{E}{\rho_s^2} \geq 7.25 \cdot 10^5 \frac{Pa}{\left(\frac{kg}{m^3}\right)^2} \quad (23)$$

By assuming standard atmosphere at sea level and  $\nu = 0.3$ , inequality (22) reduces to inequality (23) [32] which can be used to determine whether a material would be capable of achieving positive buoyancy using a vacuum at sea level. The value in inequality (23) is stiffness over density squared, which shows that the desired material properties for a thin shelled sphere are a low density and a high stiffness. The same approach was taken

in [5] where the value of inequality (23) was found to be  $4.5 \cdot 10^5$ . This is less conservative than the value in inequality (23) due to the use of the classical buckling theory without a knockdown factor as shown in equation (13).

A survey of published material properties indicated that there was no material available that meets the requirements of inequality (23). The material properties of two materials, where the fourth column is the left side of inequality (23), are shown in Table 4. The pitch based fiber represents the highest specific stiffness composite material, and beryllium the highest specific stiffness isotropic material available on open source material data bases such as Matweb [33]. As Table 4 shows, neither material achieves a specific modulus high enough to satisfy the requirements of inequality (23). There are two rows devoted to Dupont E-130-X Pitch Based UHM Carbon Fiber. The first shows the longitudinal stiffness for unidirectional fiber. Isotropic properties are assumed for equation (14), so the fiber stiffness cannot be used directly. A  $[(0/\pm 45/90)]_s$  ply has quasi-isotropic properties but the effective stiffness is about 38% of the unidirectional composite axial stiffness [34, p. 143]. This value was calculated using laminate theory which was beyond the scope of this study. However, a simple estimation approach is often used for aerospace applications that gives nearly identical results to laminate theory. This method uses the rule of mixtures and reinforcing efficiency as described in [35]. The rule of mixtures states that the stiffness of the composite material is equal to the combined stiffness of the fibers and matrix times their respective volume fractions as shown in equation (24). Volume fraction is the fraction of the total volume of the composite composed of either fiber ( $V_f$ ) or matrix ( $V_m$ ). In the case of carbon epoxy the carbon fibers can make up as much as 60% of the composite volume, resulting in a

$V_f = 0.6$  and a  $V_m = 0.4$ . The fiber reinforcing efficiency,  $\eta_\theta$ , is based on the angle of fibers and their volumetric portion of total fiber content as shown in equation (25). For a  $[(0/\pm 45/90)]_s$  ply, which gives  $\eta_\theta = 0.375$  according to equation (25), with fiber stiffness  $E_f = 895$  GPa, and matrix stiffness  $E_m = 3.5$  GPa at  $V_f = 0.6$ , equation (29) gives a composite stiffness of  $E_c = 0.375 \cdot 895 \cdot 0.6 + 3.5 \cdot 0.4 = 202$  GPa. This value is reflected in the second row of Table 4. As a point of comparison to laminate theory as used in [34], which gave a quasi-isotropic stiffness of 38.2% of the unidirectional stiffness, the quasi-isotropic stiffness calculated using equations (24) and (25) of 202 GPa was 27.5% of the unidirectional composite stiffness of 538 GPa.

$$E_c = \eta_\theta E_f V_f + E_m V_m \quad (24)$$

$$\eta_\theta = \sum_1^n a_n \cdot \cos^4 \theta \quad (25)$$

Where:

$a_n$  = proportion of total fiber content

$E_c$  = composite stiffness

$E_f$  = fiber stiffness in fiber direction

$E_m$  = matrix stiffness

$V_m$  = volume fraction of matrix

$V_f$  = volume fraction of fiber

$\eta_\theta$  = Krenchel efficiency factor

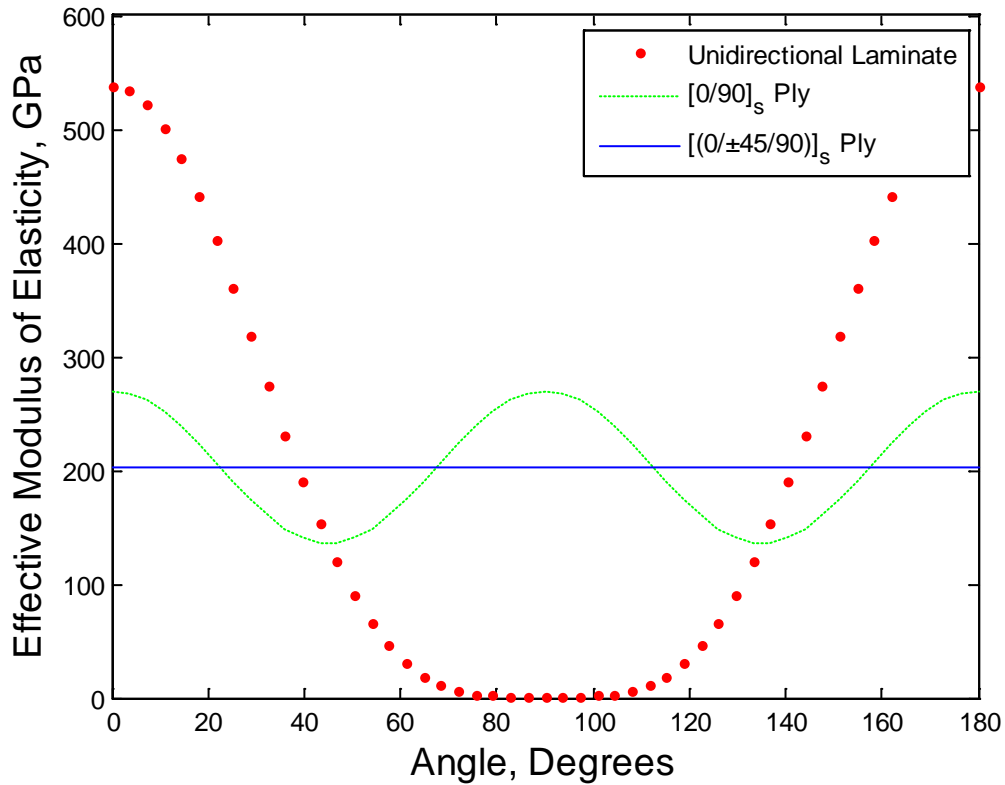
$\theta$  = angle of fibers

**Table 4: Material Properties-Monocoque Shell**

<b>Material from Matweb</b>	<b>E, Pa</b>	$\frac{\rho_s, \text{kg}}{\text{m}^3}$	$\frac{E}{\rho_s^2}$	<b>Smooth Sphere W/B</b>	<b>Comments</b>
Dupont E-130-X Pitch Based UHM Carbon Fiber	$895 \cdot 10^9$	2130			
$[(0/\pm 45/90)_2]_s$	$202 \cdot 10^9$	1522	$8.7 \cdot 10^4$	3.5	Composite
Beryllium SR-200	$303 \cdot 10^9$	1840	$8.9 \cdot 10^4$	3.6	Isotropic metal

The  $[(0/\pm 45/90)]_s$  ply was chosen because it is quasi-isotropic. This means that in the plane of the laminate it gives equal material properties in every direction. The stiffness of composites made of Dupont E-130-X carbon fiber for various angles with respect to the axial direction as calculated by equations (29) and (30) are shown in Figure 12. These curves show that a unidirectional laminate is very stiff in the axial direction, but the quickness quickly drops off at other orientations. If a unidirectional laminate, or even a  $[0/90]_s$  ply were used to construct a sphere there would be directions of high stiffness and directions of low stiffness that would invalidate the assumptions of equation (14).

Figure 12: Laminate Stiffness as a Function of Orientation

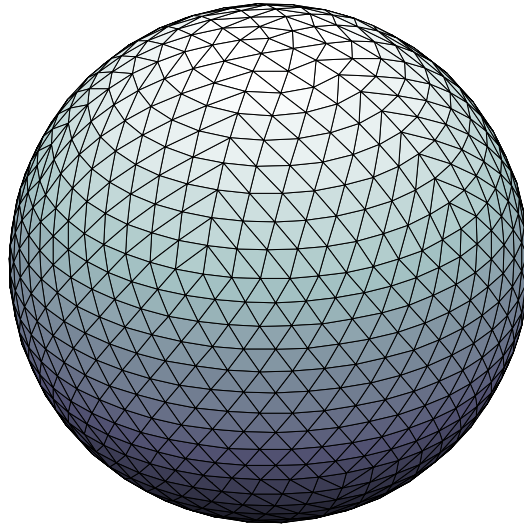


Spheres under external pressure may fail at much less than the critical pressure of a perfect sphere, or even less than the knockdown factor of 0.7 [31, p. 1]. Geometric stiffeners and increased thickness help reduce this imperfection sensitivity [29]. Considering that no materials can enable a thin shelled sphere to achieve positive buoyancy, and that even what can be achieved is highly susceptible to small imperfections, another method is required to accomplish the goals of this thesis. For this reason geometry became the dominant factor in the search for a structure that could achieve positive buoyancy in air using a vacuum.

## 2.4 Isogrid

Grid stiffened structures consist of a thin skin, as in the thin shelled sphere evaluated above, with a grid of stiffeners attached to the skin. If the grid is arranged in such a way that the stiffening ribs transmit forces equally in all directions tangent to the skin, it is called an isogrid. An isogrid structure can be treated as an isotropic material which enables the use of isotropic equations such as equation (14) [36, p. 2.0.001]. The grid is generally arranged in equilateral triangles. When applied to a spherical surface they can be arranged in the form of a geodesic sphere as shown in Figure 13.

**Figure 13: Grid Stiffened Sphere,  $f=10$**



## 2.5 Geodesic Sphere

Geodesic spheres are geometric shapes that approximate a sphere using straight lines along the great circles of a sphere as shown in Figure 13. Buckminster Fuller was granted a patent for his geodesic dome design on 12 Dec 1951 [37]. In his patent, Fuller

described a geodesic sphere based on a 20 sided polyhedron called an icosahedron. The icosahedron, shown in Figure 14, is a polyhedron composed of 20 equilateral triangles in which each vertex lies on the surface of an imaginary sphere (shown as dashed circle). Each face of the icosahedron is referred to as a major triangle. To form more complex geometric structures that more closely approximate a sphere, the major triangles are subdivided into smaller triangles. The vertices of the minor triangles that subdivide the major triangles also lie on the surface of the sphere that circumscribes the vertices of the original icosahedron. The number of divisions along one edge of each major triangle is referred to as geometric frequency ( $f$ ). A geodesic sphere with  $f=2$  is one in which the edges of each major triangle are divided into two as shown in Figure 15. An increase in  $f$  results in increasingly more complex structures. Note that increasing  $f$  beyond 1 results in a geodesic structure composed entirely of irregular triangles, whereas the original icosahedron is entirely composed of equal sized equilateral triangles. This point becomes important when evaluating loading of the geodesic sphere, because there is perfect symmetry in an icosahedron, but not on more complex geodesic spheres.

**Figure 14: Geodesic Sphere  $f=1$  (Icosahedron)**

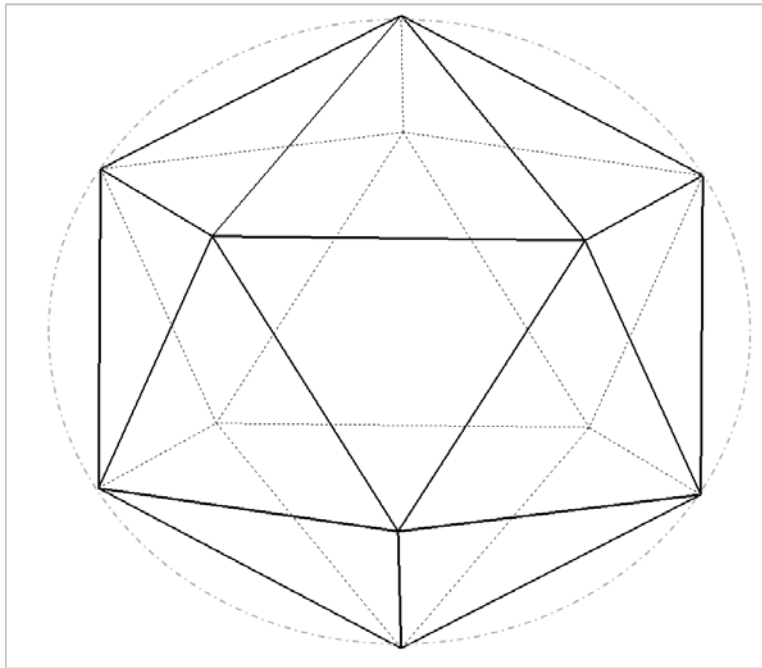
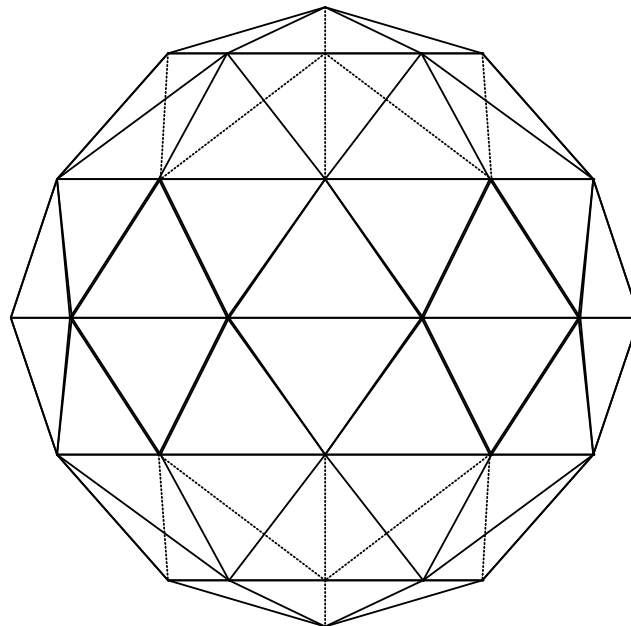


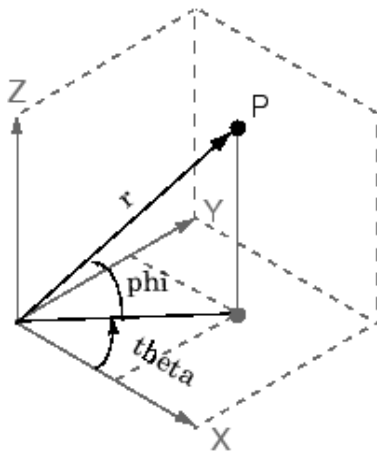
**Figure 15: Geodesic Sphere  $f=2$**



A Matlab program titled `LTAgeod.m`, Appendix A.4, was used to create Figure 13, Figure 14, and Figure 15. This program generated the geodesic sphere geometry by

starting with an icosahedron and subdividing each major triangle according to  $f$ . All coordinates were generated in spherical coordinates, but later converted to cartesian for use in a Finite Element Analysis (FEA) program. Spherical coordinates are defined in the Matlab `sph2cart.m` help file according to Figure 16 [38], and are composed of  $\theta$ ,  $\phi$ , and  $r$ . A point in spherical coordinates is defined by a vector that has length  $r$ , and direction defined by  $\theta$  and  $\phi$ . The angle  $\theta$  is measured counterclockwise in the  $xy$  cartesian plane from the  $x$  axis to the position vector. The angle  $\phi$  is measured between the position vector and the  $xy$  cartesian plane as shown in Figure 16.

**Figure 16: Spherical to Cartesian Conversion in Matlab [38]**



$$\begin{aligned} x &= r \cdot \cos(\phi) \cdot \cos(\theta) \\ y &= r \cdot \cos(\phi) \cdot \sin(\theta) \\ z &= r \cdot \sin(\phi) \end{aligned}$$

The spherical coordinates for the vertices of an icosahedron with center at the origin are listed in Table 5. Every vertex of an icosahedron lies on the surface of an imaginary sphere. By placing the center of the sphere at the origin, the coordinates of every point on the surface of the sphere, to include the vertices of the icosahedron, are at  $r = r_s$ .

Point	$\theta$ (radians)	$\phi$ (radians)	r (meters)
1	0	$\pi/2$	$r_s$
2	0	0.464	$r_s$
3	$2\pi/5$	0.464	$r_s$
4	$4\pi/5$	0.464	$r_s$
5	$6\pi/5$	0.464	$r_s$
6	$8\pi/5$	0.464	$r_s$
7	$\pi/5$	-0.464	$r_s$
8	$3\pi/5$	-0.464	$r_s$
9	$\pi$	-0.464	$r_s$
10	$7\pi/5$	-0.464	$r_s$
11	$9\pi/5$	-0.464	$r_s$
12	0	$-\pi/2$	$r_s$

The coordinates in Table 5 were derived with the knowledge that an icosahedron is composed of 20 equilateral triangles with vertices circumscribed by a sphere. The center of the icosahedron was placed at the origin with the z axis going through the top and bottom vertices. Thus the top and bottom vertices are defined by  $\phi = \pm \frac{\pi}{2}$  and  $\theta = 0$ . The rest of the vertices lie on one of two planes equidistant from the xy cartesian plane, each plane containing 5 points of constant  $\phi$  that make up a pentagon. The top plane is positive  $\phi$ , the bottom plane is negative  $\phi$ . Therefore  $\phi$  only has to be calculated once. The complete mathematical derivation for an icosahedron was beyond the scope of this thesis, however starting from the relationship between the length of the edge of a major triangle ( $a$ ), and the radius of the circle ( $r_s$ ) as shown in (26) [39], the derivation of  $\phi$  was fairly straight forward. By cutting an icosahedron in half using a plane on the z axis that passed through a vertex on the top pentagon as shown in Figure 17, the angle  $\phi$  for the points on the top and bottom pentagon were determined. The two dimensional view of the cut icosahedron is shown in Figure 18. The angle  $\phi$  can be found using the triangle

formed between two vertices of the icosahedron and the origin. This triangle has two legs of length  $r_s$  and one leg of length  $a$  as shown in Figure 18. The angle opposite the leg of length  $a$  was determined by the law of cosines as shown in equation (27) [40], and came out to be  $\cos^{-1}\left(\frac{\sqrt{5}}{5}\right) \cong 1.107$ . Therefore,  $\phi = \frac{\pi}{2} - 1.107 \cong 0.464$ .

$$r = a \cdot \sin \frac{2\pi}{5} \quad (26)$$

$$leg_1^2 = leg_2^2 + leg_3^2 - 2 \cdot leg_2 \cdot leg_3 \cdot \cos(angle_1) \quad (27)$$

**Figure 17: Icosahedron-Cutting**

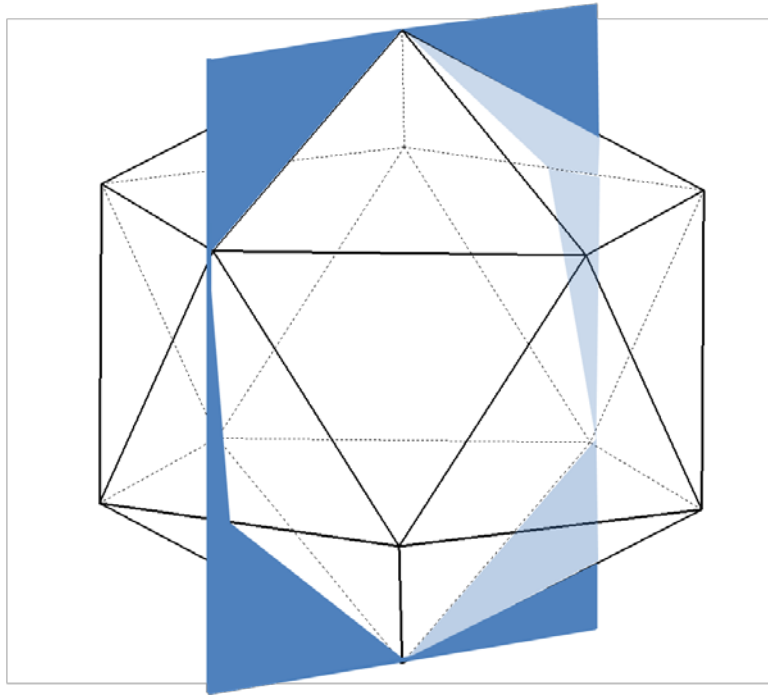
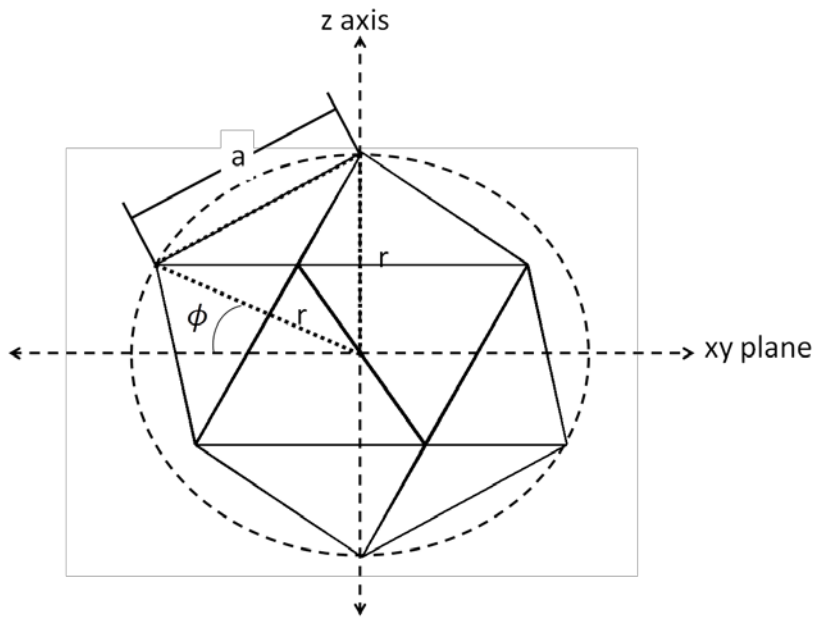
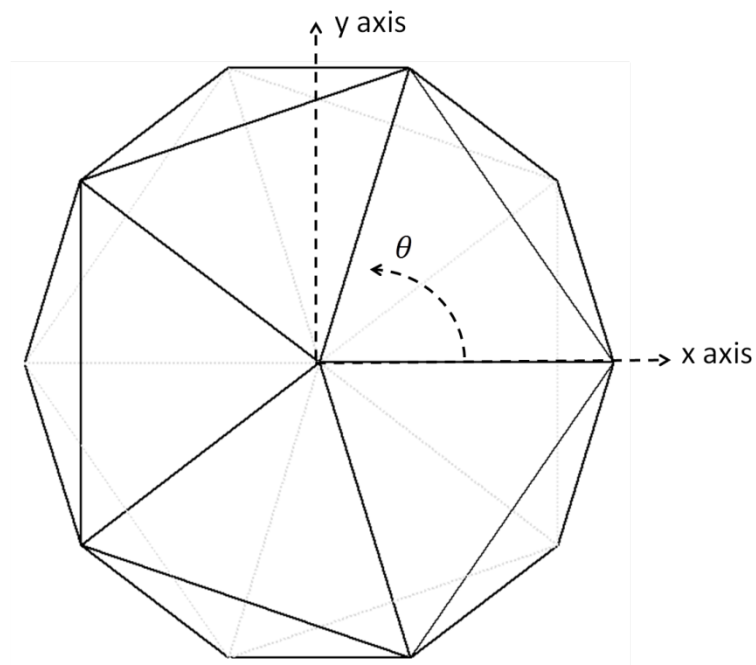


**Figure 18: Icosahedron-Cut**



The angle  $\theta$  was easier to calculate. Looking at the icosahedron from top down, as in Figure 24, it is apparent that each pentagon divides the circle into five equal angles. Therefore,  $\theta$  comes in multiples of  $2 \cdot \pi/5$ . The first vertex on the top pentagon is placed on the x axis so that  $\theta = 0$ . The following vertices on the top pentagon are at  $\theta = 2 \cdot \pi/5$ ,  $\theta = 4 \cdot \pi/5$ ,  $\theta = 6 \cdot \pi/5$  and so on for each of the five vertices on the top pentagon. The top and bottom pentagon are offset from each other so that each angle on the bottom pentagon bisects the two closest angles on the top pentagon as shown in Figure 19. Therefore  $\theta$  on the bottom pentagon starts at  $\theta = \pi/5$  and increases by increments of  $2 \cdot \pi/5$  for each subsequent vertex.

**Figure 19: Icosahedron-Top View**



The number of vertices ( $n_v$ ), edges ( $n_e$ ), and triangular faces ( $n_t$ ) of a geodesic

structure as a function of  $f$  are calculated using equations (28) - (30) [41]. An icosahedron has an  $f=1$ , which gives 12 vertices, 30 edges, and 20 triangles using equations (28) - (30). These equations show that as  $f$  increases, the complexity of a sphere increases significantly. The number of vertices, edges, and triangles were used to check the program LTAgeod.m, Appendix A.4 for accuracy, and for weight calculations when solving for W/B.

$$n_v = 10 \cdot f^2 + 2 \quad (28)$$

$$n_t = 20 \cdot f^2 \quad (29)$$

$$n_e = 30 \cdot f^2 \quad (30)$$

## 2.6 Summary

A literature review was conducted that covered each of the elements required to evaluate a vacuum LTA vehicle. These elements included general LTA vehicle aspects as they pertained to the problem of constructing a vacuum LTA vehicle. These included historical structures, missions, and potential areas for improving on historical designs. Thin shelled spheres were examined which showed the critical material properties for building a vacuum LTA structure, as well as demonstrated the need for geometric

methods of preventing buckling. Isogrid stiffened spheres and geodesic geometry were introduced as possible methods of preventing buckling without adding significant weight.

### **III. Methodology**

#### **3.1 Chapter Overview**

This chapter introduces the rotating cylinder LTA vehicle concept and the methods used to evaluate its feasibility. These include buoyancy, weight, aerodynamics, power requirements, and engine and fuel weight. Also explained are the equations from the NASA Isogrid Handbook [36] and the equations and methods behind the programs used to optimize the geodesic sphere.

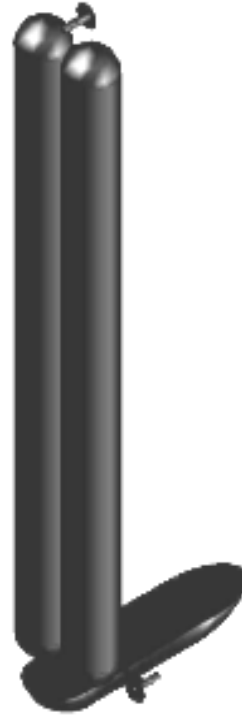
#### **3.2 Rotating Cylinder Vacuum LTA Vehicle Concept**

A preliminary investigation into the feasibility of constructing a thin shelled, unreinforced structure that achieved positive buoyancy in air using a vacuum, showed that there was no material in existence by which such a structure could be formed. Therefore, it became apparent that the structure would need to be stiffened geometrically or by some other means. One method of stiffening the structure was inspired by helicopter rotor blades. Helicopter blades are highly flexible and free to flap vertically due to a pinned-free boundary condition, but due to high rotational velocity they become resistant to vertical movement and can support great loads. This same concept was applied to the vacuum structure by investigating long cylinders rotated about their axis of symmetry. If these cylinders were rotated at a sufficient velocity, the centripetal force exerted by the skin would produce a hoop tensile stress that would counteract the hoop

compressive stress in the skin produced by atmospheric pressure. To put this simply, resisting atmospheric pressure pushes the skin towards the center while inertia pulls the skin away from the center. The assumption was made that dynamic effects would not interfere with the balance between inertial and pressure forces. This assumption would need to be verified through simulation or experiment, but it allowed energetic evaluation of the rotating cylinder idea. If the rotating cylinder proved energetically feasible, the next logical step would be to evaluate the dynamic effects of rotating a long, slender cylinder. Assuming perfect balance between all radial forces, energy requirements were evaluated based on drag torque, bearing friction, turbine engine efficiency, propeller efficiency, and power required to overcome translational drag.

A theoretical vehicle, Figure 20, was proposed that consisted of two counter-rotating cylinders mounted vertically above a gondola. The gondola would have two propellers capable of thrust vectoring. At the top of the counter-rotating cylinders would be a third propeller which would be used to trim the vehicle to keep the rotating cylinders perpendicular to the airflow. The buoyancy, weight, aerodynamic, and power characteristics of this vehicle were evaluated to determine whether it was a feasible concept. This vehicle concept was called the Rotating Cylinder, Vacuum LTA Vehicle (RCVLTAV). Each cylinder was proposed to be a smooth, thin shelled structure with spherical end-caps similar to commercial pressure vessels designed to contain compressed gas.

**Figure 20: Rotating Cylinder Vehicle**



### ***3.2.1 Buoyancy and Weight***

The buoyant force of the theoretical structure was determined using equation (31) by calculating the volume of each cylinder with equation (32) [42], and the volume of the spherical end-caps with equation (33) [42]. Both cylinders were designed to be of equal dimensions. The buoyant force of a cylinder with spherical end-caps is the mass of air displaced by the cylinder and end-caps as shown in equation (31).

$$L_{b_c} = g \cdot \rho_{air} \cdot (v_c + v_s) \quad (31)$$

$$v_c = \pi \cdot l_c \cdot r_c^2 \quad (32)$$

$$v_s = \frac{4}{3} \cdot \pi \cdot r_c^3 \quad (33)$$

$L_{bc}$  = buoyant force of cylinder with spherical endcaps  
 $v_c$  = cylinder volume  
 $v_s$  = spherical endcap volume

After calculating the buoyancy of a given set of cylinders, the thickness of the cylinder walls was determined based on equation (34) which was derived from equations (35) - (37) [4]. These equations prevent buckling of the cylinder due to the axial load on the cylinder caused by atmospheric pressure on the spherical end-caps as depicted in Figure 21. The axial force on a cylinder due to pressure on the spherical end-caps minus the buoyant force is shown in equation (35). The reason the buoyant force is subtracted from the axial load is that the payload of the cylinder hangs from one end, thus placing the cylinder in tension by an amount equal to the buoyant force. Equation (36) is the equation for the buckling end load of a hollow, cylindrical column with free-free boundary conditions. Using the end-load calculated in equation (35), the required thickness for the cylinder was found using equations (36) and (37) [4, p. 1296]. The symbolic solution to these equations is shown as equation (34). The compressive yield stress of the cylinder material was compared to equation (38) [4]. Cylinder skin thickness,  $t_{skin_c}$ , was chosen to satisfy both equations (34) and (38). End-cap thickness,

$t_{skin_s}$ , was chosen to satisfy equation (14). Material properties were based on UHM carbon epoxy as shown in Table 7.

$$t_{skin_c} = \left( \sqrt{\frac{64 \cdot r_c^6}{27} + \frac{4 \cdot F_a^2 \cdot l_c^4}{\pi^6 \cdot E^2 \cdot r_c^2} + \frac{2 \cdot F_a \cdot l_c^2}{\pi^3 \cdot E \cdot r_c}} \right)^{\frac{1}{3}} + \left( -\sqrt{\frac{64 \cdot r_c^6}{27} + \frac{4 \cdot F_a^2 \cdot l_c^4}{\pi^6 \cdot E^2 \cdot r_c^2} + \frac{2 \cdot F_a \cdot l_c^2}{\pi^3 \cdot E \cdot r_c}} \right)^{\frac{1}{3}} \quad (34)$$

$$F_a = p_{atm} \cdot \pi \cdot r_c^2 - L_{b_c} \quad (35)$$

$$F_a = \frac{\pi^2 \cdot E \cdot I}{l_c^2} \quad (36)$$

$$I = \pi \cdot \left( r_c \cdot \frac{t_{skin}^3}{4} + t_{skin_c} \cdot r_c^3 \right) \quad (37)$$

$$\sigma_a = \frac{F_a}{2 \cdot \pi \cdot r_c \cdot t_{skin_c}} \quad (38)$$

Where:

$F_a$  = axial force on cylinder

$r_c$  = cylinder radius

$v_c$  = cylinder volume

$m_c$  = cylinder mass

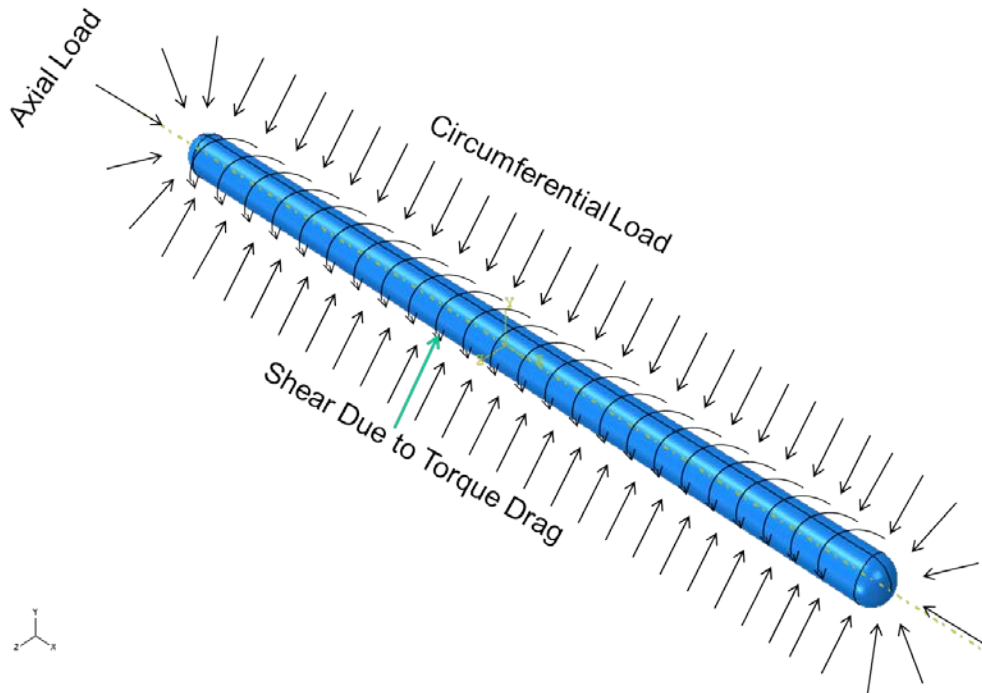
$l_c$  = cylinder length

$t_{skin_c}$  = cylinder skin thickness

$t_{skin_s}$  = sphere skin thickness

$\sigma_a$  = axial stress

**Figure 21: Rotating Cylinder Loads**



After determining  $t_{skin_c}$  and  $t_{skin_s}$ , it was possible to calculate the mass of each cylinder using equation (39) where the area of the cylinder and spherical end-caps were calculated with equations (40) and (41) [42]. The assumption was made in equation (39) that there was an absolute vacuum inside of each cylinder. This assumption provided reasonable results, even though an absolute vacuum can not be practically achieved. A very low pressure, such as 10 tor, would result in negligible weight and pressure differences. The final assumption was the basic premise behind the RCVLTA. Structure walls were assumed to be able to withstand external pressure due to rotational velocity alone.

$$m_c = \rho_{skin} \cdot (t_{skin_c} \cdot a_c + t_{skin_s} \cdot a_s) \quad (39)$$

$$a_c = 2 \cdot \pi \cdot r_c \cdot l_c \quad (40)$$

$$a_s = 4 \cdot \pi \cdot r_c^2 \quad (41)$$

Where:

$a_c$  = cylinder area

$a_s$  = spherical endcap area

$m_c$  = cylinder mass

The inertial properties of the cylinder walls were based on  $t_{skin_c}$  and  $\rho_{skin}$ , which enabled calculation of the required rotational velocity using equation (45). This equation was derived using equations (42) - (44). The total force due to atmospheric pressure ( $F_p$ ) was calculated using equation (42) by multiplying the surface area of the cylinder by  $p_{atm}$ . Centripetal force due to rotational velocity, was used to determine the required rotational velocity ( $\omega$ ) for  $F_c$  to equal  $F_p$  using equation (43) [43]. The cylinder mass was calculated using the surface area of a cylinder times the skin thickness and density as shown in equation (48). The derivation of equation (45) was accomplished by substituting the right side of equation (43) for  $F_p$  in equation (42). The buckling pressure ( $p_{cr}$ ) of the stationary cylinder was calculated using equations (46) - (50), [4, p. 1299]. The derivation of equations (46) - (50) are beyond the scope of this study, but can be

found in [44]. The amount of pressure that had to be countered using  $F_c$  was reduced by  $p_{cr}$  from equation (45). It turned out that at thickness that allowed a  $W/B < 1$ ,  $p_{atm}$  was about four orders of magnitude greater than  $p_{cr}$ . Because of this the effect of increasing thickness was negligible and the centripetal force  $F_c$  was necessary to counteract practically the entire load due to  $p_{atm}$ .

$$F_p = 2 \cdot \pi \cdot r_c \cdot l_c \cdot p_{atm} \quad (42)$$

$$F_c = m_c \cdot r_c \cdot \omega^2 \quad (43)$$

$$m_c = 2 \cdot \pi \cdot r_c \cdot l_c \cdot t_{skin_c} \cdot \rho_{skin} \quad (44)$$

$$\omega = \sqrt{\frac{p_{atm} - p_{cr}}{r_c \cdot t_{skin_c} \cdot \rho_{skin}}} \quad (45)$$

$$p_{cr} = \sigma_{cr} \frac{t_{skin_c}}{r_c} \quad (46)$$

$$\sigma_{cr} = \frac{K_c \pi^2 E}{12(1 - \nu^2)} \left( \frac{t_{skin_c}}{l_c} \right)^2 \quad (47)$$

$$K_c = 10^K \quad (48)$$

$$K = 0.6337 - 0.1455 \cdot \log^3 z - 0.01915 \cdot \log^3 z \quad (49)$$

$$z = \frac{l_c^2}{r_c \cdot t_{skin_c}} \cdot \sqrt{1 - v^2} \quad (50)$$

Where:

$a_s$  = spherical endcap area

$F_c$  = centripetal force

$F_p$  = force due to atmospheric pressure

$p_{cr}$  = critical pressure

$\sigma_r$  = radial stress due to external pressure

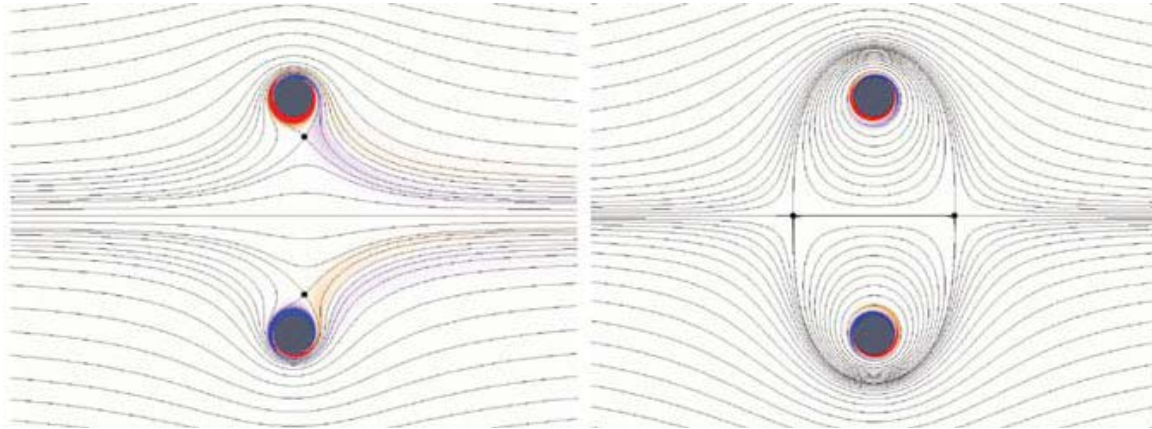
$\omega$  = rotational velocity

### 3.2.2 Aerodynamics

The cross section of a pair of infinitely long counter rotating cylinders with streamlines flowing past them from left to right is shown in Figure 22 [45, p. 13]. The streamlines on the left show cylinders that are rotating at  $\Omega < \Omega_{crit}$ , where  $\Omega$  is defined in equation (80) as the ratio of cylinder surface speed  $u_r$  to freestream velocity  $u_\infty$ . The cylinders on the right show cylinders rotating at  $\Omega_{crit}$ , which is the rotational velocity at which the streamlines form a virtual elliptical body that produces no vortices and thus experiences zero translational drag. Gap size determines  $\Omega_{crit}$ , with smaller gap sizes corresponding to smaller  $\Omega_{crit}$ . Gap size is measured in cylinder diameters, so that a gap size of 1 corresponds to two cylinders whose closest points are one diameter apart. A pair

of cylinders with a gap size of 1 were determined to both numerically and experimentally to have  $\Omega_{\text{crit}} \cong 3$  [45, p. 13]. The cylinders require power to maintain their rotational velocity, which means drag is experienced in the rotational direction, but not in the horizontal direction. In Figure 22 the horizontal direction would be to the left, with  $u_\infty$  moving from left to right. The streamlines in Figure 22 were produced using a computer program, however pictures were taken during a physical experiment that showed the same formation of a virtual elliptical body [45, p. 14]. These pictures were taken at  $Re=150$ . Rotational drag is referred to as drag torque (M) because it is measured as a torque instead of as a force. An airship consisting of a properly spaced pair of counter rotating cylinders could conceivably achieve high forward velocities with low translational drag by forming a virtual elliptical body.

**Figure 22: Formation of Virtual Elliptical Body at Critical Velocity [45]**



$$\Omega = \frac{u_r}{u_\infty} \quad (51)$$

Where:

$u_r$  = cylinder tip speed

$u_{\infty}$  = free stream velocity (translational)

### 3.2.3 Power Requirements

The power required to rotate a cylinder in a stationary body of air is shown in equation (52) and is the combination of power required due to drag torque  $P_M$ , spherical endcap rotation  $P_s$ , and bearing friction  $P_b$ . Power required due to drag torque  $P_M$  was calculated using equation (53) [46], which is the rotational velocity times drag torque (M). Equation (54) [47, p. 370], was used to calculate M, where the rotational drag coefficient ( $C_{Dc}$ ) was calculated according to equation (55) [47, p. 370]. These equations were derived in [47] based on experimental analysis of high speed, rotating cylinders by Theodorson and aerodynamic theory by Prandtl and von Karman. Interestingly, Theodorson discovered that the rotational drag coefficient,  $C_{Dc}$ , of cylinders is independent of velocity even though his experiments ranged well above cylinder surface velocities of mach=1. The equation for Reynolds number in equation (56) [48, p. 10] is the same as the Reynolds number for an object translating through air, but instead of the length of the vehicle, the radius is used. These equations were used to calculate the power required to rotate a single cylinder in a stationary body of air, which is greater than the power required to rotate cylinders in a fully developed virtual elliptical body [45, p. 32]. The power reduction for a virtual elliptical body was considered below, but it was first necessary to find the power required to rotate cylinders without a fully developed elliptical body.

$P_b$  was calculated using equation (63) [49, p. 460].  $P_b$  is a function of bearing load ( $F_b$ ), bearing radius ( $r_b$ ),  $\omega$ , and coefficient of friction ( $C_{fb}$ ).  $F_b$  was assumed to be

the cylinder useful lift, which is the buoyant force of the cylinder minus its weight.  $r_b$  and  $C_{f_b}$  were found on a bearing vendor's website [50].

$P_s$  was calculated using equation (58), [47, p. 370] and was derived during the same study that produced equations (53) - (55). The spherical end-caps on the rotating cylinders were assumed to be rotating disks for drag purposes. The drag coefficient of a rotating disk ( $C_{m_s}$ ) was verified experimentally by [47] and shown in equation (59).

$$P_r = P_M + P_b + P_s \quad (52)$$

$$P_M = \omega \cdot M \quad (53)$$

$$M = C_{Dc} \cdot \rho_{air} \cdot u_R^2 \cdot \pi \cdot r_c \cdot l_c \quad (54)$$

$$\frac{1}{\sqrt{C_{Dc}}} = -0.6 + 4.07 \cdot \log_{10} Re \cdot \sqrt{C_{Dc}} \quad (55)$$

$$Re = \rho_{air} \cdot u_t \cdot \frac{r}{\mu} \quad (56)$$

$$P_b = C_{f_b} \cdot r_b \cdot \omega \cdot F_b \quad (57)$$

$$P_s = \frac{1}{2} \cdot C_{m_s} \cdot \rho_{air} \cdot \omega^3 \cdot r_c^5 \quad (58)$$

$$C_{m_s} = \frac{0.146}{Re^{0.2}} \quad (59)$$

Where:

$C_{Dc}$  = rotating cylinder drag coefficient

$C_{fb}$  = bearing coefficient of friction

$C_{m_s}$  = spherical endcap drag coefficient

$F_b$  = bearing load

$l_c$  = cylinder length

$M$  = rotating cylinder drag moment

$P_b$  = power required due to bearing friction

$P_M$  = power required due to torque drag

$P_s$  = power required due to spherical endcap rotational drag

$P_r$  = total power required to rotate cylinder

$r_b$  = bearing radius

$Re$  = Reynold's Number

$u_t$  = rotating cylinder tip speed

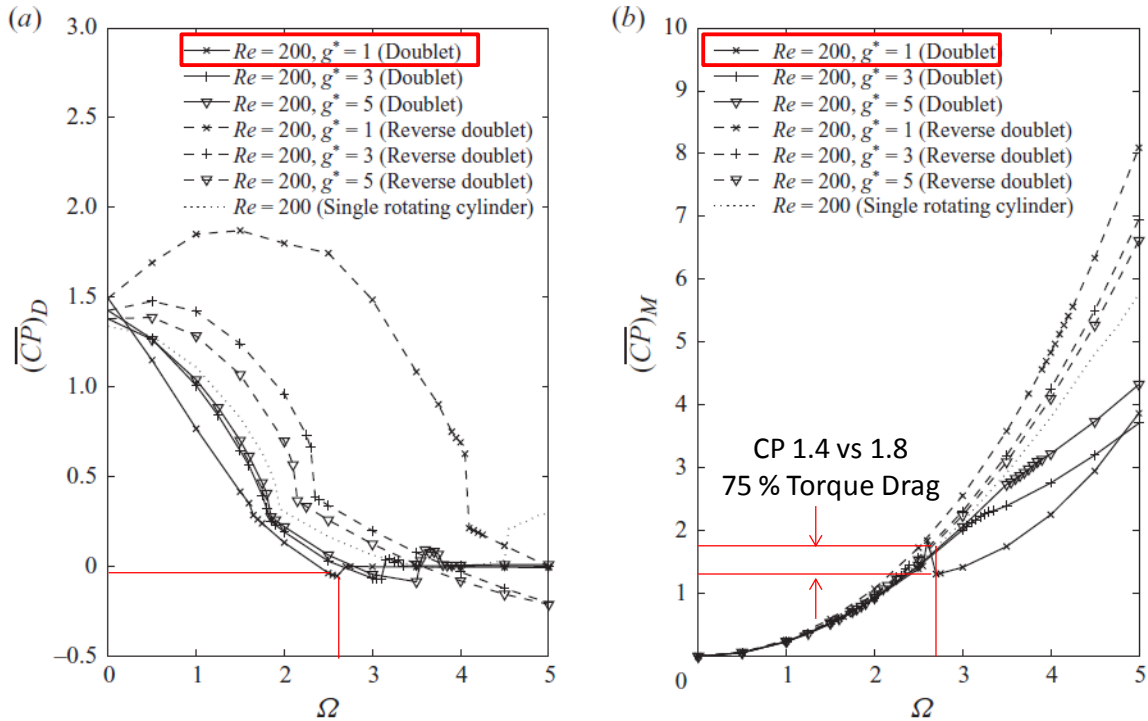
$\mu$  = air viscosity

$\omega$  = cylinder rotational velocity

Figure 23, [45] shows that as the gap size, displayed as  $g$  in Figure 23, between rotating cylinders decreases, the reduction in torque drag increases. Also, the critical tip speed  $u_r$  required to achieve the virtual elliptical body decreases as  $\Omega_{crit}$  decreases as in equation (51). The implication of this relationship is that the closer the cylinders are placed on the vehicle, the higher translational velocity the vehicle can achieve while maintaining a virtual elliptical body for a given cylinder rotational velocity, and the lower the torque drag (power required to rotate cylinders) that will be encountered. This research has not yet been conducted at gap sizes of less than 1 cylinder diameter. An

interesting area of future research would be to measure torque and translational drag on counter-rotating cylinders with gap sizes between 0 and 1 diameter to produce graphs similar to Figure 23.

**Figure 23: Reduction in Moment and Drag at Critical Rotational Velocity [45]**



### 3.2.4 Engine and Fuel Weight

After determining the translational velocity of a RCVLTAV based on equation (51) the vehicle payload ( $W$ ) was calculated using equation (60) assuming two counter-rotating cylinders with buoyant lift  $L_{cb}$ , a gondola the size of a C-27 cabin with mass  $m_g$ , 4 cylinder bearings with mass  $m_b$ , a turboshaft engine with enough power to rotate the cylinders and provide sufficient thrust to overcome the drag of the gondola with mass  $m_e$ , as well as enough fuel to travel 2130 km with mass  $m_f$ . It was assumed that no translational drag would be encountered by the rotating cylinders. Total power required

( $P_{tot}$ ) was used to determine fuel and engine requirements. Engine mass  $m_e$  was calculated using equation (61) which is an empirical formula for specific engine power for a turbo shaft engine [13, p. 225]. Fuel mass  $m_f$  was calculated using equation (62) which was derived based on the work required to fly 1852 km, the energy density of fuel ( $\zeta$ ), and engine efficiency ( $k_{ee}$ ).

Equation (63) was used to determine  $P_{tot}$ , which was assumed to be composed of the power required to spin two cylinders and the power required to counter translational drag ( $P_x$ ). Power required due to drag  $P_x$  was calculated using equation (64) which is the power equation for propellers with thrust equal to drag [25]. This is a function of propeller efficiency ( $k_{pe}$ ), propeller area ( $a_p$ ), thrust required, which in this case is the drag due to the gondola ( $D_g$ ) assuming steady level flight,  $u_\infty$ , and  $\rho_{air}$ . Gondola drag  $D_g$  was calculated based on gondola cross sectional area  $a_g$  (perpendicular to  $u_\infty$ ) and the gondola drag coefficient  $C_{dg}$ , [13]. The drag coefficient of the gondola  $C_{dg}$  was assumed to be the same as the average subsonic aircraft[51].

$$W = 2 \cdot L_{cb} - g \cdot (4 \cdot m_b + m_g + m_e + m_f) \quad (60)$$

$$m_e = P_{tot} \cdot 0.00201 \frac{\text{kg}}{\text{watt}} \quad (61)$$

$$m_f = \text{range} \cdot \frac{P_{tot}}{k_{ee} \cdot u_\infty \cdot \zeta} \quad (62)$$

$$P_{tot} = P_x + 2 \cdot P_r \quad (63)$$

$$P_x = k_{pe} \cdot \frac{D_g^2}{2 \cdot \rho_{air} \cdot a_p \cdot u_\infty} \quad (64)$$

$$D_g = \frac{1}{2} \cdot \rho_{air} \cdot u_\infty^2 \cdot a_g \cdot C_{dg} \quad (65)$$

Where:

$a_g$  = cabin cross sectional area perpendicular to  $u_\infty$

$a_p$  = propeller area

$C_{dg}$  = gondola drag coefficient

$D_g$  = gondola drag

$k_{ee}$  = engine efficiency

$k_{pe}$  = propeller efficiency

$m_b$  = bearing mass

$m_g$  = gondola mass

$P_{tot}$  = total power required for propellers and rotating cylinders

$P_x$  = power required due to cabin drag

$W$  = useful load

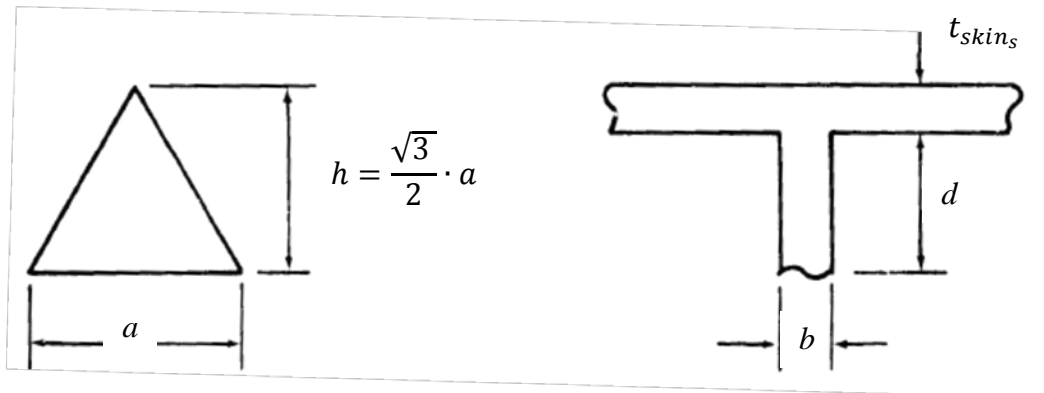
$\zeta$  = energy density of fuel

The calculation of  $W$  was necessary to determine the feasibility of the RCVLTA V concept. If  $W$  were negative the aircraft could not fly. If  $W$  were positive it could be used along with  $u_\infty$  and  $P_{tot}$  to calculate  $e_{VK}$ . Von Karman efficiency could then be used to compare the performance of the conceptual vehicle to existing vehicles.

### 3.3 Isogrid Stiffened Sphere

An isogrid acts like an isotropic, thin shelled structure, therefore equation (14) can be used to evaluate an isogrid stiffened sphere using equivalent thickness and stiffness. The NASA isogrid handbook [36] describes a simple isogrid composed of equilateral triangles as pictured in Figure 24, [36, p. 20.0.019].

Figure 24: Isogrid Geometry [36]



Where:

$t_{skin_s}$  = skin thickness

$d$  = flange height

$b$  = flange width

$h$  = triangle height

$a$  = triangle leg length

Equation (66) is the same as equation (14) but with  $E$  and  $t$  replaced by  $E^*$  and  $t^*$  which are the equivalent Young's Modulus and skin thickness respectively. The equivalent parameters  $E^*$  and  $t^*$  account for the stiffening effect of the grid, but because they are isotropic, equation (14) is still valid. Equations (67) and (68) give  $E^*$  and  $t^*$  where  $\frac{(1+\alpha)^2}{\beta}$  represents stiffness and  $\frac{\beta}{1+\alpha}$  represents thickness effect of the stiffeners on the skin.

$$p_{crit} = 0.8 \cdot \frac{E^*}{\sqrt{1-\nu^2}} \cdot \left(\frac{t^*}{r_s}\right)^2 \quad (66)$$

$$E^* = E \cdot \frac{(1+\alpha)^2}{\beta} \quad (67)$$

$$t^* = t_{skin_s} \cdot \frac{\beta}{1+\alpha} \quad (68)$$

Where:

$E^*$  = equivalent monocoque stiffness

$t^*$  = equivalent monocoque thickness

The non-dimensional values  $B$  and  $\alpha$  are given by equation (69) and equation (70). They are geometric properties of the isogrid used in equations (67) and (68). They were derived based on transformed geometry with the derivation in [36, p. 20.0.019].

$$\beta = \sqrt{3 \cdot \alpha \cdot \left(1 + \frac{d}{t_{skin_s}}\right)^2 + (1+\alpha) \cdot \left(1 + \alpha \cdot \left(\frac{d}{t_{skin_s}}\right)^2\right)} \quad (69)$$

$$\alpha = \frac{b \cdot d}{t_{skin_s} \cdot h} \quad (70)$$

Equations (66)- (70) can be used to determine the complete sphere buckling mode. However there are other buckling modes that must be examined. These are rib and skin buckling and are determined by equations (71) and (72) respectively [36]. Equation (71) is the equation for buckling of a plate that is clamped on three sides and free on the

fourth [36, p. 4.1.003]. This is an appropriate model because the stiffener is optimal at  $a/d < 5$  which gives it the dimensionality of a plate. If  $a/d > 5$  beam theory would be more appropriate. Equation (72) is the equation for buckling of an edge loaded, clamped, triangular plate [36, p. 4.1.004].

$$\sigma_{crb} = 0.456 \cdot \frac{\pi^2 \cdot E}{(1 - \nu^2)} \cdot \left(\frac{b}{d}\right)^2 \quad (71)$$

$$\sigma_{csb} = \frac{5}{12} \cdot \frac{\pi^2 \cdot E}{(1 - \nu^2)} \cdot \left(\frac{t_{skin_s}}{a}\right)^2 \quad (72)$$

Where:

$\sigma_{crb}$  = rib buckling critical stress

$\sigma_{csb}$  = skin buckling critical stress

All values of  $t$ ,  $d$ ,  $b$ , and  $h$  that satisfy equations (66), (71) and (72) are part of the feasible design space for the grid stiffened sphere. By simultaneously satisfying these equations, with the assumption that the optimal point would occur when all constraints are active, a system of three equations and four unknowns was formed. This allowed a simple graphical optimization method in which the lowest W/B was chosen by varying one variable and solving for the remaining three variables. In this case  $t_{skin_s}$  was chosen as the free variable, and  $d$ ,  $b$ , and  $h$  were found by satisfying equations (66), (71), and (72).

Figure 25 is a plot of W/B vs  $t_{skin_s}$  where W/B is a function of smeared skin thickness ( $\bar{t}$ ),  $r_s$ , and atmospheric properties as shown in equation (73). Equation (73) is the ratio of sphere weight to buoyant force. Sphere weight was based on  $a_s$ ,  $\rho_{skin}$ , and  $\bar{t}$ .

$\bar{t}$  was calculated by smearing the stiffeners and adding them to  $t_{skin_s}$  as shown in equation (76). Smearing was accomplished geometrically by taking stiffener length ( $a$ ) times stiffener cross-sectional area ( $b \cdot d$ ), assuming half of each stiffener was applied to each triangle, assuming three stiffeners per triangle, and dividing by triangle area which was  $\frac{1}{2} \cdot a \cdot h$ . This gave the smeared thickness of  $3 \cdot b \cdot \frac{d}{h}$  for each stiffener.

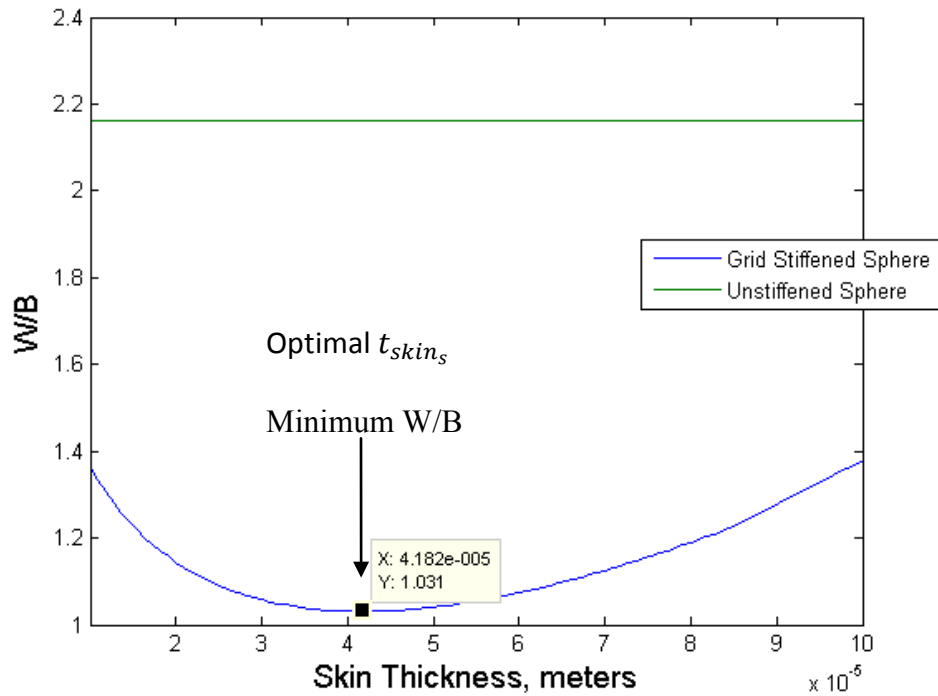
$$\frac{W}{B} = \frac{\rho_{skin} \cdot a_s \cdot \bar{t}}{\rho_{air} \cdot v_s} \quad (73)$$

$$\bar{t} = t_{skin_s} + 3 \cdot b \cdot \frac{d}{h} \quad (74)$$

Where:

$\bar{t}$  = smeared skin thickness

Figure 25: UHM Carbon Epoxy Isogrid Optimization



The optimal point in Figure 25 was the point of minimum W/B. This W/B, being a function of  $t_{skin_s}$ , enabled selection of the optimal variables  $t_{skin_s}$ , b, d, and h. This method, however, did not necessarily result in the true optimal geometry. It was recommended by the isogrid handbook, which was written in 1973 before more robust optimization techniques were made possible by modern computers. An alternate optimization technique was performed using a non-linear programming optimization routine in Matlab. The problem was formulated with equation (73) as the cost function to minimize, equations (66), (71), and (72) as constraints to be satisfied, and  $t_{skin_s}$ , b, d, and h as variables. The optimization program, called fmincon, conducted a search in order to minimize the cost function while satisfying the constraints by systematically changing the

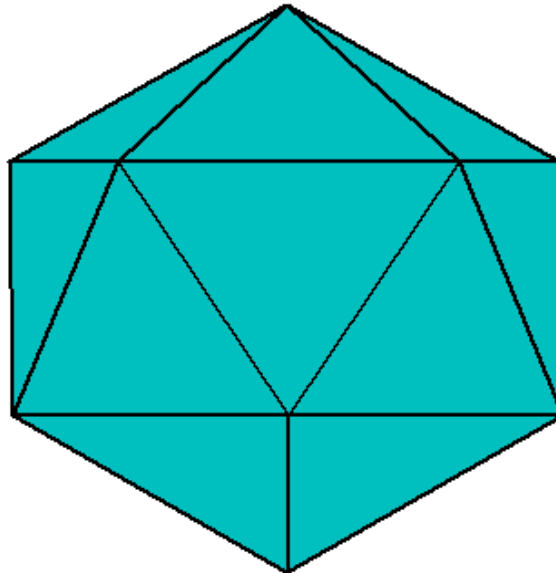
variables. More details on this optimization technique are available in 3.4.2 Optimization, and the code is available in Appendix A.13-15.

### 3.4 Geodesic Sphere

The geodesic sphere investigated consisted of a frame made of UHM carbon fiber tubes with a reinforced Mylar membrane stretched over it similar to a camping tent.

Figure 26 shows an icosahedron where the black lines represent the UHM carbon frame, and the shaded triangular faces represent the Vectran reinforced Mylar membrane.

**Figure 26: Geodesic Sphere Representation**



The material used to reinforce the Mylar membrane would need to have low density, high strength, high toughness and high stiffness. Two materials currently available for stiffening the skin are Zylon and Vectran as shown in Table 6. If graphene could be made in usable sizes and attached to the structure, it would far exceed the

performance of currently available materials. The optimization was performed for the frame alone. The skin was evaluated separately after the frame.

Table 6: Material Properties-Skin					
Material from Matweb	E, Pa	$\rho_s, \frac{kg}{m^3}$	$\sigma_y, GPa$	Geodesic Skin W/B	Comments
Graphene	$250 \cdot 10^9$	100	130	0.02	Only Available in small sheets
Zylon	$303 \cdot 10^9$	1560	5.8	2.5	Fiber
Vectran	$75 \cdot 10^9$	1400	3.2	3.6	Fiber

The W/B of the UHM carbon tube frame was computed according to equation (75). The variables  $t_{cb}$ ,  $r_{cb}$ ,  $\bar{l}_{cb}$ , and  $\rho_{cb}$  denote the thickness, radius, average length, and material density respectively of the cylindrical beams. The numerator of equation (75) is the mass of the frame. It was derived by taking the cross sectional area of each beam, multiplying it by its length and density to get the mass of each beam, then multiplying the mass of each beam by the number of beams in the structure,  $n_e$ . Equation (32) was used to calculate  $n_e$ . The buoyant mass, or mass of the air displaced by the geodesic sphere, is denoted by  $m_b$ , which is a function of the density of air and volume of the geodesic sphere as shown in equation (80). An optimization program called fmincon was run in Matlab to find the minimum W/B of the UHM carbon tube frame. The optimization problem was formulated as follows [52]:

Minimize:

$$F(t_{cb}, r_{cb}, f) = \frac{\rho_{cb} \cdot 2 \cdot \pi \cdot r_{cb} \cdot t_{cb} \cdot \bar{l}_{cb} \cdot n_e}{m_b} \quad (75)$$

Subject to:

$$g_1 = \frac{P_e}{2 \cdot \pi \cdot r_{cb} \cdot t_{cb}} - \sigma_{cbcy} \leq 0 \quad (76)$$

$$g_2 = P_e - \frac{4 \cdot \pi^2 \cdot E_{cb} \cdot I_{cb}}{l_{cb}^2} \leq 0 \quad (77)$$

$$g_3 = \frac{t_{cb}}{2} - r_{cb} \leq 0 \quad (78)$$

$$g_4 = r_{cb} + \frac{t_{cb}}{2} - \frac{\sqrt{3} \cdot r_s}{4 \cdot f} \leq 0 \quad (79)$$

Where:

$$m_b = V_{gs} \cdot \rho_{air} \quad (80)$$

And:

$g_1$  = requirement that the compressive yield strength of the material not be exceeded by the stress in any given beam.

$g_2$  = Euler's buckling equation for a cylindrical column under axial load with clamped ends, [4]

$g_3$  = requirement that the thickness not exceed twice the radius, the thickness of the beam cannot extend past the center point of the beam, at which point the cylinder is no longer a hollow pipe but is now a solid bar.

$g_4$  = requirement that the radius of the beam not extend past the center of a given minor triangle. This is a conservative estimate that will result in at least a small space between beams at the center of each triangular face.

$I_{cb}$  = the area moment of inertia of the cylindrical beam

$P_e$  = Euler load on end of beam

$\sigma_{cbcy}$  = compressive yield stress of cylindrical beam

Assumptions:

Clamped beams, even pressure distribution on skin, loads on beam ends only as equivalent forces, skin does not add stiffness, safety factor of 1.5, standard atmosphere at sea level, failure in any member constitutes global failure, no added mass for connectors at ends of beams.

The constraint  $g_1$  was derived based on the requirement that the material compressive strength of the cylindrical beams, ( $\sigma_{cbcy}$ ), not be exceeded. This was determined using FEA to solve for the stress in each beam using `analyze_beam.m` in

Appendix A.5. After solving for the stress, the maximum stress out of all the members in the structure was found and compared to  $\sigma_{cb_{cy}}$ . As long as  $\sigma_{cb_{cy}}$  was of greater absolute value than the stress in every member,  $g_1$  was satisfied.

Note that all of the constraints were set to be less than or equal to zero. This was required by `fmincon`, the optimization function used in Matlab. If any inequality constraint was less than or equal to zero, it was satisfied. If a constraint was greater than zero it was violated and the solution was considered infeasible. In the case of  $g_1$ , if  $\sigma_{cb_{cy}}$  was less than the stress in the beam, then  $g_1$  would be positive and the material strength of the beam would be exceeded.

The constraint  $g_2$  was derived based on the buckling load of a cylindrical column with clamped ends. Clamped ends were assumed because all of the methods of attaching the ends of the beams to each other that were considered involved a fastening method that transmitted bending moments in addition to forces. If a ball and socket attachment were made for the structure, equation (77) would have to be replaced by the buckling equation for a cylindrical column with end load with a pinned boundary condition at each end, which is  $\frac{1}{4}$  the critical load of the clamped equation.

The constraint  $g_4$  was a geometric constraint created to keep the cylindrical beams' walls from intersecting each other at the center of a triangular face. It is based on the distance from the center of the triangle to its edge. Triangle height is given by equation (81) where  $a$  is the leg length of a minor triangle. The distance from the edge of a triangle to its center is  $\frac{1}{2} \cdot h$ , which must be greater than or equal to the radius plus

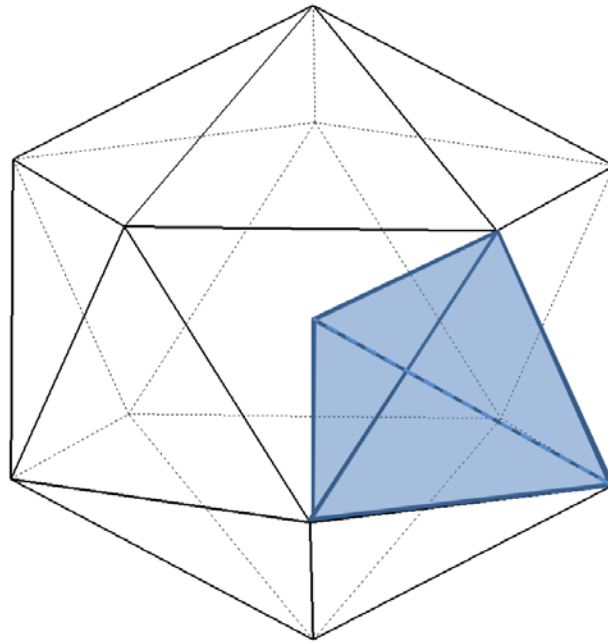
thickness of the cylindrical beams, which gives  $g_4$ . Note that  $a=1.05r/f$ , so that a more conservative solution was obtained by replacing  $a$  with  $r_s$  and dividing by  $f$ .

$$h = \frac{\sqrt{3}}{2} \cdot a \quad (81)$$

The area of the geodesic sphere,  $a_{gs}$ , was calculated by summing the area of each triangular face on the structure, and although not used in the optimization, enabled an estimate of skin weight. The volume of the geodesic sphere,  $v_{gs}$ , was calculated by summing the volume of the triangular pyramids formed by the three vertices of each triangular face and the center point of the sphere as illustrated by the shaded region in Figure 1. Equation (82), [40], gives the volume of a pyramid, ( $v_p$ ), which is 1/3 of base area, ( $a_b$ ), times height perpendicular to base. In the case of a geodesic sphere, the height was measured from the center of the sphere to the centroid of any triangle on the surface and the base was the area of the triangular face. By summing the volume of the pyramids formed by every base, the total sphere volume was found.

$$v_p = \frac{1}{3} \cdot a_b \cdot h_p \quad (82)$$

**Figure 27: Geodesic Sphere – Volume Calculation**



The Euler Load  $P_e$  was calculated using FEA with beam elements. Forces on the ends of the beams were calculated using  $p_{\text{air}}$  times the area of each triangular face, distributed over the three vertices of the triangle in the direction normal to the face. This method resulted in zero moment on each beam. This was because forces were applied at the nodes and not on the sides of the beams. It was also because multiple beams resisted the equivalent load at each node, so that axial forces in each beam resisted the equivalent load no matter which way it was oriented. The boundary condition consisted of restricting 6 degrees of freedom on the node at the bottom of the sphere. No mass was added for connectors at the ends of the beams based on the assumption that the sphere could be constructed of continuously wound filaments about a mandrill where vertices would be a flat, continuous transition between pultruded rods. If connectors are required in the future

their mass will have to be added to the cost function and would be the weight of a connector multiplied by the number of vertices,  $n_v$ .

Table 7 displays the material properties used to calculate the optimal sphere geometry. Additional constants used include  $r_s = 0.33$  m,  $p_a = 101325$  Pa, and  $\rho_a = 1.225 \frac{kg}{m^3}$ . The assumption was made that UHM carbon had a  $V_f = 0.6$  of the composite tubes and the composite stiffness in the longitudinal direction was calculated using equation (24). Poisson's ratio was assumed to be 0.3.

**Table 7: Material Properties-Frame**

Material	E, Pa	$\rho, \frac{kg}{m^3}$	$\nu$	$\sigma_{cbcy}, Pa$
Dupont E-130-X Pitch Based UHM Carbon Fiber	$895 \cdot 10^9$	2130	Unpublished	Unpublished
UHM Unidirectional Carbon Epoxy tubes	$538 \cdot 10^9$	1522	0.30	$1 \cdot 10^9$

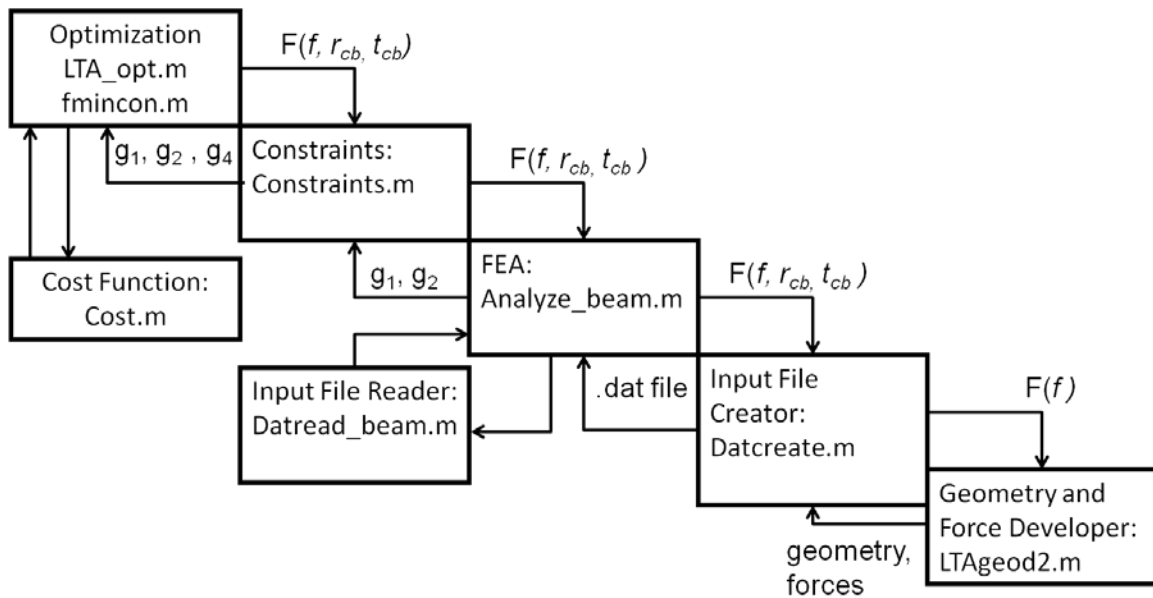
Figure 28 shows a workflow diagram of the optimization process. All programs were run within Matlab to include the geometry, force calculations, FEA, and optimization routine. Optimization was conducted graphically as well as numerically. The graphical method was primarily used to validate the numerical results, as well as understand the design space. The numerical method was conducted in LTA\_opt.m, Appendix A.1, which used the Matlab optimization routine fmincon. fmincon is a constrained, nonlinear program that worked by systematically changing the variables  $f$ ,  $r_{cb}$ , and  $t_{cb}$  in order to minimize the cost, which was evaluated using Cost.m, Appendix

A.2, where cost was defined by equation (75). Cost.m called the Matlab program Sphere\_param.m, Appendix A.3, which used the variables from fmincon to calculate sphere parameters that were then used by Cost.m to calculate the W/B of the frame. After determining that it had moved in a direction to minimize the cost, fmincon checked the feasibility of the new variables. fmincon can automatically check the feasibility of linear constraints, which it did for  $g_3$ , but it must call a function to evaluate nonlinear constraints. It did this by calling Constraints.m, Appendix A.4. Constraints.m was used to calculate  $g_1$ ,  $g_2$ , and  $g_4$ .  $g_4$  was simply a nonlinear function of the input variables, and so was quickly evaluated by Constraints.m, but  $g_1$  and  $g_2$  required the stress in each member to be evaluated, which required geometry and FEA based on the input variables from fmincon. Constraints.m called Analyze\_beam.m [53], Appendix A.5, in order to retrieve the stress in the members. Analyze\_beam.m determined the stresses in the members by retrieving a finite element input card, sending it to a finite element reader and evaluating the resulting finite element model using FEA. Analyze\_beam.m retrieved the input card by calling the Matlab program Datcreate.m [54], Appendix A.6, which created a .dat input file. Datcreate.m created the input file using a node matrix, element matrix, force matrix, and boundary conditions provided by the Matlab program LTAgeod2.m, Appendix A.7. LTAgeod2.m calculated the node matrix, element matrix, and force matrix based on  $f$  using geodesic geometry. This program was also used to generate the geodesic figures shown in this document. It relied on the geometry of an icosahedron which was discussed in detail in chapter 2.5 Geodesic Sphere, as well as geodesic geometry discussed later in this chapter. After Datcreate.m retrieved the geometric data from LTAgeod2.m, it compiled the data into a .dat input file for use by

Analyze\_beam.m. After receiving the .dat input file, Analyze\_beam.m called the .dat file reader, Datread\_beam.m [55], Appendix A.8, which processed the .dat file.

Analyze\_beam.m then created a global stiffness matrix, force vector, displacement vector, and solved for displacements. This data was then used to determine stress in each member of the frame, which was used by Constraints.m to calculate  $g_1$  and  $g_2$ . Finally, fmincon evaluated the constraints to ensure all were satisfied. It also checked to see if the change in cost was low enough to indicate an optimal point had been found. If optimization was not achieved fmincon would change the input variables using the interior –point search method and the whole process was repeated.

**Figure 28: Workflow Diagram**

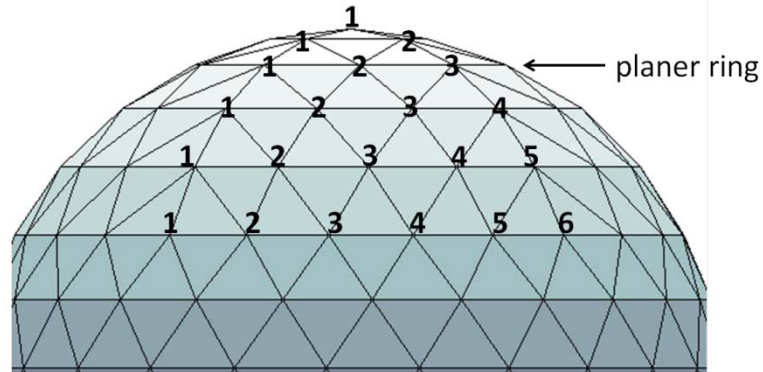


### 3.4.1 Geometry

The geodesic sphere geometry was calculated using the LTAged2.m program, Appendix A.7. This program generated a geodesic sphere by subdividing an icosahedron along its major triangles by the integer  $f$  according to the geometry described in [37].

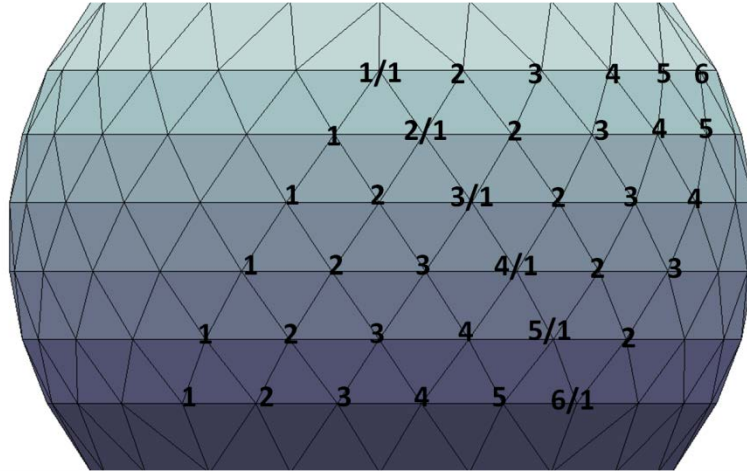
Geodesic sphere geometry was calculated by systematically working from top down on the icosahedron. Each of the major triangles were divided into three groups; the top pentagon cap of five triangles that touch vertex 1 in Table 5, the center band of 10 triangles, and the bottom pentagon cap of five triangles touching vertex 12 in Table 5. The major triangles within these groups were subdivided by dividing each major triangle vertically  $f$  times per major triangle. Planer rings were then considered working from the top vertex down, where each ring consisted of every vertex on a plane of constant  $\phi$  (parallel to the xy cartesian plane) as shown in Figure 29. For the top pentagon cap each subsequent ring had one more vertex than the one before it for each major triangle. This pattern enabled automatic generation of vertex points for the top pentagon cap for any  $f$ . This pattern is shown in Figure 29, where each number represents the order of vertex generation for a given planer ring for a geodesic sphere of  $f=5$ . Each vertex on a plane had a constant  $\phi$ .  $\theta$  was determined by dividing  $2 \cdot \pi/5$  by the number of divisions per major triangle for a given planer ring. As shown in Figure 29, the number of divisions increased by one for each planer ring, with the bottom ring having  $f$  divisions. Note that the major triangle shown in Figure 29 is divided into 5 rows of triangles corresponding to  $f=5$ . Also note that there are six triangle edges emanating from each vertex, except for those vertices at the corners of major triangles, these have five triangle edges and these make pentagon caps.

**Figure 29: Geodesic Sphere Generation-Top Pentagon Cap**



The center band of 10 triangles, as shown in Figure 30, continued the pattern of  $\phi$  generation for each planer ring by dividing the triangles vertically  $f$  times, just as was done for the top pentagon cap.  $\theta$  was different, however, in that every planer ring had exactly the same number of divisions for the center band of 10 triangles. This occurred because the 10 triangles along the center band alternate between point up and point down. As one triangle gets wider, the adjacent triangles get narrower. If layed flat, the center band of triangles would make a parallelogram with sides of  $length = 5 \cdot a$  on top and bottom and  $length=a$  on the sides, where  $a$  is the length of a major triangle leg. Equally dividing this parallelogram for each planer ring resulted in increments of  $\theta = (2 \cdot \pi)/(5 \cdot f)$ . This pattern again allowed for automatic generation of vertices based on  $f$ .

**Figure 30: Geodesic Sphere Generation-Center Band of 10 Major Triangles**



The bottom pentagon cap was simply the reverse of the top pentagon cap, which again allowed for automatic vertex generation. Similar, although somewhat more complicated approaches, were used to determine beam connections between vertices.

Forces were calculated by multiplying the area of each triangle by the pressure of atmosphere and a 1.5 safety factor. The resulting force was divided by 3 and applied at the vertices of each triangle. For the icosahedron, which consists entirely of equilateral triangles, this resulted in completely symmetric loading. For geodesic spheres of  $f > 1$  this resulted in uneven loading due to slightly different triangle areas. This caused some beams to have higher stress than others.

### ***3.4.2 Optimization***

The `fmincon` optimization routine in Matlab is a robust solver that finds the minimum value of a constrained, nonlinear, multivariable function. For an in depth explanation of the theory behind `fmincon` see the Matlab help file, which includes references that explain the theory [56]. In this case, equation (75) was minimized subject

to the constraints g1, g2, g3, and g4. The constraints g1 and g2 required outputs from the FEA program. The FEA program was limited in function to 6 degree of freedom beam elements, but it was computationally efficient and operated within Matlab, which significantly increased the speed of each iteration above what would have been possible using commercial FEA codes. The results of the FEA program were checked against NASTRAN, which by design uses the same input files as the FEA program used for this study. Stress results between NASTRAN and Analyze\_beam.m were the same when given the same .dat file from Datcreate.m.

A genetic algorithm minimization routine was also used in Matlab, called ga.m, to make sure fmincon was not being caught in local minimums. The genetic algorithm operates by testing cost and feasibility at multiple points in the design space over successive generations of design point populations. The first generation is often random, but subsequent generations are based on the best design points, termed individuals, from the previous generation. After testing these points, and assigning a fitness value to them, the genetic algorithm selects the most fit individuals, and reproduces them. The subsequent generation is formed by a random group of individuals that are based on the most fit individuals from the previous generation, similar to the theory of natural selection. This continues until the genetic algorithm converges sufficiently or reaches the specified number of generations. This method was highly inefficient because it required multiple iterations of the optimization process shown in Figure 28 for each generation, and it required multiple generations. The purpose of using the genetic algorithm was that it was less susceptible to getting stuck in a local minimum due to use of the wrong start point. Unlike fmincon, which requires an initial value for each variable, the genetic

algorithm only required upper and lower bounds on variables. The optimization results of `ga.m` were nearly identical to `fmincon`. `fmincon` was much faster, and more consistent however. The consistency of `fmincon` can be explained by its search method, which uses first and second derivative information. The genetic algorithm used a more random approach, in which no two searches tested the exact same populations of points, so that the optimal individual was always a little different. This imprecise nature of genetic algorithms was acceptable as long as the number of generations, and number of individuals per generation were sufficient. The tolerances on fitness value change over subsequent generations could be adjusted so that the genetic algorithm would keep searching until it began finding solutions within the specified error. This resulted in satisfactory results within tolerance, but the solution was still slightly different every time the program was run.

Finally, a graphical method of optimization was performed where the cost function and constraint functions were plotted for various cylinder radii and thicknesses while holding  $f$  constant. This provided a good sanity check for the answers `fmincon` produced as well as a better understanding of the design space. An example of the design space formed using the graphical method is shown in Figure 43. The cost was a function of three variables;  $f$ ,  $r_{cb}$ , and  $t_{cb}$  which would require a four dimensional plot to optimize graphically. Four dimensions is difficult if not impossible to plot or even comprehend. A plot of cost as a function of two variables, however, would only require three dimensions. Due to the long times required to generate geometry and evaluate stresses using FEA for high  $f$ ,  $f$  of only 1 through 10 were evaluated. It was hoped that by evaluating ten geometric frequencies a pattern would emerge, either high  $f$  would produce a lower W/B

or a higher W/B. Because the variable  $f$  consisted of integers, it was possible to produce ten three dimensional plots of the design space, each plot having a constant  $f$ , with cost as a function of  $r_{cb}$  and  $t_{cb}$  only. These plots allowed visual understanding of the design space and provided validation of fmincon and genetic algorithm results. These plots can be seen in Figure 43 and Figure 41 and are explained in chapter 4.

### **3.5 Summary**

The methods used in this investigation included buoyancy, weight, aerodynamic, and power requirements for the rotating cylinder vehicle, isogrid calculations for the isogrid stiffened structure, and geometry, FEA and optimization for the geodesic structure.

## **IV. Analysis and Results**

### **4.1 Chapter Overview**

This chapter gives the results of each study described in the methodology section. Also introduced are results to minor investigations which were necessary throughout the course of this investigation to focus the research. These include the identification of important material properties and choosing an altitude for evaluating vacuum LTA vehicles. The W/Bs obtained for the grid stiffened and geodesic spheres are listed and were evaluated for their impact on potential missions. Plots of von Karman efficiency were used to give a visual representation of these results.

## 4.2 Minor Investigations

The main focus of this investigation was development of a structure that could achieve positive buoyancy using a vacuum. Whenever an idea for a structure was evaluated it became necessary to determine the ideal material for that structure in order to find the lowest W/B. Reduction of W/B required improved geometric stiffening or improved material properties. The effect of increasing isotropic stiffness or decreasing density while keeping all other material properties constant is displayed in Figure 31. The dominant material property is  $E/\rho^2$ , therefore reducing density has a greater effect than increasing stiffness. After an extensive material search it became apparent that most materials with low densities and high stiffness also have low compressive strength, so that compressive strength becomes the dominant material property. These materials are generally foams or micro-lattice structures. Carbon epoxy composites appear to be the most promising materials available for this problem due to their combination of high specific stiffness and high compressive strength. There may be unpublished materials with higher specific stiffness than evaluated in this study. The question was asked, what happens if there are better materials, and what would the effect of improved material properties be on W/B? Figure 31 shows the linear relationship between density and W/B. The assumptions made for creating this graph were an isotropic stiffness of  $E=895$  GPa,  $\nu = 0.3$ ,  $\sigma_{c_y} = 1.7$  GPa and using an isogrid stiffened sphere. No material on the market has these characteristics, but they serve to show the effect of changing material properties on achievable W/B in an isogrid stiffened sphere. These effects are specific to the isogrid geometry, however similar affects will be seen on the frame of the geodesic sphere.

Figure 31: Effect of Density on W/B

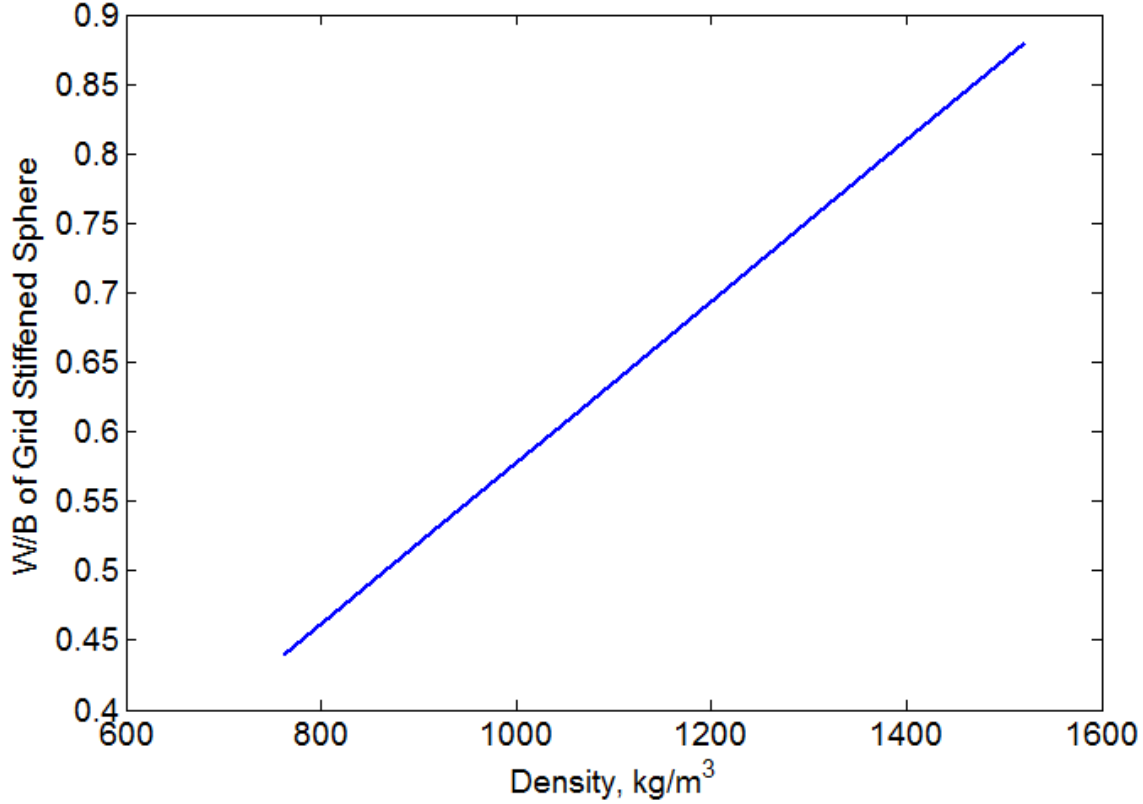
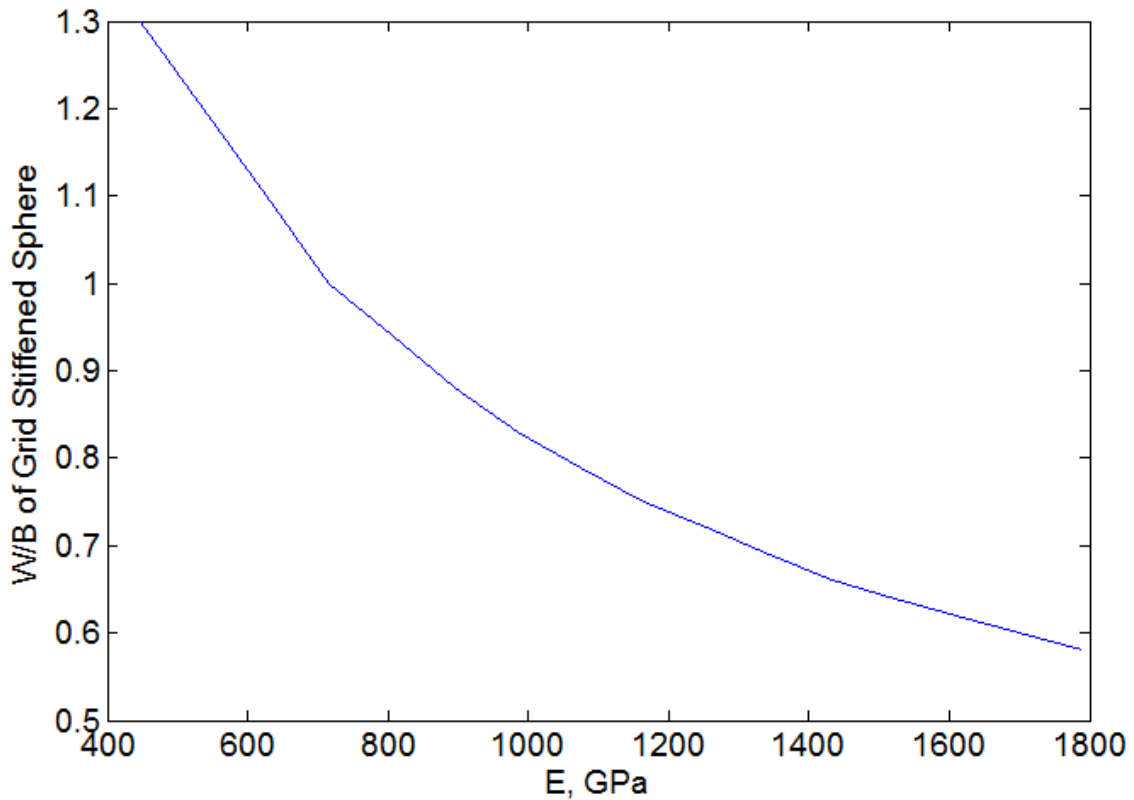


Figure 32 shows the effect of increasing stiffness. Although increasing stiffness decreases W/B, the W/B is less sensitive to stiffness than it is to density. This makes sense when looking at equation (23), which shows that W/B is a function of  $E/\rho^2$ . The assumptions made for creating this graph were  $\rho = 1522 \text{ kg/m}^3$ ,  $\nu = 0.3$ , and using an isogrid stiffened sphere. Figure 31 and Figure 32 were produced using LTAsphere.m, Appendix A.10

**Figure 32: Effect of Young's Modulus of Elasticity on W/B**



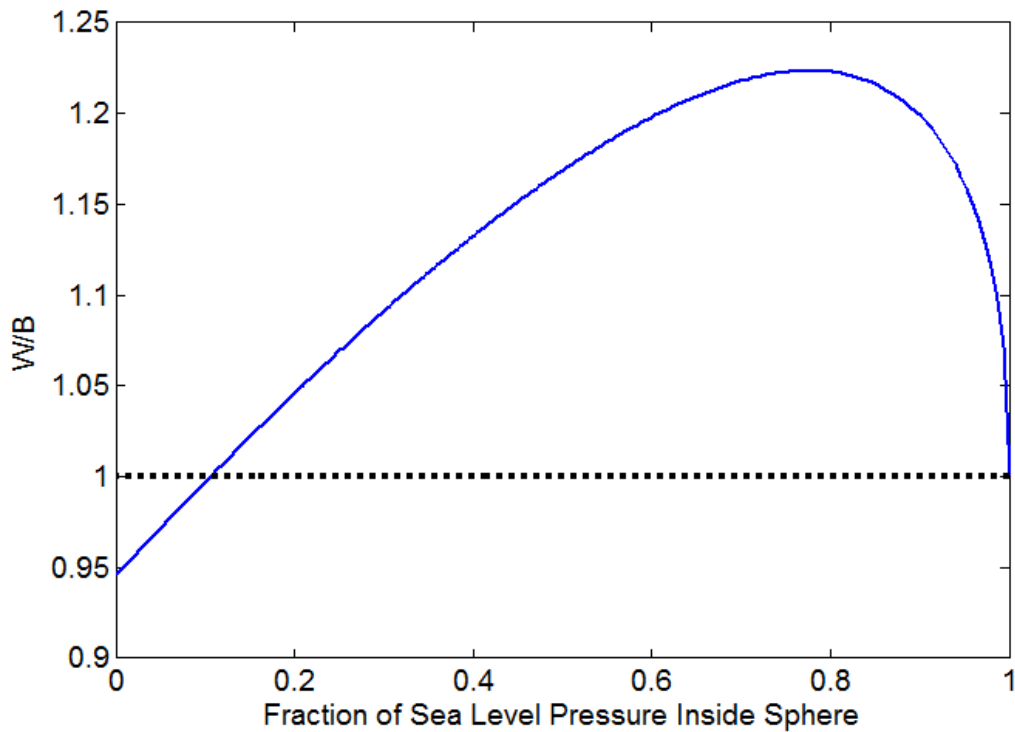
A study was conducted to determine the optimal internal pressure for air in a partial vacuum LTA structure. The question that drove this study was whether there was an optimal internal air pressure at which the required structure weight due to external pressure compared most favorably with a decrease of buoyant force due to internal air pressure. Figure 33 shows a plot of W/B at sea level for a blade stiffened sphere assuming it is designed for a specific internal pressure corresponding to the value on the abscissa. This means that as internal pressure increases on the x axis, the structure is designed to withstand less external pressure loading. As design internal pressure increases, even with the reduced stiffness requirement, the increase in weight due to the air molecules inside the structure, as well as the decrease in buoyant force results in a

decrease in achievable W/B. These calculations were performed in the Matlab program titled LTApvalt.m , Appendix A.11. The governing equations in LTApvalt are equations (66) through (70) where  $\bar{t}$ ,  $t^*$ , and  $E^*$  were calculated in the Matlab program titled LTAsphere.m for a blade stiffened sphere.

Figure 33 was generated assuming an isogrid structure with an isotropic material with  $E=450$  GPa,  $\rho = 1522$  kg/m<sup>3</sup>,  $\nu = 0.3$ , sea level standard day conditions.

Although a material with these properties does not necessarily exist, Figure 33 does show the appropriate relationship between internal pressure and W/B. Note that the curve in Figure 33 appears to show a decrease in W/B at an internal pressure of about 80% of sea level pressure. There is indeed a decrease in W/B, but this portion of the curve will always decrease to a minimum W/B=1 at an internal pressure of sea level. This is because the required structural stiffness approaches zero as internal pressure approaches sea level pressure, but the weight of air inside the structure approaches the weight of air displaced, so that as the structure weight decreases, the internal weight of air increases. The farthest right point on the graph is where W/B=1 because the structure no longer exists, and the air is neutrally buoyant within itself. Therefore the only truly informative part of the curve in Figure 33 is the portion of the graph to the left of the W/B maximum point. This portion of the curve shows that as internal pressure decreases, W/B also decreases, so that the point of minimum W/B will be achieved when there is a perfect vacuum inside the structure.

**Figure 33: Effect of Increasing Internal Pressure**



Does an increase in volume result in a decrease in  $W/B$ ? This question is often accompanied with a reference to the squared cube law. The squared cube law states that as the radius of a sphere increases, its surface area grows at a rate of radius squared, while its volume grows at a rate of radius cubed. These relationships can be seen by comparing equations (21) and (41), which are the volume of a sphere and surface area of a sphere respectively. This is also reflected by von Karman efficiency, defined by equation (2), which favors an increase in volume for an airship. This is shown graphically in Figure 9 where the airship with the larger radius (and thus volume) has a better von Karman efficiency (its curve is down and to the right). This is because the lifting capacity of the airship grows faster with an increase in volume than the drag of the airship.

If the square cubed law makes the conventional airship favor larger sizes, does it do the same to the vacuum structure? As far as von Karman efficiency is concerned, the vacuum airship would perform better at higher volumes. But as far as W/B is concerned, the squared cube law does not apply. This is because the vacuum LTA vehicle must be able to resist compressive loads without buckling or exceeding material strength. This can only be accomplished by an increase in thickness whenever there is an increase in volume for a given design. The increase in thickness, accompanied by the increased surface area, increases the volume of the skin material at the same rate as the volume of the overall structure is increased, so that the mass of the structure maintains the same ratio with the mass of the air displaced. In other words, the W/B is constant for a given design regardless of volume. There are several advantages to making a vacuum LTA vehicle larger, however. One is that a larger structure has thicker walls. The designs in this study require very thin walls, some that might be thinner than current manufacturing capabilities allow. By making a larger structure it would be possible to use larger thicknesses that can be accommodated by current technology. The second advantage is increased von Karman efficiency, as previously discussed. The property of constant W/B regardless of sphere size means that the dimensions of the results of this study can be scaled, but the optimal W/B will be the same for any sized sphere.

### **4.3 Rotating Cylinder Vacuum LTA Vehicle**

The RCVLTA V was evaluated with assumptions listed in Table 8. The results gave energy requirements so high for each radius and length calculation that the weight of the engine and fuel was prohibitive for flight. This was because the entire lift capacity

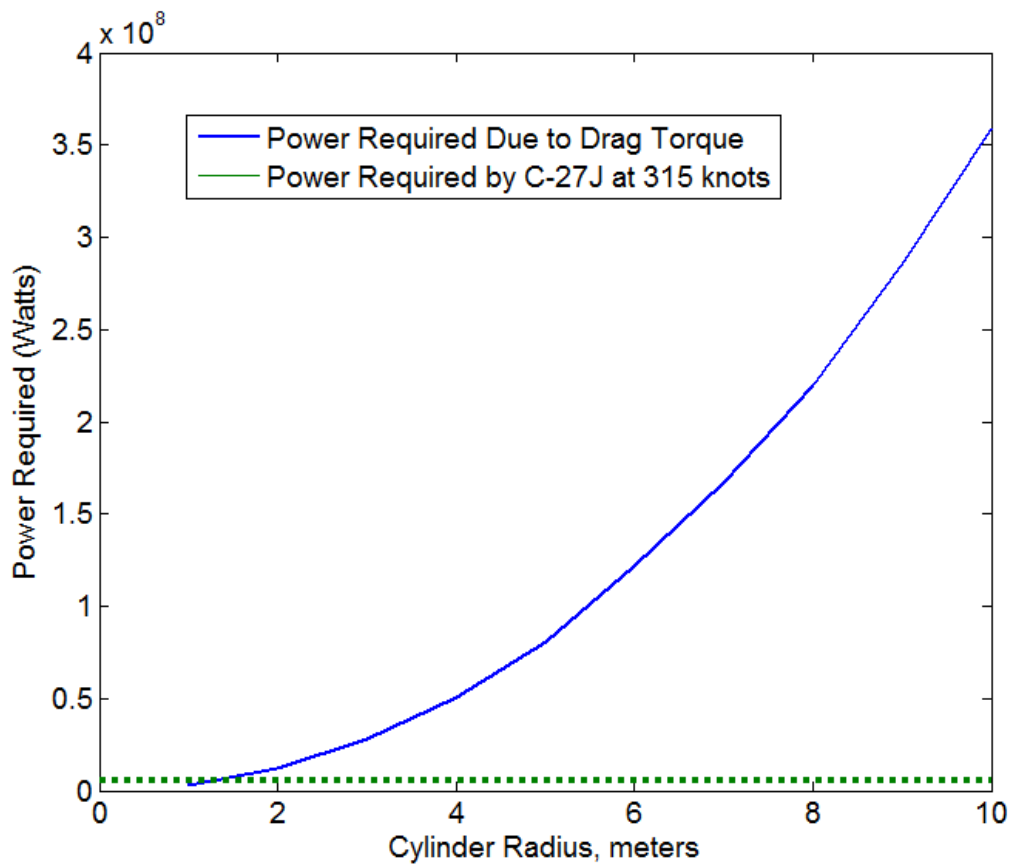
of the vehicle was less than the weight of the engine and fuel required to rotate the cylinders according to equations (61) and (62). This held true for rotating cylinder vehicles at all altitudes with cylinder radii of 10 meters or less and a length/diameter <500 even if the weight of fuel was neglected. The power requirements of the RCVLTAV are plotted with the power requirements of the C-27J in Figure 34 to give an idea of how much power the RCVLTAV would require. An altitude of 19.8km (65k ft) MSL was assumed, which was the most efficient altitude for the RCVLTAV. These high power requirements were due to high rotational velocities, which were required by the assumption that the external pressure due to atmosphere was fully resisted by the inertia of rotating cylinder walls. At sea level the cylinder surface velocity,  $u_r \cong 730$  m/s, which is greater than the speed of sound, while at 19.8km MSL it was about 195 m/s. Due to the fact that  $C_{Dc}$  does not change with Mach number [47], equation (55) remains valid even for high velocities. Whether or not counter rotating cylinders would form virtual elliptical bodies at high Reynolds numbers is uncertain. The RCVLTAV at 19.8km would have Reynolds numbers ranging from  $1 \cdot 10^7$  to  $1.2 \cdot 10^8$  for radii of 1 to 10 meters. The assumption was made that the rotating cylinders would act in the same manner as rotating cylinders with low Reynolds numbers. If the results of this study was favorable to the performance of the RCVLTAV this assumption would need to be verified.

**Table 8: Rotating Cylinder Vehicle Assumptions**

$a_g$	= 10.5 m <sup>2</sup> based on cylindrical cross section of C-27J cabin[6]
$a_p$	= 12.6 m <sup>2</sup> based on historical airship rotor sizes [9]
$C_{d_g}$	= 0.012 based on wind tunnel testing[13]
$k_{ee}$	= 0.33 based on turbine engine efficiency [13]

$k_{pe} = 0.55$  assuming stern mounted propellers [24]  
 $m_b = 26$  kg from vendor website [50]  
 $m_g = 2114$  kg based on  $11 \frac{\text{kg}}{\text{m}^3}$  and volume of C-27J cabin [13],[6]  
 range= 1852 km based on C-27J range [6]  
 $\zeta = 43.02 \cdot 10^6 \frac{\text{J}}{\text{kg}}$  BP Jet A [57]  
 $\Omega = 1.5$  assuming less than 1 cylinder diameter spacing [45]  
 sea level to 19.8km (65k ft) MSL standard day atmospheric conditions

**Figure 34: Power Required by RCVLTA at 75% Drag Torque at 19.8km MSL**



A reduction in drag torque of about 25% on counter rotating cylinders due to a virtual elliptical body has been shown [45]. There is an apparent trend that as the gap between cylinders is decreased, the drag torque also decreases. The question was raised, how much would the drag torque have to decrease in order for the RCVLTA to become

feasible? The energy requirements of a RCVLTAV with a 99% decrease in drag torque, at the optimal operating altitude of 19.8km MSL, resulted in a vehicle that could fly. The energy comparison between this vehicle at various cylinder radii and the C-27J is plotted in Figure 35. This shows that with a radius of less than nine meters, the RCVLTAV would use less energy than the C-27J. In order to better understand the transportation efficiency of the RCVLTAV a plot of von Karman Efficiency is shown for radii of one through ten meters in Figure 36.

**Figure 35: Power Required by RCVLTAV at 1% Drag Torque at 19.8km MSL**

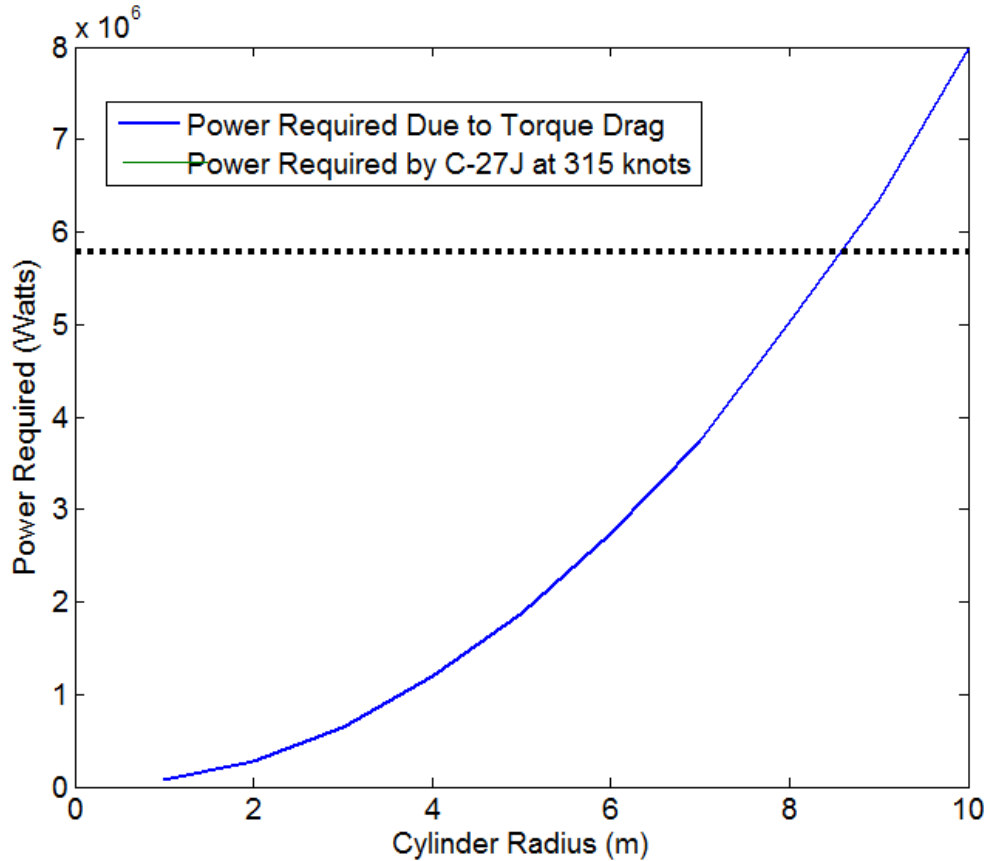
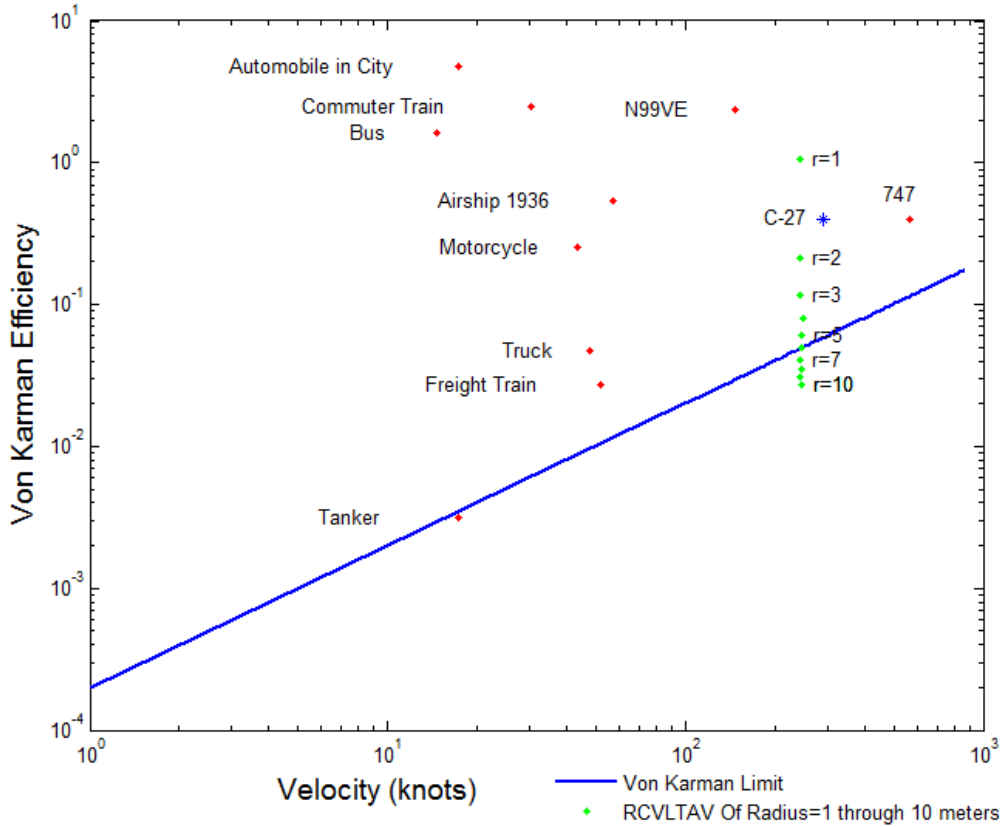


Figure 36: RCVLTAV at 1% Drag Torque at 19.8km MSL



The von Karman efficiency of the RCVLTAVs in Figure 36 are excellent, but it is unlikely that a drag torque reduction of 99% will occur for closely spaced, or even touching cylinders. Even if a drag torque reduction of 99% were possible, the vehicle still could not operate at sea level. At sea level, the energy requirements were higher due to increased drag, so that an engine that could provide the required power would be too heavy. Therefore the vehicle would have to be assisted in its climb to altitude by another vehicle capable of carrying itself and the vehicle in question. The geometry of this structure would be 1 to 10 meters in radius (or higher if desired),  $W/B=0.51$ , 305 to 3100 meters long, and have a mass of 5,865 to 990,000 kg (depending on radius). The

dimensions of this vehicle, the inability to fly at sea level atmospheric conditions, and the requirement for a 99% reduction in drag torque, all combine to make the RCVLTAV appear infeasible.

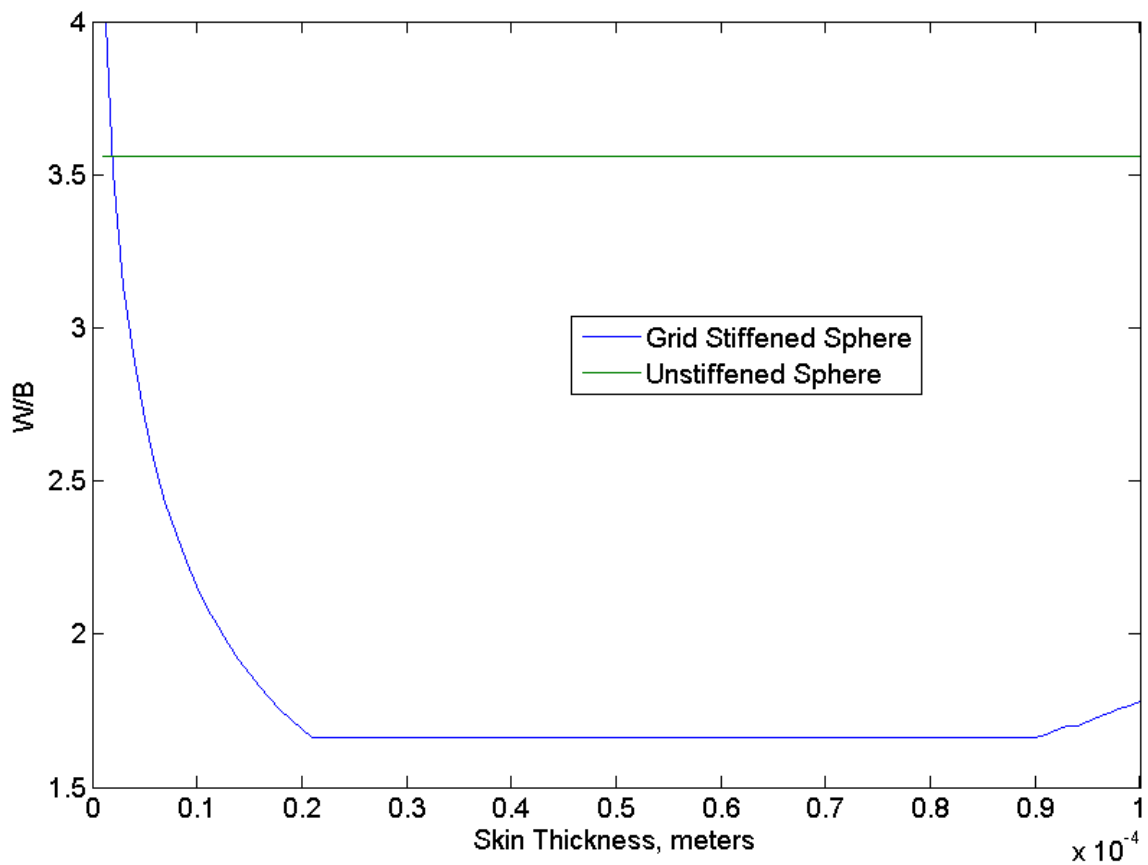
#### 4.4 Isogrid Stiffened Sphere

Using equations (66) - (72) the optimal isogrid dimensions were calculated for a 1/3 meter radius sphere made of the UHM carbon epoxy with properties shown in Table 4. The W/B of various structures were found to be independent of size so that any radius could have been chosen. A 1/3 meter radius was chosen to create a structure capable of fitting through a door. This had both research and mission purposes. For the purposes of research it would be more economical to construct a structure that uses less material. If a vacuum LTA structure could be designed, it would be advantageous to have it small enough to move in and out of labs, class rooms, vehicles etc. Also, one mission type identified as suitable for the vacuum LTA vehicle was as a small sensor platform for use in the urban environment.

An optimization was performed using equations (66), (71), and (72) and four unknowns ( $b$ ,  $d$ ,  $h$ , and  $t_{skin_s}$ ). The optimization was performed by assuming the optimum design occurred when each of the constraints were simultaneously satisfied. Because there was one more variable than equation, it was possible to solve the equations for multiple values of  $t_{skin_s}$ . The equivalent mass thickness,  $\bar{t}$ , was calculated using equation (74), which gave the thickness that would be obtained if the isogrid was smeared evenly over the skin.

Equations (20), (21), (73), and (74) were used to determine the W/B of the grid stiffened sphere at standard day sea level pressure with a safety factor of 1.5. By varying thickness and solving for the remaining three variables a different W/B was calculated for each thickness and plotted in Figure 37 for a sphere made of Beryllium. The thickness corresponding to the lowest W/B was chosen as the optimal structure. The W/B for the optimal structure came out to be 1.7. Unfortunately this isogrid structure would not achieve positive buoyancy.

**Figure 37: Beryllium Isogrid Optimization**



Equations (5) and (21) were then used to determine the W/B ratio of an unstiffened sphere of the same radius, material, and atmospheric conditions. This ratio came out to be 3.6. Therefore the isogrid structure reduced the W/B ratio of the unstiffened sphere by about 52%. Both values can be seen on Figure 37. This exercise demonstrates the difficulty of achieving positive buoyancy with a vacuum structure. It also demonstrates the importance of both material selection and geometry. Beryllium was selected because it had the highest  $E/\rho^2$  value of any isotropic material investigated. Note the flat portion of the curve at the bottom of Figure 37 where W/B is 1.7 for a range of thicknesses. The flat portion is caused by the material compressive strength constraint becoming active as opposed to the buckling constraint. When this occurs there is a minimum cross sectional area required in order to prevent material failure, so no matter what combination of variables are chosen, they must add up to a minimum  $\bar{t}$ . If the compressive yield strength of the beryllium could be augmented, a lower value for W/B could be achieved. Augmentation in this case could take the form of adding another material to the structure. For a composite material it could mean adding a different fiber or additive to the matrix. This demonstrates that although  $E/\rho^2$  is important, in this case the material compressive yield strength is the active constraint at the optimal point, so that an increase in material stiffness would have no effect on W/B. There are lightweight materials such as plastic foams that have better  $E/\rho^2$  values than UHM carbon fiber, but due to their low compressive yield strengths they are unsuitable for this problem. These materials fail when their compressive yield strength is exceeded.

An evaluation of the grid stiffened sphere was conducted using Dupont E-130-X carbon fiber in an Epoxy matrix. A unidirectional arrangement of fibers was assumed for

the stiffeners, and a quasi-isotropic laminate for the skin. If a  $[0/\pm 45/90]_s$  ply arrangement were used for the skin, the estimated isotropic stiffness would be approximately 202 GPa. The unidirectional fiber Modulus in the stiffeners was approximately 538 GPa. In order to use the isotropic assumptions of the isogrid handbook, a transformed thickness had to be computed for the stiffener. This was done using equation (83), which gives equivalent stiffener thickness by multiplying the actual thickness by the ratio of stiffener stiffness to skin stiffness. The transformed thickness  $b^*$  is then used in equation (70) to calculate  $\alpha$  in order to determine the equivalent thickness and stiffness  $E^*$  and  $t^*$ .

$$b^* = b \cdot \frac{E_{stif}}{E_{skin}} \quad (83)$$

Where:

$b$  = stiffener thickness

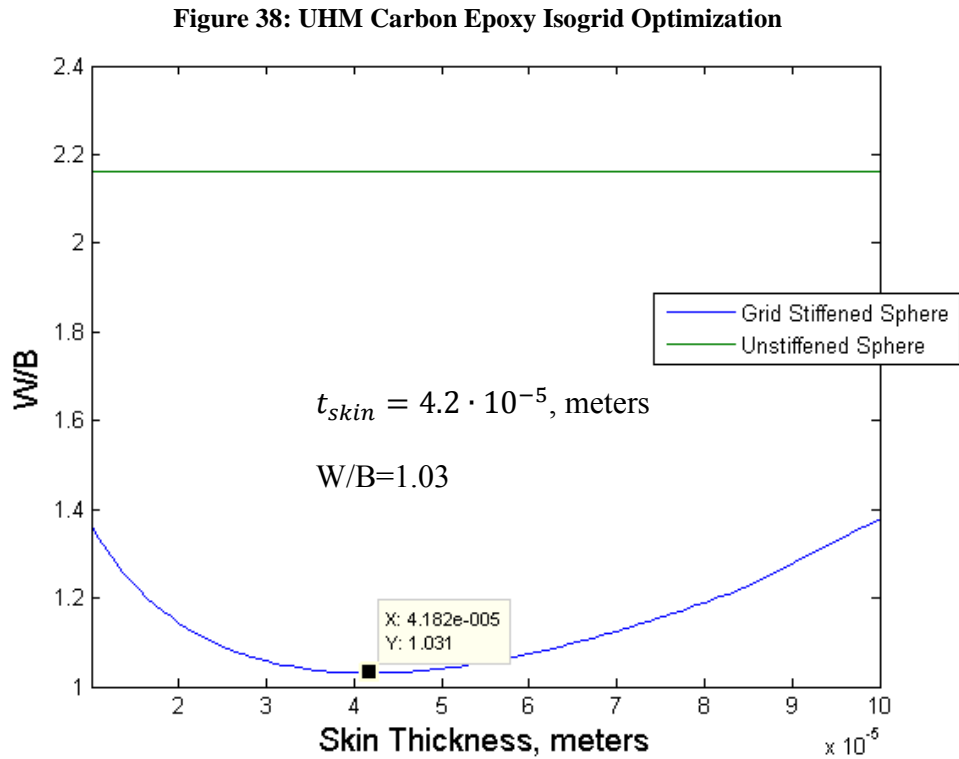
$b^*$  = transformed stiffener thickness

$E_{stif}$  = stiffener modulus of elasticity

$E_{skin}$  = skin modulus of elasticity

After transforming the stiffener thickness it is possible to treat the entire structure as having isotropic properties of constant stiffness in order to use equation (66). This process was used to determine the W/B of an isogrid stiffened sphere assuming UHM carbon as described above. The resulting W/B is displayed in Figure 38. The W/B is slightly better than beryllium, but LTA flight is not achieved. Note that the bottom of the curve in Figure 38 is curved, not flat like in Figure 37. This is because the compressive strength of the epoxy matrix, as shown in Table 7, is sufficient to prevent material failure

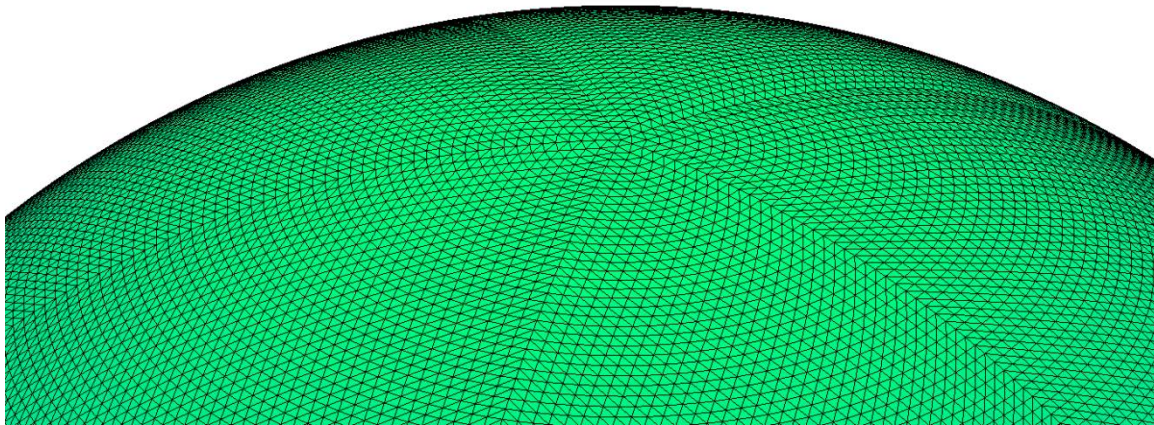
and allow very small  $\bar{t}$ . In this case the  $E/\rho^2$  value is the active material constraint, and changes in stiffness would result in smaller W/B.



The optimal design values for a sphere of  $r_s = 0.33$  m are as follows:  $h = 2.1$  mm,  $t = 0.042$  mm.,  $b = 0.035$  mm, and  $d = 1$  mm. This design would be extremely difficult to build on account of the small size and high number of stiffeners required. In order to arrange triangular stiffeners on the surface of a sphere, a geodesic arrangement must be used. Therefore the geometry used to calculate the geodesic sphere can also be used to calculate the arrangement of isogrid stiffeners. An  $r_s = 0.33$  m with an  $a = 2.4$  mm implies that the major triangle of length 0.347 (where  $a = 1.05 \cdot r_s$ ), would be divided 144 times to get a minor triangle length of 4.1 mm, meaning  $f=144$ . Using equation (28), the number of individual blade type stiffeners (triangle legs) would

be 622,080. The Isogrid Handbook [36] actually mentions that a feasible way to apply an isogrid to a sphere is using the geodesic method described in [37]. A close-up view of the surface of the proposed sphere with  $f=85$  is shown in Figure 39. An  $f=144$  would be even more complex. A feasible method for building such a complex structure would require automation.

**Figure 39: Isogrid Visualization  $f=85$**



After conducting the optimization technique of simultaneously satisfying all three constraints it became apparent that the isogrid did not perform as well as expected. The possible cause was that the optimal design did not have all constraints active. Finding this point required a more robust optimization method. Therefore the isogrid was optimized using the non-linear programming optimization routine called `fmincon`. The program was inconsistent with its results at first because of scaling problems. The variables  $h$ ,  $t_{skins}$ ,  $b$ , and  $d$  were so small that the program's step size tended to overshoot the optimal point and failed to converge on the right value. After properly scaling the problem to make the variables have a magnitude close to unity, `fmincon` consistently converged on a

$W/B=0.81$ . This occurred at  $h=1.4$  mm,  $t_{skin_s}=0.032$  mm,  $b=0.015$  mm, and  $d=1.27$  mm. These values did not lie in the two dimensional design space shown in Figure 38 because not all constraints were active at the optimal point. Only the global buckling constraint, equation (66), was active with a value of -0.01. The negative value indicates that the constraint was satisfied, the magnitude indicates it was just barely satisfied, thus it was an active constraint. The other constraints were inactive with values for the skin buckling of -63 and rib buckling of -73. The negative values indicate the constraints were satisfied, which means the buckling load was not exceeded by the stress. The magnitudes indicate that the skin and stiffeners had thicker cross sections than the minimum required to prevent buckling of the skin or stiffeners, which means these constraints were not active.

Two additional constraints were added to the optimization. These were the requirement that the skin compressive yield strength and stiffener compressive yield strength not be exceeded by the stress in the structure. This resulted in a total of 5 equations and four variables. The problem was not over-constrained, however, as long as no more than four variables were active. It turned out that at the optimal point for each of the isogrid designs only one constraint was ever active, the global buckling constraint, equation (66).



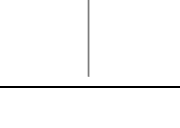
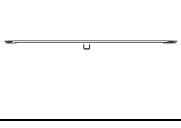
The same optimization was run for pure beryllium resulting in a  $W/B=1.7$ , just as in the method of simultaneously solving constraints. This was the expected result because the compressive strength of beryllium prevented the design from falling below a minimum cross sectional area, which prevented reduction in  $W/B$  using any method of optimization. No particular result was found because there were a range of values for

which a  $W/B=1.7$  could occur, just as shown in Figure 37 using the first optimization method.

The same optimization was run for a sphere with a beryllium skin and a carbon fiber stiffener. A  $W/B=0.79$  was obtained with a geometry of  $h=1.3$  mm,  $t_{skin_s}=0.026$  mm,  $b=0.014$  mm, and  $d=1.2$  mm. This hybrid structure of beryllium and UHM carbon composite combined the higher isotropic stiffness of Beryllium with the higher axial stiffness, lower density, and higher compressive strength of UHM carbon.

The geometry and  $W/B$  of each isogrid design is listed in Table 9. Note the comparatively large value for  $b$  and small value for  $d$  for the beryllium skin/UHM carbon stiffener hybrid structure. This can be explained by the high stiffness in the beryllium skin which did not require a substantial stiffener to be added to prevent skin or global buckling. The skin did require additional area, however, to spread out the stress due to its low compressive yield stress. The UHM carbon epoxy is substantially less dense than the beryllium, which makes it a better material for adding thickness.

**Table 9: Isogrid Results**

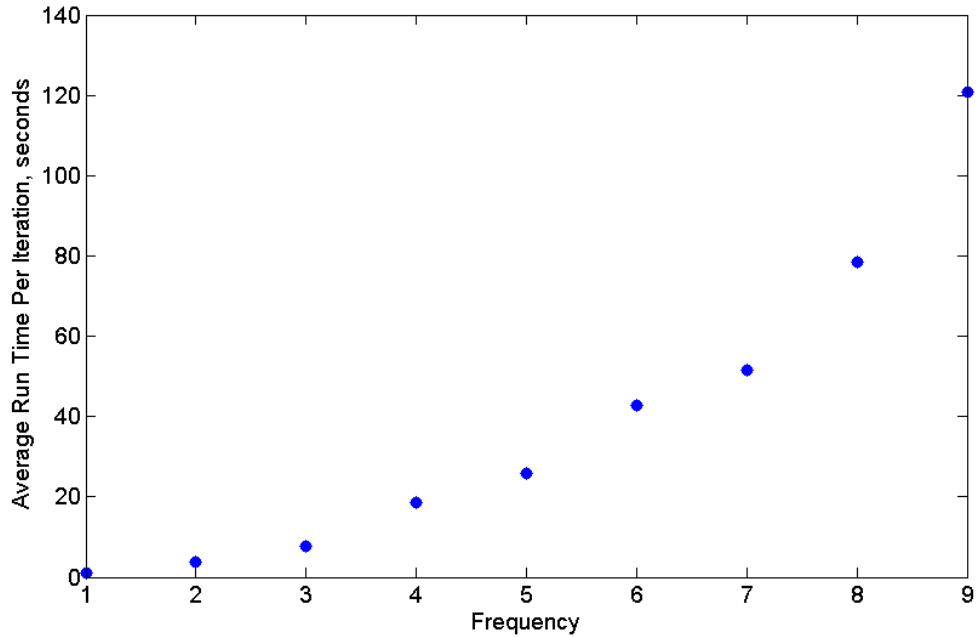
Material	Optimization Method	h	t	b	d	W/B	Diagram
Beryllium	Simultaneous Constraint Satisfaction Non-linear Programming	1.8E-03	3.3E-05	4.8E-05	1.1E-03	1.66	
UHM Carbon Epoxy	Simultaneous Constraint Satisfaction	2.1E-03	4.2E-05	3.5E-05	1.0E-03	1.03	
UHM Carbon Epoxy	Non-linear Programming	1.4E-03	3.2E-05	1.5E-05	1.3E-03	0.81	
Beryllium Skin UHM Carbon Epoxy Stiffeners	Non-linear Programming	1.3E-03	2.6E-05	4.8E-05	1.4E-05	0.79	

#### 4.5 Geodesic Sphere

The geodesic sphere results are given in this section, as well as a description of the design space. The geodesic sphere was evaluated for  $f=1$  through 10. If the optimization showed that higher  $f$  resulted in lower W/B, then higher values of  $f$  would have been investigated. This approach was taken because of the high computational cost of generating and evaluating structures with high numbers of elements. The number of elements in a geodesic structure was equal to the number of edges,  $n_e$ , given by equation (30). The computational cost of the optimization routine depended on  $f$ , with  $f=1$  (30 elements) having an average run time of 1 second and an  $f=9$  (2430 elements) having an average run time of 120 seconds per iteration on an Intel® Core™ i7-2630QM CPU @ 2.00 GHz with 8 MB of RAM. This trend is plotted in Figure 40. The differences in run time were primarily due to the FEA portion of the routine with the large number of

elements at higher frequencies requiring significant computation times. The graph in Figure 40 should be quadratic, which it appears to be, Because  $n_e$  is a function of  $f^2$ .

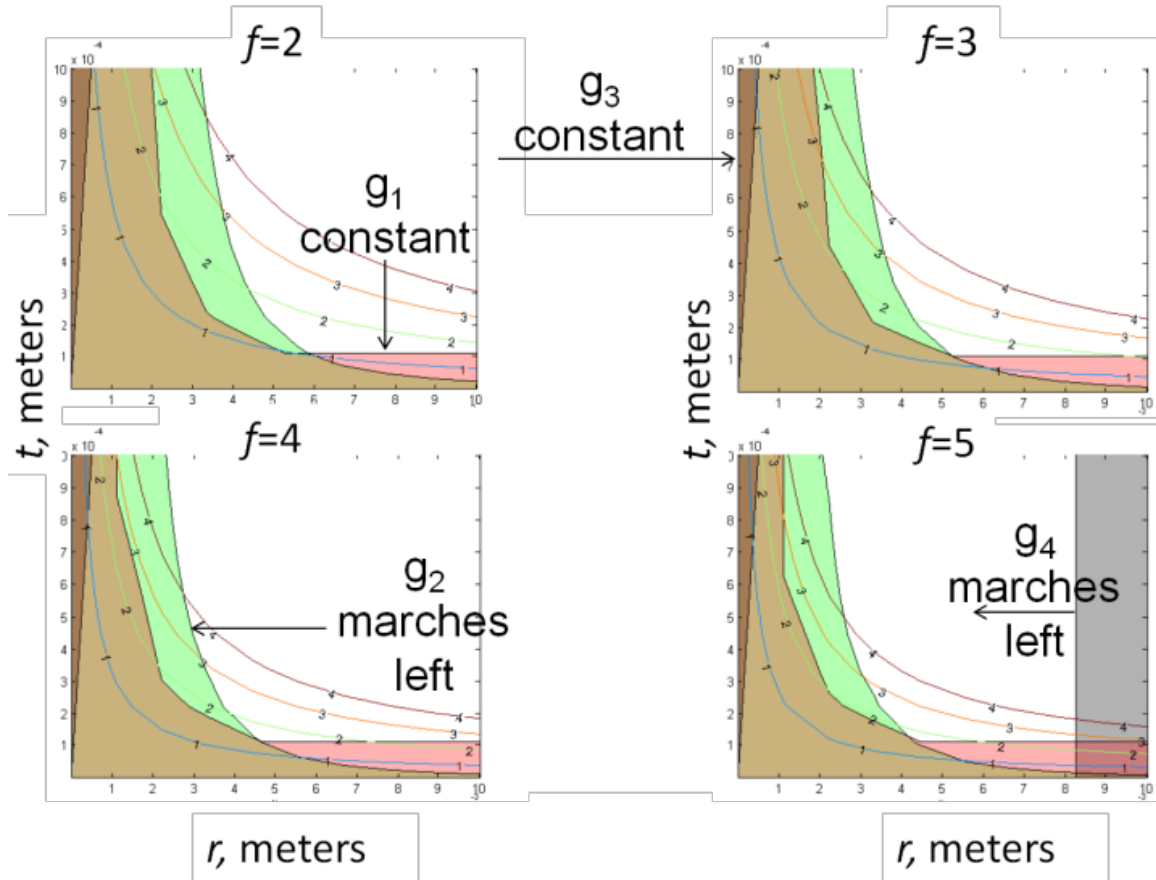
**Figure 40: Effect of Geometric Frequency on Run Time**



It turned out that lower frequencies resulted in lower  $W/B$ , so that no  $f > 10$  was investigated. There are two reasons an  $f=1$  is optimal. The first is minimal structure. At higher frequencies the sphere approaches a solid sphere, whereas low frequencies have more empty space. This can be seen in Figure 41, where the isocost lines (lines of constant cost) which correspond to geodesic frame  $W/B$ , move left with increasing  $f$ . The axes of Figure 41 are the variables  $r_{cb}$  and  $t_{cb}$ . For a given combination of  $r_{cb}$  and  $t_{cb}$ , an increase in  $f$  results in an increase in  $W/B$ . This makes sense because it is equivalent to keeping the cross section of the cylindrical beams constant and increasing total length of the beams (if all members were added together to form one long cylinder). This would

increase overall weight of the structure while keeping buoyancy constant, which would increase  $W/B$ .

Figure 41: Effect of Geometric Frequency on Feasible Design Space



The other reason  $f=1$  is optimal is that the icosahedron is perfectly symmetric, so that every beam has the same stress when loaded evenly. Figure 42 shows the relationship between stress and  $f$ . At higher  $f$  the average stress in all the beams decreases in magnitude, however some members have more stress than others due to asymmetrical loading. The icosahedron ( $f=1$ ) is the structure with the lowest maximum stress in its members because it is a perfectly symmetric structure, so that its maximum stress magnitude is equal to its average stress magnitude. This property of the icosahedron, in

addition to having the lowest structural mass, results in the lowest W/B of any geodesic structure investigated. Note that Figure 42 is a plot of compressive stress, so that all values are negative and a higher compressive stress magnitude is lower on the y axis than a lower compressive stress magnitude. The solid dots indicate maximum stress anywhere in the structure, while the hollow dots indicate mean stress throughout the structure. For the icosahedron, which corresponds to a geodesic sphere with an  $f=1$ , the mean stress equals the maximum stress.

**Figure 42: Effect of Geometric Frequency on  $\sigma$**

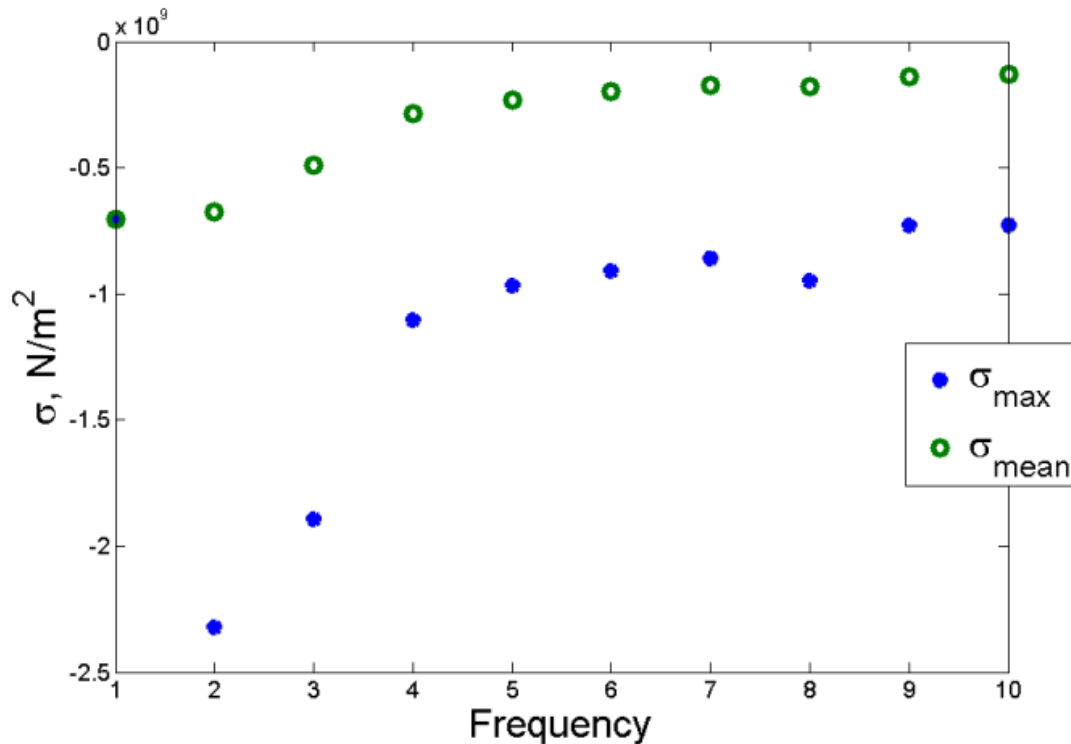


Figure 43 shows the design space for  $f=1$ . White denotes the feasible design space with isocost lines denoting W/Bs of 1 through 4. The constraints  $g_1$ ,  $g_2$  and  $g_3$  are labeled with the infeasible design space shown in color. The constraint  $g_4$  is not pictured due to

being off the right side of the graph. The optimal point shows a  $W/B$  less than 1. The  $g_1$  constraint is pictured in red (brown when it overlaps  $g_2$ ). The  $g_1$  constraint is the requirement for compressive yield strength of the material to exceed the maximum compressive stress in the structure. As would be expected, this constraint is parallel to the isocost lines because cross sectional area is directly related to both weight and stress. If cross sectional area is always exactly sufficient to satisfy  $g_1$ , it will correspond to the same amount of material in the frame, which will correspond to a constant weight. Cross sectional area is a product of the two variables  $r_{cb}$  and  $t_{cb}$ , which are the x and y axes of Figure 43. The advantage of having  $g_1$  be the active constraint is that it allows for flexibility in design. An  $r_{cb}$  anywhere between 4mm and 1cm, as shown on Figure 43, will result in a  $W/B$  for the frame of 0.57. If, for example, the minimum thickness that can be constructed of a pultruded UHM carbon epoxy rod happens to be 0.15 mm, then that thickness can be selected, and the corresponding  $r_{cb}=5$  mm could be used without an increase in  $W/B$ .

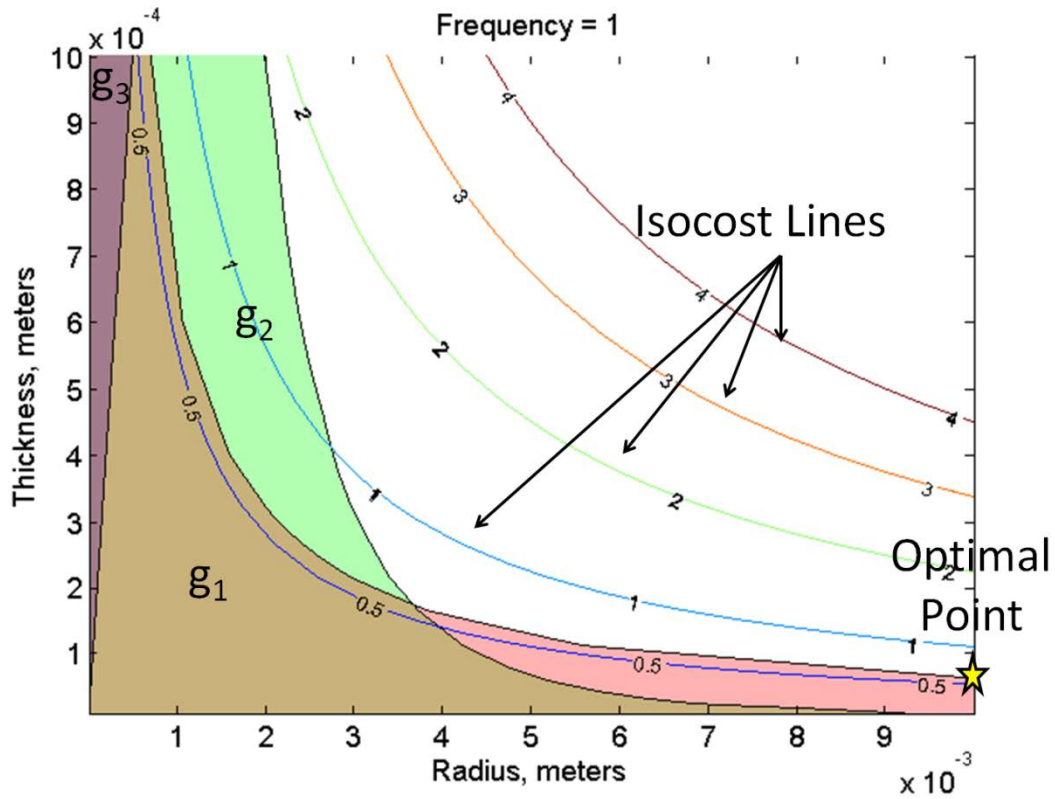
The requirement for the buckling load of the cylindrical beams to exceed the load on any member in the structure is defined by  $g_2$ . The constraint  $g_2$  is optimal at infinite radius and infinitesimal thickness. As can be seen in Figure 43, minimum  $r_{cb}$  is defined by  $g_2$ , and minimum  $t_{cb}$  is defined by  $g_1$ .

The constraint  $g_3$  is the requirement that thickness not exceed half the radius, and so is only active for high thickness and low radius. This can be seen on Figure 43 where  $g_3$  is only active at low radii and high thickness.

The constraint  $g_4$  does not even appear on Figure 43. This is because  $g_4$  sets an upper limit on  $r_{cb}$  as a function of  $f$ . Higher  $f$ s result in more restrictions on  $r_{cb}$ , so that  $g_4$

only becomes a factor in design spaces with high  $f$ . The constraint  $g_4$  is visible in Figure 41 on the graph of  $f=5$ .

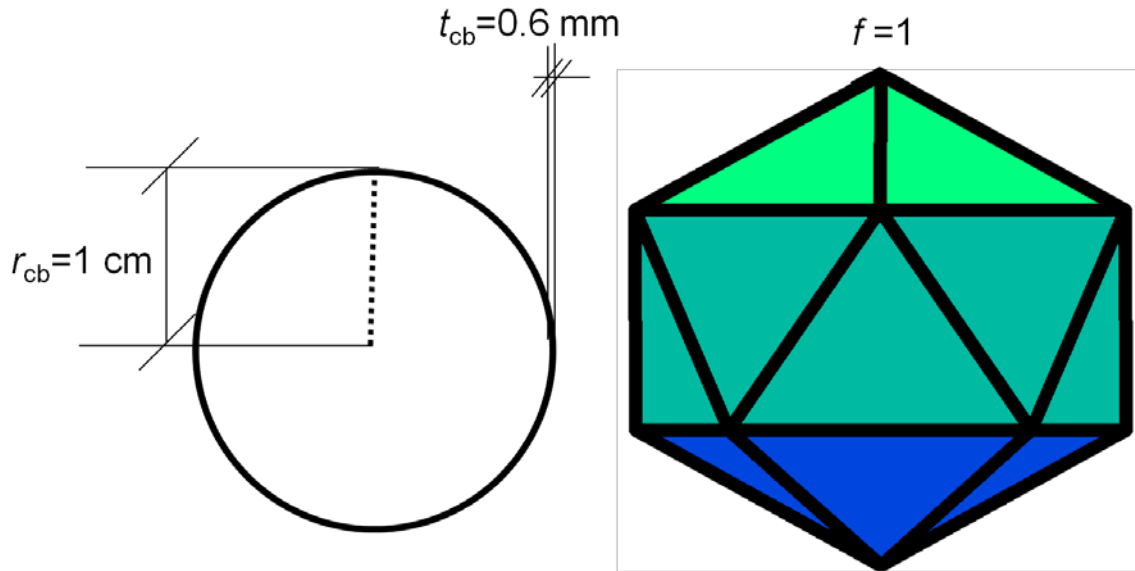
Figure 43: Graphical Representation of Geodesic Sphere Design Space



A minimum  $W/B=0.57$  was attained for the UHM carbon epoxy frame with  $f=1$ ,  $r_{cb} = 1$  cm, and  $t_{cb} = 0.64$  mm for the frame alone as shown in Figure 44. The cross section of a cylindrical tube is shown with the thickness of the cylinder wall scaled proportional to the radius of the cylinder. The icosahedron is also shown with the line thickness scaled proportional to the triangle leg length. The fmincon program proved robust enough for the problem even though it was not designed to handle discrete design variables. Although  $f$  was a discrete design variable, fmincon was usable by rounding  $f$  to

the nearest integer within the subroutines of the optimization routine, as well as rounding the final value of  $f$  at the end of the optimization prior to evaluating it in the cost function.

**Figure 44: Optimal Geometry for  $r_s=0.33$  m Geodesic Sphere**



The skin thickness,  $t_{sk}$ , was not optimized but was assumed to be 5 mm thick Vectran for the purpose of FEA evaluation of a triangular plate under 1.5 times sea level pressure with clamped edges as shown in Figure 45 . It was found that with a thickness of 5mm, a skin with Vectran material properties as shown in Table 6, that the maximum displacement at the center of the skin was 0.59 mm. The maximum stress in the skin was 49 MPa which is far below the maximum strength of Vectran of 3.2 GPa as shown in Table 6. This only occurred on the edges and center of the triangle, whereas the average stress in the skin was below 30 MPa. An optimized skin could be reinforced in the places of greatest stress, so that the average thickness could be designed for a stress of 30 MPa. One of the highest specific tensile strengths in available materials is found in Zylon, with a tensile strength of 5.8 GPa [33]. Assuming the skin thickness of 5 mm and a stress of 30

MPa from the FEA shown in Figure 45, the force/unit length was calculated in the structure by multiplying  $t_{skin}$  by stress. Taking this force/length and dividing by 5.8 GPa gave a minimum skin thickness of 0.0259 mm. This process is shown in equation (84).

$$\sigma_{FEA} \cdot \frac{t_{skin_{FEA}}}{\sigma_y} = t_{skin_{required}} \quad (84)$$

Where:

$t_{skin_{FEA}}$  = skin thickness used in FEA

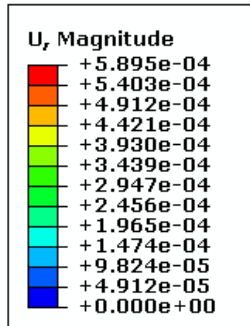
$t_{skin_{required}}$  = minimum required skin thickness

$\sigma_{FEA}$  = Stress calculated by FEA

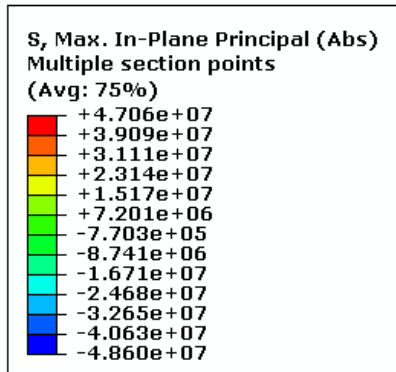
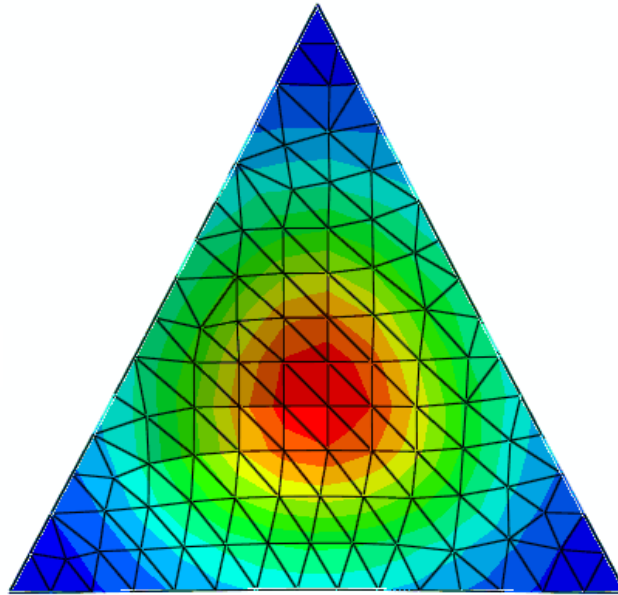
$\sigma_y$  = yield strength of material

The minimum required skin thickness,  $t_{skin_{required}} = 0.0259$  mm, gave a W/B=0.37 for the skin and a W/B=0.94 for the whole structure. The payload capability of a structure with a W/B=0.94 is shown in Figure 46. The mass of the structure would be  $0.94/(1-.94)=15.7$  times the payload. For a diameter of 1 meter, the structure would have a mass of 580 grams and a payload of 37 grams.

Figure 45: FEA of Vectran Triangular Plate With Clamped Edges



Displacement, meters



Stress, Pa

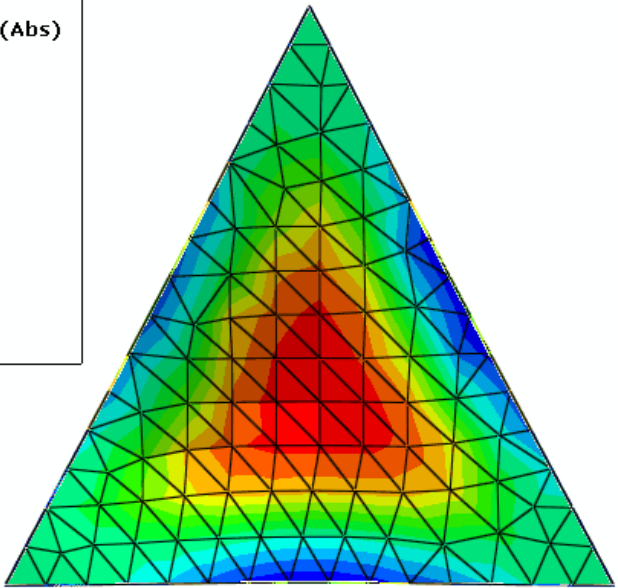
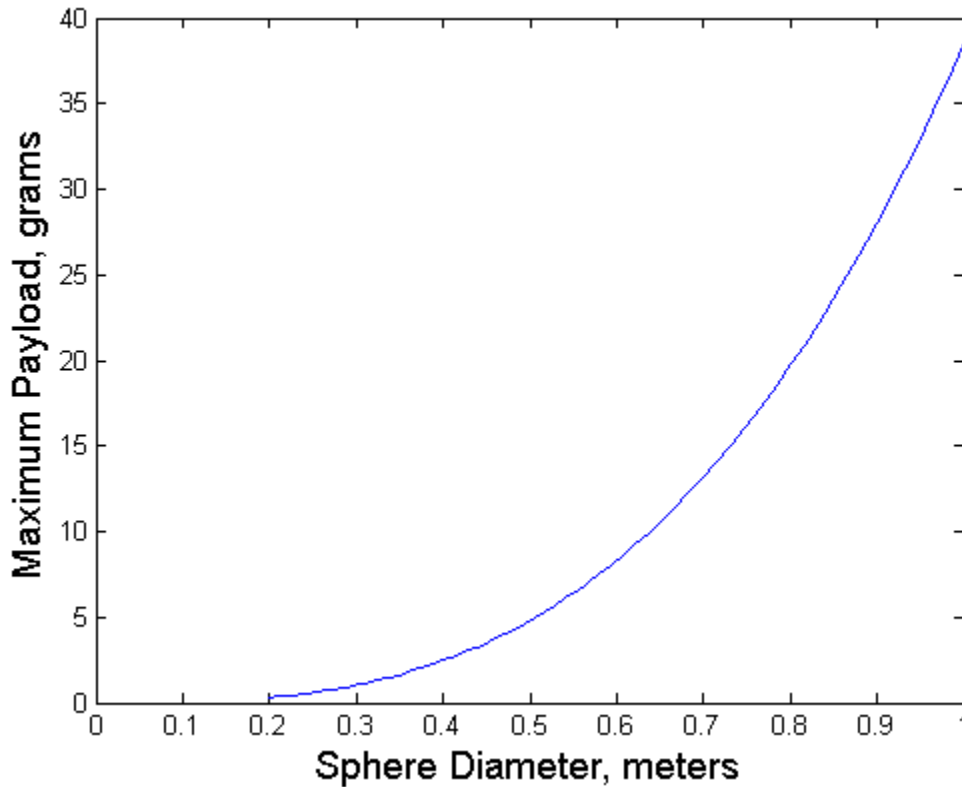


Figure 46: Payload Capability for W/B=0.94



A much more promising material to be used for the membrane is graphene.

Graphene has a tensile strength of 135 GPa, [58], which would enable a skin only 0.001 mm thick. A skin of graphene would have a  $W/B=0.001$ , which would result in an overall  $W/B=0.57$ . This would be an effectively weightless skin. Currently, graphene appears to only be available in small sizes on the order of several centimeters in length, but graphene represents the future potential of material research [58].

Optimization of the skin would be a tradeoff between loss of buoyancy due to decreasing volume ( $V_{gs}$ ) with skin displacement as a function of  $t_{sk}$ , and a decrease in weight as a function of  $t_{sk}$ . The loss in  $V_{gs}$  would occur when the skin displaced inward

due to external pressure, thus reducing the total volume of displaced air contributing to buoyancy. Diffusivity is a measure of the rate at which air could seep through the Mylar membrane. If this occurred the weight of the structure would increase due to added air molecules inside the skin of the structure. This is the same process as a leaking ship that sinks as it takes on water. Optimization of both W/B and diffusivity would be a multi-objective problem in which the diffusivity of air through the reinforced Mylar membrane as a function of  $t_{sk}$  would be considered. The cost function would need to be adjusted to incorporate diffusivity with weighting values assigned to both W/B and diffusivity. A Pareto front could then be constructed to give designers a choice between design goals. A weighting function could also be formed such as maximizing mission time, where mission time is a function of both diffusivity and W/B. A Pareto front is constructed by giving different weights to the objective functions of a multi-objective optimization problem. If one objective is given a lot more weight than the other, the problem will be optimized primarily for that objective alone. If both objectives are given equal weight a solution that is half way between optimizing either objective will be the optimal point.

#### **4.6 Potential Missions**

The vacuum LTA vehicle has the potential to fulfill missions in transportation, surveillance, communications relay, and sensor platforms just like any other LTA vehicle. Whether a vacuum LTA vehicle is suited for any of these missions will depend on each of the design challenges covered previously. The most important hurdle the vacuum structure must clear is becoming LTA. Therefore minimizing W/B is the first priority. Based on W/B, a von Karman Efficiency can be predicted for a theoretical

vehicle that uses a vacuum LTA structure. This von Karman efficiency in turn predicts whether the vehicle could be economically used for transportation.

One of the questions posed early in this study was if there was an ideal altitude at which a vacuum LTA structure could be designed to operate. Figure 47 is a plot of  $W/B$  for a vacuum LTA structure at various altitudes using altitude tables for a standard day [28]. Figure 33 and Figure 47 were created using the Matlab program titled `LTApvalt.m`, Appendix A.11. There are two lines with positive slope in Figure 47. The solid line represents a vacuum LTA structure designed to achieve  $W/B=0.95$  at sea level. At higher altitudes, buoyancy decreases due to decreased air density, and therefore  $W/B$  increases. The dashed line represents the minimum  $W/B$  for vacuum LTA structures specifically designed to resist the pressure of a particular altitude (and no more). The dash dot line represents a vacuum LTA structure designed for 500 meters pressure altitude. This structure would have a lower  $W/B$  than the vacuum LTA structure designed for sea level, but would have a minimum altitude of 500 meters. Descending below 500 meters pressure altitude would cause the structure to exceed its design pressures, which could cause it to fail. Even though the structure designed for 500 meters has a better  $W/B$  at higher altitudes than the structure designed for sea level, the minimum  $W/B$  achievable is by the structure designed for sea level, while it is at sea level. This study shows that the optimal elevation for  $W/B$  is always the lowest available elevation. Therefore the lowest  $W/B$  achievable by a vacuum LTA structure is at sea level. For this reason all structures evaluated during the course of this study were evaluated for the  $W/B$  achievable at sea level standard atmosphere conditions in order to give a best case scenario as well as for the purpose of continuity.

**Figure 47: Effect of Increasing Designed Deployment Elevation**

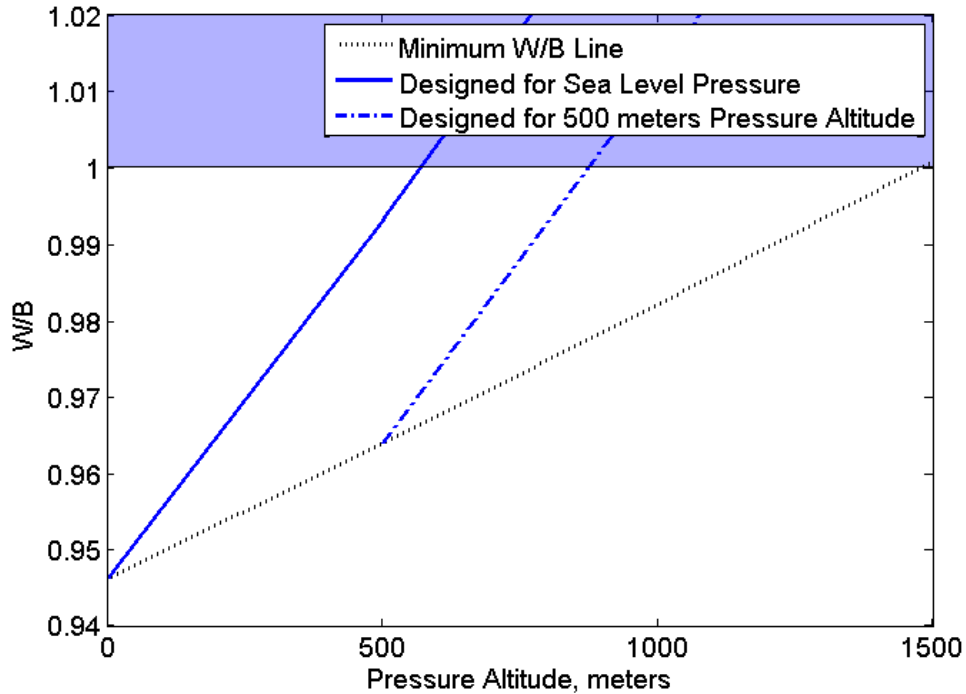
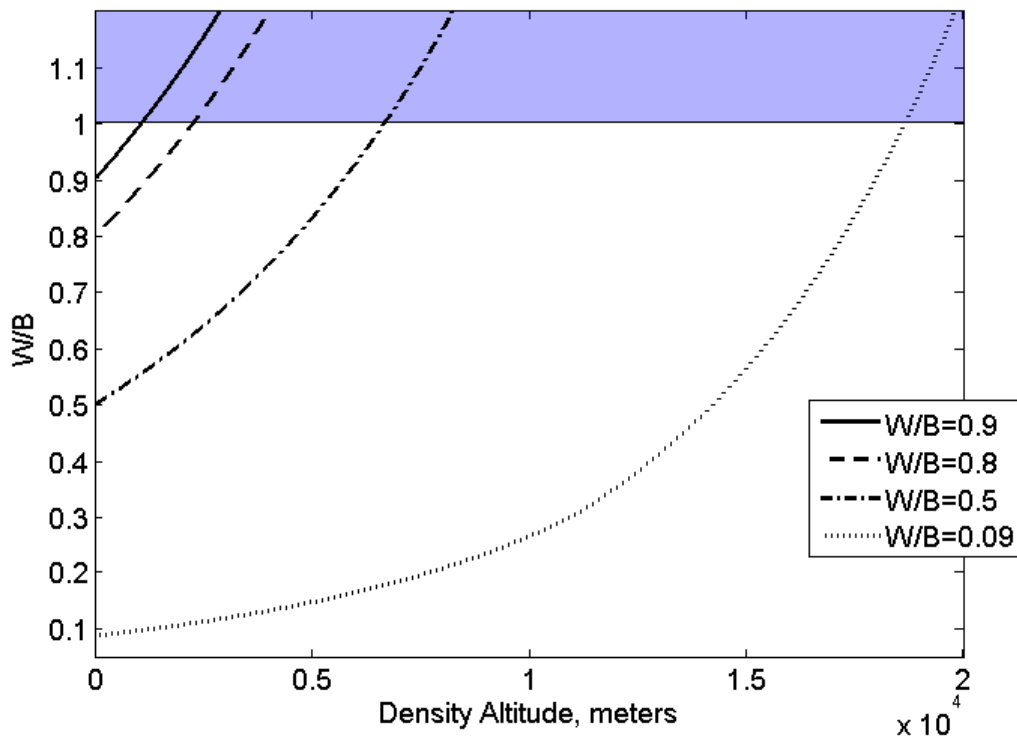


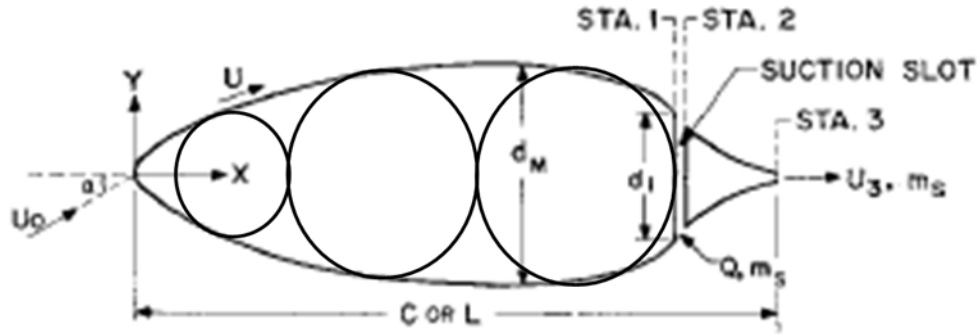
Figure 48 shows the W/B for LTA structures of various W/Bs at sea level. In order for a LTA structure to operate at high altitudes, it must have a low W/B at sea level. The maximum altitude for a given LTA structure is the altitude at which its W/B=1, which is the shaded region on both Figure 47 and Figure 48. This is the main reason cargo LTA vehicles were commonly operated below 1000 feet [9]. Sea level provides the maximum possible buoyancy for any LTA vehicle and is therefore the ideal place to operate cargo oriented LTA vehicles. Without low W/B, any mission requiring high altitude will be impossible for the vacuum LTA vehicle. A W/B=0.09 would be required for a LTA vehicle to operate at the design altitude of the Lockheed HALED [59].

Figure 48: Effect of Altitude on W/B



The von Karman efficiency of the design space for a vacuum LTA vehicle is graphed in Figure 50. This vehicle was assumed to have a  $W/B=0.8$ , an aerodynamic shroud, and a BLC device added that gave the same  $C_D = 0.0169$  as the BLC airship previously evaluated. The assumption was made that the shroud would increase the  $W/B$  to 0.9 and that it would give the spherical vacuum structure a more aerodynamic shape. A conceptual design of this vehicle is shown in Figure 49 and is composed of the Griffith Airfoil used as a body of revolution as described and drawn by Goldschmied [24], with three vacuum LTA spheres inside.

Figure 49: Conceptual Design of BLC Vacuum LTA Vehicle [24]



Von Karman efficiency was plotted for sea level standard day conditions and payload was calculated according to equation (4). The lift for this vehicle was abysmal but the von Karman efficiency was competitive due to low drag. If the drag were increased to the value of a smooth sphere where  $C_D = 0.1$  [51] and the W/B remained at 0.8, the resulting von Karman efficiency of the design space would look like Figure 51. This shows that the increased drag has a significant effect on von Karman efficiency, more so than the ten percent change in W/B. Therefore as long as the shroud could be made light enough for the structure to float, there is a good chance that improving the aerodynamics of the vacuum LTA structure beyond that of a sphere would be beneficial.

Figure 50: von Karman Efficiency at  $W/B=0.8$   $C_D = 0.0169$

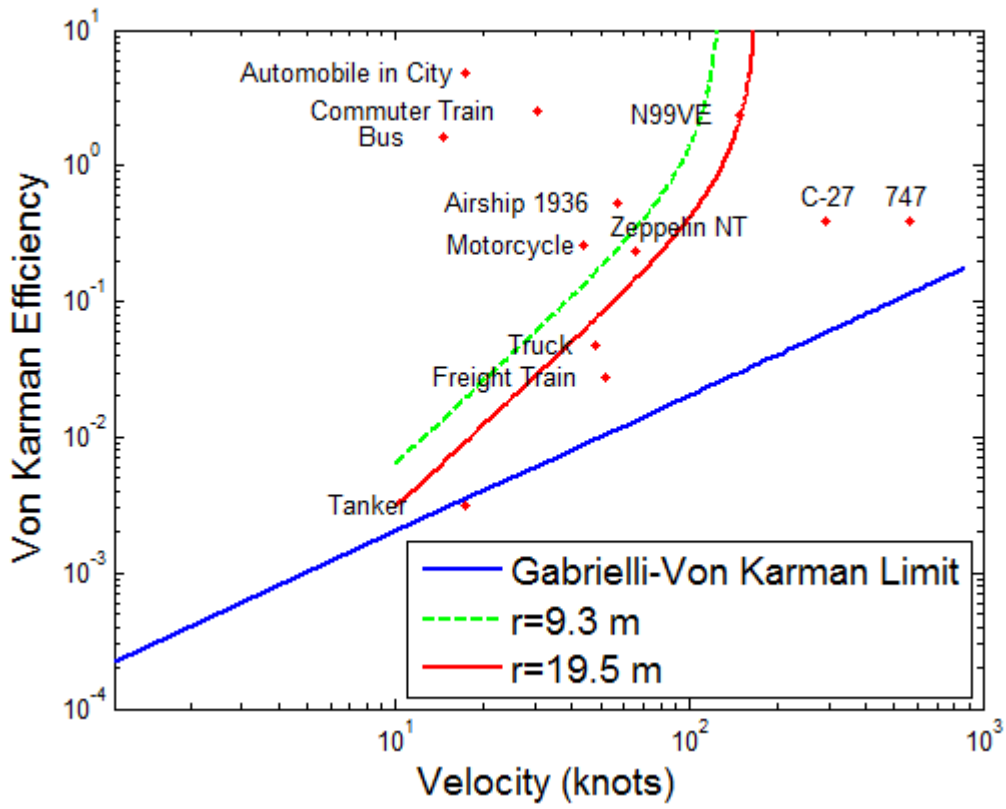
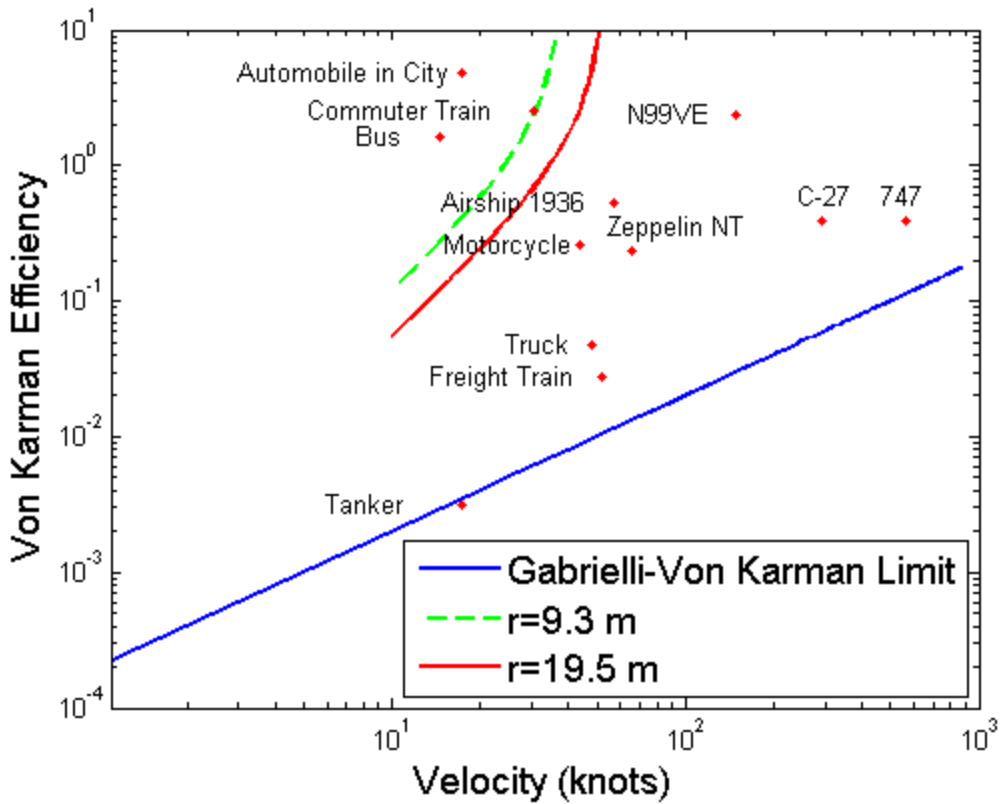


Figure 51: von Karman Efficiency at  $W/B=0.8$   $C_D = 0.1$



The von Karman efficiency of a vacuum LTA vehicle with a  $W/B = 0.8$  or higher at sea level is unlikely to be used for transporting cargo. This conclusion was made based on the altitude limitations shown in Figure 48 and the poor von Karman efficiency shown in Figure 50 and Figure 51. If the BLC can be achieved on the vacuum LTA vehicle it would perform a little worse than the Zeppelin NT for a volume equal to the Zeppelin NT. Any BLC that could be applied to the vacuum LTA vehicle could also be applied to a LTA vehicle relying on a lifting gas, so that the vacuum LTA vehicle is at an efficiency disadvantage to the lifting gas airship. The vacuum LTA vehicle does pose advantages, however, due to its lack of need for a lifting gas, which would enable its use in areas

where shipping helium containers is cost prohibitive, or where the danger of fire due to hydrogen is unacceptable. Therefore it is conceivable that a mission suited for the vacuum LTA vehicle would be one requiring low payload and low altitude, such as an Intelligence, Surveillance, Reconnaissance (ISR) sensor platform for use in the urban environment. These missions could be conducted in hostile environments such as around chemical, biological, or radiation hazards. A geodesic sphere could be constructed so that certain beams were designed to buckle without damage. This would allow intentional buckling of the structure for storage purposes. When the structure needed to be re-deployed it could be inflated to unbuckle the beams, deflated to cause positive buoyancy, and re-deployed. This would require a valve and a vacuum pump, which would require a power source, but not a lifting gas.

A vacuum LTA vehicle with a radius=0.33 meters could fit through a standard door. If it had a W/B=0.8, it would have a total structure mass of 180 grams and be able to carry 46 grams at sea level. Any control systems, fuel, motors and payload would have to weigh less than 46 grams.

#### **4.7 Summary**

The rotating cylinder vehicle was deemed infeasible due to its high energy requirements due to torque drag. Even a rotating cylinder vehicle with a drag torque reduction of 99% below a single rotating cylinder would be infeasible at sea level. At 20 km MSL the RCVLTAV with a 99% drag torque reduction would appear energetically viable, however the requirement to be lifted to altitude by an external aircraft, and the requirement for a 99% reduced drag torque make the RCVLTAV appear infeasible.

A grid stiffened sphere was optimized using two methods, one in which all constraints were simultaneously satisfied, and a non-linear programming optimization problem. Two material arrangements were found with a  $W/B < 1$ . The first was an UHM carbon epoxy sphere with unidirectional stiffeners and a quasi-isotropic skin which was predicted to achieve a  $W/B = 0.81$ . The second was a beryllium skin with UHM carbon fiber unidirectional stiffeners which achieved a  $W/B = 0.79$ . This was achieved with a high geometric frequency of very thin stiffeners, which calls into question the feasibility of construction. Advanced automated methods of composite construction would be required to construct such high frequency geodesic grids.

A geodesic frame composed of cylindrical beams made of UHM carbon fiber was predicted to achieve a  $W/B = 0.57$ . A skin made of Mylar reinforced with Zylon was predicted to add an additional  $W/B = 0.37$ , which would result in an overall  $W/B = 0.94$ . A skin with the properties of graphene would have a  $W/B = 0.001$ , which would result in a vehicle with a  $W/B = 0.57$ . This conclusion was attained using FEA in conjunction with Euler buckling loads and published material properties. Optimization techniques included graphical, the genetic algorithm function in Matlab, and the `fmincon` function in Matlab.

The von Karman efficiency for a vacuum LTA vehicle with a structural  $W/B = 0.8$  was evaluated. The vacuum LTA vehicle could not compete with a lifting gas LTA vehicle as far as efficiency is concerned. It would, however, have the unique property of not relying on a lifting gas. This could make the vacuum LTA vehicle suitable for missions in which efficiency was not of primary concern.

## V. Conclusions and Recommendations

### 5.1 Chapter Overview

This study began by investigating LTA vehicles to include their structure, missions, and design challenges. The buckling of vacuum structures was combined with buoyancy to find several structures that could possibly achieve positive buoyancy using a vacuum. The performance of vehicles using these vacuum structures were then predicted using von Karman Efficiency.

### 5.2 Conclusions of Research

Eight questions were posed in the introduction section. The answers to these questions are available in Table 10.

**Table 10: Research Questions Revisited**

1	Can positive buoyancy be achieved by a structure in air using a vacuum?
	Probably. The grid stiffened structure could possibly achieve positive buoyancy using a vacuum but advanced automated construction of large numbers of stiffeners would be required. The beryllium and UHM carbon epoxy hybrid was the most successful structure investigated, with a predicted $W/B=0.79$ . The geodesic sphere appears to provide a feasible means by which positive buoyancy can be achieved by a vacuum structure using available materials such as UHM carbon tubes and Zylon reinforced skin. A $W/B=0.94$ for the geodesic structure was predicted, with $W/B=0.57$ attributed to the frame, and $W/B=0.37$ attributed to the skin. Graphene would far exceed the material requirements. The rotating cylinder vehicle cannot feasibly achieve positive buoyancy.
2	Is a vacuum LTA structure a feasible platform for any existing missions?
	Yes. The vacuum LTA structure could potentially be used for any mission not requiring a low $W/B$ . This would include any mission suitable for the characteristics of a LTA vehicle that do not require a low von Karman efficiency. A mission that appears particularly suited for the vacuum LTA vehicle is a low altitude sensor platform for ISR in hostile environments.
3	What is the ideal internal pressure of a partial vacuum LTA structure?
	The closer the internal pressure can be to absolute vacuum, the better

	W/B achievable by the vacuum LTA structure.
4	What is the ideal operating altitude of a vacuum LTA structure?
	Sea level is the ideal operating altitude. Any increase in altitude results in an increase in W/B as shown in Figure 47.
5	Are there viable geometric shapes for a vacuum LTA structure?
	The sphere is the best geometric shape, but geodesic approximations to the sphere appear viable as well. The icosahedron actually achieved lower W/B than more complicated geodesic shapes due to its symmetry and sparse structure.
6	Do construction techniques exist which can construct the required geometric shapes?
	The answer appears unlikely for the grid stiffened structure as long as it is made of carbon fibers. It is possible that a dissolvable mandrill could be constructed by a rapid prototype machine and carbon fiber applied using continuously wound fibers using an automated filament winder. The thicknesses of the skin and stiffeners of the grid stiffened structure would also pose a problem unless the structure was made very large. It appears the geodesic sphere could be constructed because the optimal shape is composed of only 30 tubes of reasonable thickness. The challenge to building this structure lies in connecting the tubes at the vertices.
7	What are the critical material properties for a vacuum LTA structure?
	$E$ = Young's modulus of elasticity $\sigma_{cy}$ = compressive yield strength $\rho$ = material density $\sigma_y$ = tensile yield strength A material search can be performed for the geodesic frame or isogrid structure by looking for the maximum $E/\rho^2$ . The $\sigma_{cy}$ must also be checked as it may be the active constraint as in the case of Beryllium. For skin, permeability is important, as well as tensile yield strength $\sigma_y$ and $\rho$ . A material search for the ideal skin could be found by searching for the maximum $\sigma_y/\rho$
8	Do materials exist from which a vacuum LTA structure can be constructed?
	Yes. UHM carbon fiber in an epoxy matrix is the most likely material to be used for the structure. Stiffer fibers and less dense matrix materials are the most promising area for material improvement. For the membrane a high specific strength material like Zylon appears most promising.

### **5.3 Significance of Research**

A vacuum LTA structure would replace the need for a lifting gas. If the risk of fire is unacceptable for a particular mission and helium is unavailable due to reduced supply, vacuum LTA structures may be the best alternative. At the current state of research a vacuum structure can not achieve W/Bs as low as LTA structures containing helium or hydrogen lifting gases. Nevertheless, the construction of a vacuum LTA structure would constitute a technological milestone in structural design. The largest contribution of this research is that it appears to be the first time FEA and non-linear programming optimization techniques have been used to show that a structure can achieve positive buoyancy in air using a vacuum.

### **5.4 Recommendations for Future Research**

Recommended future research includes optimization of the skin for diffusivity and deflection, evaluation of the bending effects due to membrane loads on the sides of the beams using FEA, and experimental analysis of both membrane deflection and global buckling of the icosahedron in order to validate the FEA models. An experiment could be performed on inexpensive materials such as fiberglass in order to perfect construction techniques and validate W/B predictions. This experiment could be performed by building the structure with geometry optimized for the cheaper material, predicting the pressure at which it will fail using the cheaper material, then removing the air from inside of the structure using a vacuum pump while measuring the pressure inside and outside of the structure to observed the critical pressure at which the structure fails. This would be a useful experiment to not only validate the design, but also to overcome the difficulties of

building a structure that can withstand an atmosphere of external pressure without leaking.

A study of the diffusivity of various membranes would be necessary to determine a suitable skin for the geodesic structure. A vacuum LTA vehicle could potentially require less servicing than a helium LTA vehicle because the membrane preventing the equalization of pressure would require pores smaller than the critical diameter of an Oxygen molecule of  $2.8 \text{ \AA}$  as opposed to the critical diameter of a Helium molecule of  $2 \text{ \AA}$ . [1]. The pressure gradient across the membrane is a factor in diffusivity rates as well, so that the relative diffusivity rates between a traditional helium filled membrane which has very little pressure gradient, and the theoretical air displacing vacuum membrane which has an atmosphere pressure gradient are not clear without further study.

An optimization should be performed on the skin where W/B is minimized by varying skin thickness where W/B is affected by volume loss due to membrane displacement and weight due to thickness. The skin will most likely need to be composed of a low diffusivity membrane such as Mylar and a high strength reinforcement cloth such as Zylon.

The rotating cylinder concept could be further studied by researching the torque and  $\Omega_{crit}$  for gap sizes between 1 and 0. Depending on the results of this study rotating cylinder LTA vehicle filled with helium could be evaluated for feasibility using von Karman efficiency.

## Appendix A: Matlab Code

### A.1 Optimization Routine (LTA\_opt.m)

```
%LTA fmincon and Genetic Algorithm
%Written by 1st Lt Justin Mason, Capt Trent Metlen, and Brian Cranston

clear; close all; clc;

%*****
% This program is for MECH 620 optimization of a lighter than air (LTA)
% icosahedron structure.
%
%*****
tic
% Scaling factors for design variables for optimization routine:[f r t]

scaling = [1 1 1];

%% Optimization This section picks which optimization routine to run

% Set upper and lower bounds
ub=[1.1 1e-1 1e-2]./scaling;
lb=[0.9 1e-5 1e-6]./scaling;

% Set initial guess
% Note: this is only used in fmincon
xo = [1 4e-3 2e-4]./scaling;

optimization = 'fmincon';
%optimization = 'genetic';

switch optimization
    case 'genetic'
        %% Genetic Algorithm Optimization
        % Run an optimization routine with a genetic algorithm

        % A = [f r t]
        % g3 = inequality const
        A=[0 -1 .5]; b=0;
        nvars = 3;
        IntCon = 1;
        options=gaoptimset('display','iter','PopulationSize',10);
        [x,fval,exitflag,output,population,scores] = ga(@(x)
        Cost(x,scaling),nvars,A,b,[],[],lb,ub,@(x)
        Constraints(x,scaling,krieking),options);
        x = x.*scaling;

    case 'fmincon'
        %% fmincon Optimization
        % This section runs a fmincon optimization routine
```

```

% A = [f r t]
% g3 = inequality const
A=[0 -1 .5]; b=[0];
options=optimset('algorithm','interior-point','display','iter');
[x,fval] = fmincon(@(x) cost(x,scaling),xo,A,b,[],[],lb,ub,@(x)
Constraints(x,scaling,krieking),options);
x = x.*scaling;
end
toc

```

## A.2 Optimization Sub-Routine: Cost Function (Cost.m)

```

function [ cost ] = Cost( x,scaling)

load geometry1.mat
x=x.*scaling;
f = round(x(1));
rcb = x(2);
tcb = x(3);

% Get sphere parameters
[par] = Sphere_parameters(x);
% Constants
rhocb = par(1);
rhosk = par(2);
rs = par(3);
tsk = par(4);
% lcb = par(5);
% Volume=par(6);
rhoair=1.225; %kg/m^3, density of air
buoyancy=rhoair*Volume;
cost = (rhocb*(60*pi*tcb*rcb*(lcb)*f^2)+Area*tsk*rhosk)/buoyancy;
end

```

## A.3 Optimization Sub-Routine: Sphere Parameters (Sphere\_parameters.m)

```

function [ par ] = Sphere_parameters( x )

% Capt Trent Metlen, 1st Lt Justin Mason, and Brian Cranston

f = round(x(1));
r = x(2);
t = x(3);
load geometry1.mat
%average lengths of geodesic spheres f=1:10 for rs=0.33
store_lcb = [0.3470    0.1926    0.1313    0.0993    0.0797    0.0666
0.0572    0.0501    0.0445    0.0401];
Icb = pi*((r+.5*t)^4-(r-.5*t)^4)/4; %area moment of inertia
rhosk = 1400; %kg/m^3 Ref 1
rs=0.33;

```

```

tsk=1.6e-5;
lcb = store_lcb(round(f));
sigcbcy = 1e9; %UHM carbon epoxy
Ecb = 450e9; %modulus of elaticity UHM carbon epoxy
rhocb = 1522; %density UHM carbon epoxy

par = [rhocb;rhosk;rs;tsk;lcb;Volume;sigcbcy;Ecb;Icb];

end

```

#### A.4 Optimization Sub-Routine: Constraints (Constraints.m)

```

function [ G,ceq ] = Constraints( x,scaling)

x = x.*scaling;
f = round(x(1));
rcb = x(2);
tcb = x(3);

[par] = Sphere_parameters(x);
sigcbcy = par(7);
rs = par(3);
g1= abs(sigmax)-sigcbcy;
[sigmax g2] = Analyze_beam(f,rcb,tcb);
g4= rcb+.5*tcb-sqrt(3)*rs/4/f;
% nonlinear constraints g1, g2, g4
G = [g1; g2 ; g4];

ceq = [];
end

```

#### A.5 Optimization Sub-Routine: Finite Element Program

```

function [ sigmax g2 ] = Analyze_beam(f,r,t)
% 1stLt Justin Mason and Dr Black's Finite Element Class 2012
% Create and analyze FE models from *.dat files

%% Create the *.dat file
Datcreate([round(f) r t])
%% Read *.dat file
model=Datread_beam('icos.dat');
% disp('Read in dat file');

%% Initialize
dof = 6;
N = model.ngrid*dof;
K = zeros(N,N);

%% Generate global K matrix
for element_index = 1 : model.ncbar ;
    EID = model.cbar.EID(element_index);

```

```

PID = model.cbar.PID(EID);
MID = model.pbar.MID(PID);
G1 = model.cbar.G1(EID);
G2 = model.cbar.G2(EID);
A = model.pbar.A(PID);
E = model.mat1.E(MID);
L = sqrt((model.grid.X1(G2)-model.grid.X1(G1))^2+...
          (model.grid.X2(G2)-model.grid.X2(G1))^2+...
          (model.grid.X3(G2)-model.grid.X3(G1))^2);

I_zz=model.pbar.I1(PID);
I_yy=model.pbar.I2(PID);
J=model.pbar.J(PID);
nu=model.mat1.NU(MID);
G=E/(2*(1+nu));
X = A*E/L;
Y_1 = 12*E*I_zz/L^3;
Y_2 = 6*E*I_zz/L^2;
Y_3 = 4*E*I_zz/L;
Y_4 = 2*E*I_zz/L;
Z_1 = 12*E*I_yy/L^3;
Z_2 = 6*E*I_yy/L^2;
Z_3 = 4*E*I_yy/L;
Z_4 = 2*E*I_yy/L;
S = G*J/L;
elemK = [ X      0      0      0      0      0      -X      0      0      0      0      0 ;
          0      Y_1     0      0      0      Y_2     0      -Y_1    0      0      0      Y_2;
          0      0      Z_1     0      -Z_2     0      0      0      -Z_1    0      -Z_2     0 ;
          0      0      0      S      0      0      0      0      0      0      -S      0 ;
          0      0      -Z_2    0      Z_3     0      0      0      Z_2     0      Z_4     0 ;
          0      Y_2     0      0      0      Y_3     0      -Y_2    0      0      0      Y_4;
          -X      0      0      0      0      0      X      0      0      0      0      0 ;
          0      -Y_1    0      0      0      -Y_2    0      Y_1     0      0      0      -Y_2;
          0      0      -Z_1    0      Z_2     0      0      0      Z_1     0      Z_2     0 ;
          0      0      0      -S      0      0      0      0      0      S      0      0 ;
          0      0      -Z_2    0      Z_4     0      0      0      Z_2     0      Z_3     0 ;
          0      Y_2     0      0      0      Y_4     0      -Y_2    0      0      0      Y_3];

%
%
%-----
% Create and apply transformation matrix T
%-----
T=zeros(12,12);
V=[model.cbar.X1(EID);model.cbar.X2(EID);model.cbar.X3(EID)];
Vx=[model.grid.X1(G2)-model.grid.X1(G1),...
    model.grid.X2(G2)-model.grid.X2(G1),...
    model.grid.X3(G2)-model.grid.X3(G1)];
Vy=cross(Vx,V);
Vz=cross(Vz,Vx);
Vx_e=Vx/norm(Vx);
Vy_e=Vy/norm(Vy);
Vz_e=Vz/norm(Vz);
delta = [Vx_e;Vy_e;Vz_e];
z=zeros(3,3);

```

```

T=[delta z z z; z delta z z; z z delta z; z z z delta];
TelemK=T'*elemK*T;

%-----
% Place elemK into global K
%-----
G1_index=find(model.grid.ID==G1);
G2_index=find(model.grid.ID==G2);
dofs1=(G1_index-1)*dof+1:G1_index*dof;
dofs2=(G2_index-1)*dof+1:G2_index*dof;
K(dofs1,dofs1)=K(dofs1,dofs1)+TelemK(1:dof,1:dof);
K(dofs2,dofs1)=K(dofs2,dofs1)+TelemK(dof+1:2*dof,1:dof);
K(dofs1,dofs2)=K(dofs1,dofs2)+TelemK(1:dof,dof+1:2*dof);
K(dofs2,dofs2)=K(dofs2,dofs2)+TelemK(dof+1:2*dof,dof+1:2*dof);

end
% disp('Generated global K matrix');

%% Create force vector
F = zeros(N,1); %Initialize
for ctr = 1 : model.nforce %Cycle through all FORCE1 cards
G_index=find(model.grid.ID==double(model.force.G(ctr)));
fdofs=(G_index-1)*dof+1:(G_index-1)*dof+3;
Vxf=[model.grid.X1(model.force.G2(ctr))-
model.grid.X1(model.force.G1(ctr));...
model.grid.X2(model.force.G2(ctr))-
model.grid.X2(model.force.G1(ctr));...
model.grid.X3(model.force.G2(ctr))-
model.grid.X3(model.force.G1(ctr))];
Vx_e_force=Vxf/norm(Vxf);
%Force vec=model.force.F
F(fdofs)=F(fdofs)+Vx_e_force*model.force.F(ctr);
end
% disp('Created Force vector');

%% GRDSET Cards
% cdof=[];
cdof=false(N,1);
for ctr = 1 : model.ngrdset %Cycle through all grdset cards if
model.ngrdset
for ctr2=1:length(model.grdset.PS)
dim=str2double(model.grdset.PS(ctr2));
cdof((0:(model.ngrid-1))*dof+dim)=true;
% cdof=[cdof,((0:(model.ngrid-1))*dof+dim)];
end
end

%% SPC Cards
for ctr = 1 : model.nspc %Cycle through all SPC1 cards
for dim_ctr=1:length(model.spc.C{ctr})
dim=str2double(model.spc.C{ctr}(dim_ctr));
G_idx=find(model.grid.ID==double(model.spc.G1(ctr)));
cdof((G_idx-1)*dof+dim)=true;
end
end

```

```

end
udof=~cdof;

%% Compute Displacements
D = zeros(N,1); %create displacement vector
D(udof) = K(udof,udof)\F(udof); % solve for displacements
F(cdof) = K(cdof,:)*D; % compute reaction forces
% disp(' ')
% disp('          Displacements')
% disp('Node      T1          T2          T3          R1          R2
R3');
% disp('-----          -----          -----          -----          -----
-----');

for ctr = 1 : model.ngrid
    row = (ctr-1)*dof+1 : ctr*dof;
%   disp(sprintf('%4d  %10.2e  %10.2e  %10.2e  %10.2e  %10.2e
%10.2e',...
%           full(model.grid.ID(ctr)),D(row,1)));
end

% %% Reaction Forces
% disp(' ')
% disp('          Reaction Forces')
% disp('Node      F1          F2          F3          M1          M3
M3');
% disp('-----          -----          -----          -----          -----
-----');
%
% for ctr = 1 : model.ngrid
%   row = (ctr-1)*dof+1 : ctr*dof;
%   disp(sprintf('%4d  %10.2e  %10.2e  %10.2e  %10.2e  %10.2e
%10.2e',...
%           full(model.grid.ID(ctr)),F(row,1)));
% end
%% Stress and strains

% disp(' ')
% disp('          Stress')
% disp('Element      SigmaX          Taut T          Tau Y          Tau
Z');
% disp('-----          -----          -----          -----          -----
');
sig_all = zeros(1,length(model.ncbar));g2 = sig_all;
for ctr=1:model.ncbar
    EID = model.cbar.EID(ctr);
    PID = model.cbar.PID(EID);
    MID = model.pbar.MID(PID);
    G1 = model.cbar.G1(EID);
    G2 = model.cbar.G2(EID);
    A = model.pbar.A(PID);
    E = model.mat1.E(MID);
    L = sqrt((model.grid.X1(G2)-model.grid.X1(G1))^2+...

```

```

        (model.grid.X2(G2)-model.grid.X2(G1))^2+...
        (model.grid.X3(G2)-model.grid.X3(G1))^2);

I_zz=model.pbar.I1(PID);
I_yy=model.pbar.I2(PID);
J=model.pbar.J(PID);
nu=model.mat1.NU(MID);
G=E/(2*(1+nu));

T=zeros(12,12);
V=[model.cbar.X1(EID);model.cbar.X2(EID);model.cbar.X3(EID)];
Vx=[model.grid.X1(G2)-model.grid.X1(G1),...
     model.grid.X2(G2)-model.grid.X2(G1),...
     model.grid.X3(G2)-model.grid.X3(G1)];
Vz=cross(Vx,V);
Vy=cross(Vz,Vx);
Vx_e=Vx/norm(Vx);
Vy_e=Vy/norm(Vy);
Vz_e=Vz/norm(Vz);
delta = [Vx_e;Vy_e;Vz_e];
z=zeros(3,3);
T=[delta z z z; z delta z z; z z delta z; z z z delta];
TelemK=T'*elemK*T;

G1_index=find(model.grid.ID==G1);
G2_index=find(model.grid.ID==G2);
dofs1=(G1_index-1)*dof+1:G1_index*dof;
dofs2=(G2_index-1)*dof+1:G2_index*dof;
D_local1=[D(dofs1);D(dofs2)];
D_local=T*D_local1;
u1=D_local(1,1); v1=D_local(2,1); w1=D_local(3,1);
u2=D_local(7,1); v2=D_local(8,1); w2=D_local(9,1);
theta_x1=D_local(4,1); theta_y1=D_local(5,1); theta_z1=D_local(6,1);
theta_x2=D_local(10,1); theta_y2=D_local(11,1);
theta_z2=D_local(11,1);
x=0;
y=r;
z=0;
cy=2;cz=2;
M_z=E*I_zz*((-6/L^2+12*x/L^3)*v1+(-4/L+6*x/L^2)*theta_z1+(6/L^2-
12*x/L^3)*v2+(-2/L+6*x/L^2)*theta_z2);
V_z=E*I_zz*(12/L^3*v1+6/L^2*theta_z1-12/L^3*v2+6/L^2*theta_z2);
M_y=E*I_yy*((-6/L^2+12*x/L^3)*w1-(-4/L+6*x/L^2)*theta_y1+(6/L^2-
12*x/L^3)*w2-(-2/L+6*x/L^2)*theta_y2);
V_y=E*I_yy*(12/L^3*w1-6/L^2*theta_y1-12/L^3*w2-6/L^2*theta_y2);
Normal=A*E/L*(u2-u1+v2-v1+w2-w1);
Torsion=G*J*(theta_x2-theta_x1+theta_y2-theta_y1+theta_z2-
theta_z1)/L;
Sigma_x=Normal/A-M_z*y/I_zz-M_y*z/I_yy;
Tau_t=Torsion*(r+t/2)/J;
Tau_y=cy*V_y/A;
Tau_z=cz*V_z/A;

```

```

% disp(sprintf('%4d      %10.2e      %10.2e      %10.2e
%10.2e',...
% full(EID),full(Sigma_x),full(Tau_t),full(Tau_y),full(Tau_z));
sig_all(2*ctr-1) = Sigma_x/2-sqrt((Sigma_x/2)^2+Tau_t^2);
% disp(sprintf('sig1      %10.2e',sig_all(2*ctr-1)))
g(2*ctr-1,1) = Sigma_x*A-pi^2*E*I_zz/L/.5;
x=L;
M_z=E*I_zz*((-6/L^2+12*x/L^3)*v1+(-4/L+6*x/L^2)*theta_z1+(6/L^2-
12*x/L^3)*v2+(-2/L+6*x/L^2)*theta_z2);
V_z=E*I_zz*(12/L^3*v1+6/L^2*theta_z1-12/L^3*v2+6/L^2*theta_z2);
M_y=E*I_yy*((-6/L^2+12*x/L^3)*w1-(-4/L+6*x/L^2)*theta_y1+(6/L^2-
12*x/L^3)*w2-(-2/L+6*x/L^2)*theta_y2);
V_y=E*I_yy*(12/L^3*w1-6/L^2*theta_y1-12/L^3*w2-6/L^2*theta_y2);
Normal=A*E/L*(u2-u1+v2-v1+w2-w1);
Torsion=G*J*(theta_x2-theta_x1+theta_y2-theta_y1+theta_z2-
theta_z1)/L;
Sigma_x=Normal/A-M_z*y/I_zz-M_y*z/I_yy;
Tau_t=Torsion*(r+t/2)/J;
Tau_y=cy*V_y/A;
Tau_z=cz*V_z/A;

% disp(sprintf('      %10.2e      %10.2e      %10.2e
%10.2e',...
% full(Sigma_x),full(Tau_t),full(Tau_y),full(Tau_z));

g(2*ctr,1) = -Sigma_x*A-4*pi^2*E*I_zz/L^2;
sig_all(2*ctr) = Sigma_x/2-sqrt((Sigma_x/2)^2+Tau_t^2);
% disp(sprintf('sig1      %10.2e',sig_all(2*ctr)))
end
g2 = max(full(g));
sigmax = min(sig_all);
sigmean=mean(sig_all);

% disp('Done analyze_beam')
end

```

## A.6 Optimization Sub-Routine: Datcreate (Datcreate.m)

```

function [ ] = Datcreate( x )

% 1stLt Justin Mason
% This program writes a .dat file for optimization routine of an
% icosahedron
%% *****
% THIS FUNCTION MUST BE RUN WITHIN LTAgeod.mat
% inputs: rcb, tcb, XYZ, beam, & force
%% Define Constants

[XYZ, beam, force, nV, centroid] = LTAgeod2(x);

f = x(1);
rcb = x(2);
tcb = x(3);

```

```

A = 2*pi*rcb*tcB;      %area
I1 = pi*((rcb+.5*tcB)^4-(rcb-.5*tcB)^4)/4;  %area moment of inertia
I2 = I1;      %area moment of inertia
J = pi*((rcb+.5*tcB)^4-(rcb-.5*tcB)^4)/2;  %torsional constant
E = 450e9;      %modulus of elasticity of carbon epoxy
nu = 0.33;      %poisson's ratio of carbon epoxy
rho = 1522;      %density of carbon epoxy

%% Open file and create header
fileName = 'icos.dat';
fid = fopen(fileName,'w');
header = {'ID ICOS OPT'; 'SOL 101'; 'CEND'; 'TITLE = ICOS OPT';
         'SUBTIT = MECH 620'; 'LABEL = ICOSAHEDRON'; 'SPC = 1';
         'LOAD = 1'; 'DISP = ALL'; 'STRESS = ALL'; 'BEGIN BULK'; };
for ctr = 1:length(header)
    fprintf(fid, strcat(header{ctr}, '\n'));
end

%% Write XYZ Locations

fprintf(fid, '$          Geometry\n');
for ctr = 1:length(XYZ)
    fprintf(fid, 'GRID, %d, , %.4f, %.4f, %.4f\n', XYZ(ctr, :));
end

%% Write beam Conectivity

fprintf(fid, '$          Beam Connectivity\n');
for ctr = 1:length(beam)
    idx = [find(XYZ(:,1)==beam(ctr,2)) find(XYZ(:,1)==beam(ctr,3))];
    v = XYZ(idx,2:4);
    orient = null(v);
    fprintf(fid, 'CBAR, %d, 1, %d, %d, %.4f, %.4f, %.4f\n', beam(ctr, :), orient);
end

%% Write beam and Material Properties

fprintf(fid, '$          Beam and Material Properties\n');
fprintf(fid, 'PBAR, 1, 1, %.10e, %.10e, %.10e, %.10e, 0.0\n', A, I1, I2, J);
fprintf(fid, 'MAT1, 1, %.4f, , %.4f, %.4f\n', E, nu, rho);

%% Write Boundary Conditions

fprintf(fid, '$          Boundary Conditions\n');
fprintf(fid, 'GRDSET, , , , , , , \n');
fprintf(fid, 'SPC1, 1, 123456, %d\n', nV);
for ctr = nV+1:nV+length(centroid)+1
    fprintf(fid, 'SPC1, 1, 123456, %d\n', XYZ(ctr,1));
end
for ctr = 1:length(force)
    fprintf(fid, 'FORCE1, 1, %d, %.4f, %d, %d\n', force(ctr, :));
end

```

```
% fprintf(fid,'FORCE1,1,1,1000,1,2\n');
fprintf(fid,'ENDDATA');
```

```
fclose(fid);
```

```
end
```

## A.7 Optimization Sub-Routine: Geodesic Sphere Geometry (LTAgeod2.m)

```
function [ XYZ, beam, force, nV, centroid] = LTAgeod2( x )
%Capt Trent Metlen 10/10/2012

% Frequency of triangles per major triangle (1 for icosahedron)

f=x(1);
rcb = x(2);
tcb = x(3);
r=0.33;

% Angles in spherical coordinates used to determine icosahedron
vertices
phil=0.4636476090008;
phi2=pi/2-phil;
thetal=2*pi/5;

% Atmospheric Conditions
Pa=1.5*101325; %pascals, sea level pressure (safety factor 1.5)

% Icosahedron vertices in spherical coordinates
Vp=[0 pi/2;0 phil;thetal phil;2*thetal phil;3*thetal phil;4*thetal
phil; 0.5*thetal -phil;1.5*thetal -phil;2.5*thetal -phil;3.5*thetal -
phil; 4.5*thetal -phil;0 -pi/2];

% Basic information on geodesic shape
nV=10*f^2+2; %number of vertices
nt=20*f^2; %number of triangles
ne=30*f^2; %number of edges

% Find all vertices of first 5 major triangles for geoesic sphere
V=[r*ones(nV,1) ones(nV,2)];
V(1,2:3)=Vp(1,:);
V(nV,2:3)=Vp(12,:);
K=1;

for I=1:f
    for J=1:I*5
        V((K+J),2:3)=[(J-1)*2*pi/(I*5) pi/2-I*phi2/f];
    end
    J;
    K=K+J;
end
```

```

% Find all vertices of next 10 major triangles
for I=1:f
    for J=1:5*f
        V((K+J),2:3)=[I*(pi/(5*f))+(2*pi/(5*f))*(J-1) phi1-2*phi1*I/f];
    end
    J;
    K=K+J;
end

% Find all vertices of last 5 major triangles
for I=1:f
    if I<f
        for J=1:5*(f-I)
            V((K+J),2:3)=[pi/5+(2*pi/(5*(f-I)))*(J-1) -pi/2+phi2-phi2*I/f];
        end
        K=K+J;
    end
end

% Convert from spherical coordinates to cartesian coordinates
[x y z]=sph2cart(V(:,2)',V(:,3)',V(:,1)');
leg=sqrt((x(1)-x(2))^2+(y(1)-y(2))^2+(z(1)-z(2))^2);

% Create xyz matrix in cartesian coordinates
XYZ=[x' y' z'];

% Find beam matrix for icosahedron (f=1)
if f==1
    beam=[1 2;1 3;1 4;1 5;1 6;
          2,11;2,7;3,7;3,8;4,8;4,9;5,9;5,10;6,10;6,11;
          7,12;8,12;9,12;10,12;11,12;
          2,3;3,4;4,5;5,6;6,2;
          7,8;8,9;9,10;10,11;11,7];
    n=length(beam);
    beam=[(1:n)' beam];
else %for more complex geodesic spheres (f>1)

    % Split up variables into matrices of planes in sphere
    p=2*f+f+1;
    plane = cell(1,2*f+1);
    plane{1}=[1 XYZ(1,:)];

    if f>1
        cntr=1;
        for I = 2:f
            cntr2=(I-1)*5;
            plane{I}=[(cntr+1:cntr2+cntr)' (XYZ(cntr+1:cntr2+cntr,:))];
            cntr=cntr2+cntr;
        end
    end

    for I=f+1:2*f+1

```

```

    plane{I}=[(cntr+1:cntr+f*5)' XYZ(cntr+1:cntr+f*5,:)];
    cntr=cntr+f*5;
end

J=0;

for I=p-(f-1):p-1
    J=J+1;
    plane{I}=[(cntr+1:cntr+(f-J)*5)' XYZ(cntr+1:cntr+(f-J)*5,:)];
    cntr=cntr+(f-J)*5;
end
plane{p}=[cntr+1 XYZ(end,:)];

% Determine number of planes
[sp1,sp2]=size(plane);

% Create connections between top point and plane 2
cntr=1:cntr;
beam=[1 2;1 3;1 4;1 5;1 6]; %beam=[counter(n) node1 node2]
n=6; %n is the beam counter

% Create connections between coplaner nodes (creates horizontal
rings)
for I=2:sp2-1
    [s1,s2]=size(plane{1,I});
    for J=1:s1-1
        beam(n,:)=[plane{1,I}(J,1) plane{1,I}(J+1,1)];
        n=n+1;
    end
    beam(n,:)=[plane{1,I}(s1,1) plane{1,I}(1,1)];
    n=n+1;
end

% Create connections between planes in triangular cap starting plane
2 to 3
e=[1 1 1]; %edge point connections (points lying on edge of major
triangles)
c=[1 1]; %center point connections (points not lying on edges of
major triangles)

for I=2:f
    % B=matrix of e's and c's where e's=1 and c's=0
    B=[1 zeros(1,I-2) 1 zeros(1,I-2) 1 zeros(1,I-2) 1 zeros(1,I-2)
1 zeros(1,I-2)];
    [s1,s2]=size(B);
    % A=matrix of points where the first row are start points, second row
    % end points, will be added to beam matrix when loop is complete

% first point connections
A=[plane{1,I}(1,1)*e; plane{1,I+1}(end,1) plane{1,I+1}(1,1)
plane{1,I+1}(2,1)];
    cntr=2;
    for J=2:s2

```

```

        if B(J)>0
            m=e;
        else
            m=c;
        end
        % All other point connections on plane
        A=[A(1,:) plane{1,I}(J,1)*m; A(2,:)
(plane{1,I+1}(cntr:cntr+length(m)-1,1))'];
        cntr=cntr+length(m)-1;
    end
    [s4,s3]=size(A);
    % Beam matrix is updated by A matrix
    beam(n:n+s3-1,:)= [A(1,:) A(2,:)'];
    n=n+s3;
end

% Create connections from bottom of triangular cap to bottom of
middle triangles
m=[1 1];

for I=1:f
    s2=f*5;
    A=[plane{1,f+I}(1,1)*m; plane{1,f+I+1}(end,1)
plane{1,f+I+1}(1,1)];
    cntr=1;
    for J=2:s2
        A=[A(1,:) plane{1,f+I}(J,1)*m; A(2,:)
(plane{1,f+I+1}(cntr:cntr+1,1))'];
        cntr=cntr+1;
    end
    [s4,s3]=size(A);
    beam(n:n+s3-1,:)= [A(1,:) A(2,:)'];
    n=n+s3;
end

% Create connections from bottom of middle triangles to last plane
% before endpoint

e=[1];
c=[1 1];

for I=1:f-1
    B=[1 zeros(1,f-I) 1 zeros(1,f-I) 1 zeros(1,f-I) 1 zeros(1,f-I)
1 zeros(1,f-I)];
    [s1,s2]=size(B);
    A=[plane{1,2*f+I}(end,1)*c; plane{1,2*f+I+1}(end,1)
plane{1,2*f+I+1}(1,1)];
    cntr=1;
    for J=1:s2-1
        if B(J)>0
            m=e;
        else
            m=c;
        end
    end
end

```

```

        A=[A(1,:) plane{1,2*f+I}(J,1)*m; A(2,:)
(plane{1,2*f+I+1}(cntr:cntr+length(m)-1,1))'];
        cntr=cntr+length(m)-1;
    end
    [s4,s3]=size(A);
    beam(n:n+s3-1,:)=[A(1,:) ' A(2,:)'];
    n=n+s3;
end

% Create endpoint connections

A=[(plane{1,3*f}(1:5,1))'; (plane{1,3*f+1}(1,1))*[1 1 1 1 1]];
beam(n:n+4,:)=[A(1,:) ' A(2,:)'];
n=n+4;
beam=[(1:n)' beam];
end %ends if loop which was necessary in the case of f=1

% show 3D plot of geodesic sphere
% Plot shape
% tic
% figure();
% for I=1:n
%     plot3(XYZ(beam(I,2:3),1),XYZ(beam(I,2:3),2),XYZ(beam(I,2:3),3))
%
%     hold on
% end
% toc

% Find Triangles Making up Geodesic Sphere
triangle=[0 0 0];
for I=1:nV
    ind = find(beam(:,2)==I);
    ind = [ind;find(beam(:,3)==I)];
    A=beam(ind,:);
    points=unique(A(:,2:3));
    points(find(points==I))=[]; %remove point of interest from list of
points
    for J=1:length(points)
        ind = find(beam(:,2)==points(J));
        ind = [ind;find(beam(:,3)==points(J))];
        A=beam(ind,:);
        points2=unique(A(:,2:3));
        points2(find(points2==I))=[];
        points2(find(points2==points(J)))=[];
        B=zeros(size(points));
        for K=1:length(points2)
            B1=points==points2(K);
            B=B+B1;
        end
        point_vertices=nonzeros(B.*points);
        triangle=[triangle;I*(ones(size(point_vertices)))
points(J)*(ones(size(point_vertices))) point_vertices];
    end
end
end

```

```

triangle(1,:)=[];
for I=1:length(triangle)
    triangle(I,:)=sort(triangle(I,:));
end
triangle=unique(triangle,'rows');

for I=1:length(triangle)
    centroid(I,:)=mean([(XYZ(triangle(I,1),:)); (XYZ(triangle(I,2),:));
(XYZ(triangle(I,3),:))]);
    %calc height of each tetrahedron
    height(I)=norm(centroid(I,:));
    %calc area of each triangular face
    areat(I)=0.5*norm(cross((XYZ(triangle(I,3),:)-
XYZ(triangle(I,1),:)),(XYZ(triangle(I,3),:)-XYZ(triangle(I,2),:))));
end

%calculate volume of each irregular tetrahedron
volumet=(1/3)*areat.*height;
%find volume and surface are of total structure
Volume=sum(volumet);
Area=sum(areat);

% center point index in xyz matrix
cp=nt+nV+1;

%calc force vector force=[point mag pt1 pt2]
force=[0 0 0 0];
for I=1:length(triangle)
    % find vectors for each triangle to determine area
    v12=0.5*(XYZ(triangle(I,2),:)-XYZ(triangle(I,1),:));
    v1c=centroid(I,:)-XYZ(triangle(I,1),:);
    v13=0.5*(XYZ(triangle(I,3),:)-XYZ(triangle(I,1),:));
    v21=0.5*(XYZ(triangle(I,1),:)-XYZ(triangle(I,2),:));
    v2c=centroid(I,:)-XYZ(triangle(I,2),:);
    v23=0.5*(XYZ(triangle(I,3),:)-XYZ(triangle(I,2),:));
    v31=0.5*(XYZ(triangle(I,1),:)-XYZ(triangle(I,3),:));
    v3c=centroid(I,:)-XYZ(triangle(I,3),:);
    v32=0.5*(XYZ(triangle(I,2),:)-XYZ(triangle(I,3),:));
    % Calc force magnitude= Pressure*area where area is 1/2 cross product
    % of vectors (triangle). Two triangles per irregular quadrilateral.
    % Three quadrilaterals make up the total area of a triangular face
    % with the pressure from each quadrilateral acting as an equivalent
    % force at the closest vertex of the triangular face. Each
    % quadrilateral is defined by four points, one at the vertex of the
    % triangular face, one at the centroid, and the remaining two halfway
    % along each edge of the triangular face that meets the vertex at which
    % the force will act.
    magn=Pa*.5*[norm(cross(v12,v1c))+norm(cross(v1c,v13));
norm(cross(v21,v2c))+norm(cross(v2c,v23));
norm(cross(v31,v3c))+norm(cross(v3c,v32))];
    % magnitude =[point mag pt1 pt2]
    % [point of force application, magnitude of force,
    % starting point of force direction, ending point of force
direction]

```

```

    % start point is centroid of triangular face, end point is origin
    force=[force; triangle(I,1) magn(1) nV+I cp;
           triangle(I,2) magn(2) nV+I cp;
           triangle(I,3) magn(3) nV+I cp];
end
force(1,:)=[];

% Find average length of beams
lcbi=zeros(1,length(bean));
for I=1:length(bean)
    lcbi(I)=norm(XYZ(bean(I,3),:)-XYZ(bean(I,2),:));
end
lcb=mean(lcbi);
save geometry1.mat Volume Area lcb;
% Add centroids and origin to xyz matrix
XYZ=[XYZ;centroid;0 0 0];

% Add index to xyz matrix
XYZ=[(1:cp)' XYZ];
End

```

## A.8 Optimization Sub-Routine: .dat File Reader (Datread\_beam.m)

```

function [model] = Datread_beam(filename)
% 1stLt Justin Mason and Dr Black's 2012 Finite Element Class
% Simple *.dat file reader with very limited capabilities
% Warning - use at your own risk!

%% Open file
fid = fopen(filename); %Open dat file

%% Initialize Variables
model.ncrod=0; % Number of rod element cards
model.ncbar=0; % Number of bar element cards
model.ngrid=0; % Number of grid point cards
model.nprod=0; % Number of rod property cards
model.npbar=0; % Number of bar property cards
model.nmat=0; % Number of material cards
model.nspc=0; % Number of single point constraint cards
model.nforce=0; % Number of force cards
model.ngrdset=0; % Number of gridset cards
model.grid.ID = sparse(zeros);
model.grid.CP = sparse(zeros);
model.grid.X1 = sparse(zeros);
model.grid.X2 = sparse(zeros);
model.grid.X3 = sparse(zeros);
model.grid.dof1 = sparse(zeros);
model.grid.dofn = sparse(zeros);
model.crod.EID = sparse(zeros);
model.crod.PID = sparse(zeros);
model.crod.G1 = sparse(zeros);
model.crod.G2 = sparse(zeros);
model.cbar.EID = sparse(zeros);%Beam Elements

```

```

model.cbar.PID = sparse(zeros);
model.cbar.G1 = sparse(zeros);
model.cbar.G2 = sparse(zeros);
model.cbar.X1 = sparse(zeros);
model.cbar.X2 = sparse(zeros);
model.cbar.X3 = sparse(zeros);
model.prod.PID = sparse(zeros);
model.prod.MID = sparse(zeros);
model.prod.A = sparse(zeros);
model.pbar.PID = sparse(zeros);%Beam Mat'l Properties
model.pbar.MID = sparse(zeros);
model.pbar.A = sparse(zeros);
model.pbar.I1 = sparse(zeros);
model.pbar.I2 = sparse(zeros);
model.pbar.J = sparse(zeros);
model.pbar.NSM = sparse(zeros);
model.matl.MID = sparse(zeros);
model.matl.E = sparse(zeros);
model.matl.G = sparse(zeros);
model.matl.NU = sparse(zeros);
dofs=6;

%% Read Executive Control
read_more = true; % initialize logical var to stop reading dat file
first = textscan(fid, '%s',1,'delimiter',' '); %read line up to first
space
first_string = char(first{1,1}); % Transform cell array to character
string
while (read_more) % While logical read_more is true keep reading
    switch first_string % Switch on the first string that is read in

        case {'ID'} %Read in the ID for the job
            cell = textscan(fid, '%[^\n]',1); %read the rest of the line
            model.ID = char(cell{1,1}); %convert to a character string

        case {'SOL'} %Read in the solution sequence to be executed
            cell = textscan(fid, '%u',1); %read the rest of the line
            model.sol = uint32(cell{1,1}); %convert to an integer

        case {'CEND'} %Exit when done with executive control
            read_more = false; %All done reading
            break

    end
    first = textscan(fid, '%s',1,'delimiter',' '); %read line up to the
first space
    first_string = char(first{1,1}); % Transform cell array to character
string
end
% disp('Completed reading Executive Control'); %Dump to the screen an
update

%% Read Case Control

```

```

read_more = true; % initialize logical var to stop reading dat file
first = textscan(fid, '%s',1,'delimiter',' '); %read line up to the
first space
first_string = char(first{1,1}); % Transform cell array to character
string
while (read_more) % While logical read_more is true keep reading
    switch first_string % Switch on the first string that is read in

        case {'TITLE'} %Read in the title
            cell = textscan(fid, '%[^\n]',1); %read the rest of the line
            temp = char(cell{1,1}); %convert to a character string
            model.title = temp(2:length(temp)); %trim off the '='

        case {'SUBTIT'} %Read in subtitle
            cell = textscan(fid, '%[^\n]',1); %read the rest of the line
            temp = char(cell{1,1}); %convert to a character string
            model.subtitle = temp(2:length(temp)); %trim off the '='

        case {'LABEL'} %Read in the label
            cell = textscan(fid, '%[^\n]',1); %read the rest of the line
            temp = char(cell{1,1}); %convert to a character string
            model.label = temp(2:length(temp)); %trim off the '='

        case {'SPC'} %Read in the SPC identifier
            cell = textscan(fid, '%s%u',1); %read the rest of the line
            model.spc_ID = uint32(cell{1,2}); %convert to an integer

        case {'LOAD'} %Read in the Load identifier
            cell = textscan(fid, '%s%u',1); %read the rest of the line
            model.load_ID = uint32(cell{1,2}); %convert to an integer

        case {'DISP'} %Read in the Disp
            cell = textscan(fid, '%[^\n]',1); %read the rest of the line
            temp = char(cell{1,1}); %convert to a character string
            model.disp = temp(2:length(temp)); %trim off the '='

        case {'STRESS'} %Read in the Stress
            cell = textscan(fid, '%[^\n]',1); %read the rest of the line
            temp = char(cell{1,1}); %convert to a character string
            model.stress = temp(2:length(temp)); %trim off the '='

        case {'BEGIN'} %Exit when done with case control
            read_more = false; %All done reading
            break

    end
    first = textscan(fid, '%s',1,'delimiter',' '); % Read line up to the
first space
    first_string = char(first{1,1}); % Transform cell array to character
string
end
% disp('Completed reading Case Control'); %Dump to the screen an
update

```

```

%% Read Bulk Data
read_more = true; % initialize logical var to stop reading dat file
first = textscan(fid, '%s',1,'delimiter',' '); %read line up to the
first comma
first_string = char(first{1,1}); % Transform cell array to character
string
while (read_more) % While logical read_more is true keep reading
    switch first_string % Switch on the first string that is read in

        case {'GRID','EGRID'} %Read in a grid card
            model.ngrid = model.ngrid + 1; %Increment the number of grid
points
            cell = textscan(fid, '%u%u%f%f%f',1,'delimiter',' ',...
                'emptyValue', 0); %read the rest of the line
            GN = uint32(cell{1,1}); %Store grid ID
            model.grid.ID(model.ngrid) = GN;
            model.grid.CP(GN) = uint32(cell{1,2}); %Store
coordinate system
            model.grid.X1(GN) = double(cell{1,3}); %Store 1
coordinate
            model.grid.X2(GN) = double(cell{1,4}); %Store 2
coordinate
            model.grid.X3(GN) = double(cell{1,5}); %Store 3
coordinate
            model.grid.dof1(GN) = (model.ngrid-1)*dofs+1;
            model.grid.dofn(GN) = (model.ngrid)*dofs;

        case {'CROD'}
            model.ncrod = model.ncrod + 1;
            cell = textscan(fid, '%u%u%u%u',1,'delimiter',' ',...
                'emptyValue', 0); %read the rest of the line
            EID = uint32(cell{1,1});
            model.crod.EID(model.ncrod) = EID; %Store element ID
            model.crod.PID(EID) = uint32(cell{1,2}); %Store the
property ID
            model.crod.G1(EID) = uint32(cell{1,3}); %Store grid ID
1
            model.crod.G2(EID) = uint32(cell{1,4}); %Store grid ID
2

        case {'PROD'}
            model.nprod = model.nprod + 1;
            cell = textscan(fid, '%u%u%f',1,'delimiter',' ',...
                'emptyValue', 0); %read the rest of the line
            PID = uint32(cell{1,1});
            model.prod.PID(model.nprod) = PID; %Store property ID
            model.prod.MID(PID) = uint32(cell{1,2}); %Store material ID
            model.prod.A(PID) = double(cell{1,3}); %Store cross sectional
area

        case {'CBAR'}
            model.ncbar = model.ncbar + 1;
            cell = textscan(fid, '%u%u%u%u%f%f%f',1,'delimiter',' ',...

```

```

        'emptyValue', 0); %read the rest of the line
EID = uint32(cell{1,1});
model.cbar.EID(model.ncbar) = EID; %Store element ID
model.cbar.PID(EID) = uint32(cell{1,2}); %Store the
property ID
1 model.cbar.G1(EID) = uint32(cell{1,3}); %Store grid ID
2 model.cbar.G2(EID) = uint32(cell{1,4}); %Store grid ID
model.cbar.X1(EID) = double(cell{1,5}); %Store
component x1 of orientation vector
model.cbar.X2(EID) = double(cell{1,6}); %Store
component x2 of orientation vector
model.cbar.X3(EID) = double(cell{1,7}); %Store
component x3 of orientation vector

case {'PBAR'}
model.npbar = model.npbar + 1;
cell = textscan(fid, '%u%f%f%f%f',1,'delimiter',' ','...',
'emptyValue', 0); %read the rest of the line
PID = uint32(cell{1,1});
model.pbar.PID(model.npbar) = PID; %Store property ID
model.pbar.MID(PID) = uint32(cell{1,2}); %Store material ID
model.pbar.A(PID) = double(cell{1,3}); %Store cross sectional
area
model.pbar.I1(PID) = double(cell{1,4}); %Store 1st moment of
inertia
model.pbar.I2(PID) = double(cell{1,5}); %Store 2st moment of
inertia
model.pbar.J(PID) = double(cell{1,6}); %Store polar moment of
inertia
model.pbar.NSM(PID) = double(cell{1,7}); %Store non-
structural mass

case {'MAT1'}
model.nmat = model.nmat + 1;
cell = textscan(fid, '%u%f%f',1,'delimiter',' ','...',
'emptyValue', 0); %read the rest of the line
MID = uint32(cell{1,1});
model.mat1.MID(model.nmat) = MID; %Store material ID
model.mat1.E(MID) = double(cell{1,2}); %Store Youngs
modulus
model.mat1.G(MID) = double(cell{1,3}); %Store Shear
modulus
model.mat1.NU(MID) = double(cell{1,4}); %Store Poissons
ratio

case {'SPC1'}
model.nspc = model.nspc + 1; %Increment the number of SPC cards
cell = textscan(fid, '%u%s%',1,'delimiter',' ','...',
'emptyValue', 0); %read the rest of the line
model.spc.SID(model.nspc) = uint32(cell{1,1}); %Store SPC ID
model.spc.G1(model.nspc) = uint32(cell{1,3}); %Store node to be
constrained

```

```

        model.spc.C{model.nspc} = char(cell{1,2}); %Store
constrained components

    case {'FORCE1'}
        model.nforce = model.nforce + 1; %Increment the number of
FORCE1 cards
        cell = textscan(fid, '%u%f%u',1,'delimiter',' ','...',
            'emptyValue', 0); %read the rest of the line
        model.force.SID(model.nforce) = uint32(cell{1,1}); %Store
force1 ID
        model.force.G(model.nforce) = uint32(cell{1,2}); %Store node
ID
        model.force.F(model.nforce) = double(cell{1,3}); %Store
magnitude of force
        model.force.G1(model.nforce) = uint32(cell{1,4}); %Store
begining node ID for vector
        model.force.G2(model.nforce) = uint32(cell{1,5}); %Store
ending node for ID

    case {'GRDSET'}
        model.ngrdset = model.ngrdset + 1; %Increment the number of
GRDSET cards
        cell = textscan(fid, '%u%u%u%u%u%u%s',1,'delimiter',' ','...',
            'emptyValue', 0); %read the rest of the line
        model.grdset.CP = uint32(cell{1,2}); %Coordinate system for
grid points
        model.grdset.CD = uint32(cell{1,6}); %Coordinate system for
displacements
        model.grdset.PS = char(cell{1,7});

    case 'ENDDATA' %Exit when done with data
        read_more = false; %All done reading
        break

    end

    first = textscan(fid, '%s',1,'delimiter',' ',''); %read line up to the
first comma
    first_string = char(first{1,1}); % Transform cell array to character
string
    end
    % disp('Completed reading Bulk Data'); %Dump to the screen an update
fclose(fid); %Open dat file
end

```

## A.9 Von Karman Efficiency for Rotating Cylinder (LTAheliumcylinder.m)

```

% LTAheliumcylinder
% Capt Trent Metlen
clc; close all; clear all;
global P rho ro mfact L I E Vs Ms sm d J

%*****atmosphere*****
rho=0.889; % kg/m^3, density of air at 10k feet

```

```

P=1500*70; %Pa, Pressure and 1.5 safety factor
mu=1.68*10^-5; %dynamic viscosity of air
%*****
v=.3; % Poisson's ratio
sm=5.67*10^9;%Pa tensile strength of Hextow lm7
E=2.76*10^11;%2.76*10^11;%modulus of Hextow lm7 *10^11
Ec=1.2*10^10; %transverse modulus elasticity of UHM carbon fiber
ss=128*10^6; %shear strength of AS4 hextow fiber
dhe=0.056; %kg/m^3 density of helium at 10k ft
da=rho-dhe;%density of air - density of helium
d=1522.3945;%density of AS4/3501-6
Vc=0;
mc=0;
K=1;
syms cdi
options = optimset('Display','off'); % Turn off display
options2=optimset('Display','off','Algorithm','trust-region-
reflective'); % Turn off display
mub=.0011; %bearing friction coefficient Ref 5
db=.15;%bearing inner diameter (m) Ref 6
to=.0045;
for J=1:20
    ro=8;%m, radius
    u=10*J;% m/s,tip speed of cylinder
    Re=rho*u.*ro/mu; %reynolds number for cylinder in free flow
    for counter=1:length(Re)
        Rel=Re(counter);
        F=solve(10^((1/(cdi^.5)+.6)/4.07)-Rel*cdi^.5); %find cd
        cd(counter)=double(F); %convert symbolic to numeric
    end
    L=ro*[1:1:10];%m, length of cylinder
    As=4*pi*ro^2;%m^2, area of spherical endcaps
    for I=1:length(L) %find required thickness and mass for each L and
R
        eta=ro/to;
        Kc=0.4233+79.9779*eta^-1-12759.6621*eta^-2+755633.25*eta^-3;
        z=L(I)^2*sqrt(1-v^2)/(ro*to);
        Ac(I)=L(I)*2*pi*(ro);%m^2, surface area of cylinder
        M=0.5*rho*ro*Ac(I)*cd*(u.^2); % Nm, moment
        t(I)=(M*z^(1/4)/(2*pi*ro*Kc*E))^-.5;%m, required thickness of
%cylinder shell due to torque
        to=t(I);
        tl=M/(2*pi*ro^2*ss); %thickness required due to shear stress
        if tl>to %check local buckling condition, is ultimate strength
%greater than local stress?
            t(I)=tl;
        end
        ts(I)=M./(2*pi*((.15+ro)/2)^2*ss);%m, thickness of
spherical endcaps
        Ms(I)=As*ts(I)*d;%kg, mass of sphere
        Vs(I)=4/3*pi*ro^3;%m^3, volume of sphere
        mc(I)=d*Ac(I)*t(I)+Ms(I);%kg, mass of cylinder with spherical
%endcaps
        Vc(I)=L(I)*pi*(ro)^2+Vs(I);%m^3, volume of cylinder with
%spherical endcaps

```

```

    Lr(I)=L(I)/(ro);%Length/radius of cylinder
end

wc=mc*9.8; %N, weight of spherical endcaps
wac=Vc*da*9.8; %N, buoyant force
Lift=wac-wc; %N, lift force of cylinder
fb=.5.*(Lift); %N, bearing load weight of 1/2 payload
Cm=.146./(Re.^2); %Moment Coefficient
    Pb=0.5*mub*db*(u./ro).*fb; %watts, power required due to
bearing friction
    w=u/ro;
    Ps=1/2*Cm.*rho.*u.^3.*ro.^2; %watts, power required to rotate
disks (ends of cylinders)
    Pr=w.*M %watts, power required to rotate cylinder
    Px=0.75*Pr+Ps+Pb; Ref 1 75% power requirement
    U=u/2.5; %m/s, forward velocity omegacrit=2.5 gap size=2*r
    evk=Px./(U*Lift); %von Karman efficiency
    [Evk(J),ind]=min(evk(find(evk>0))); %find minimum evk assuming
no engine weight (so that minimization happens even if vehicle is
infeasible)
    [~,ind]=find(evk==Evk(J))
    Acm(J)=Ac(ind);
    rm(J)=Lr(ind); %length/radius at optimal evk
    tm(J)=t(ind); %thickness at optimal evk
    rom(J)=ro; %radius
    wci(J)=wc(ind); %weight of cylinder at optimal evk
    waci(J)=wac(ind); %buoyancy of cylinder at optimal evk
    omega=w; %rotational velocity required for equilibrium
    Vtip(J)=u; %tip speed of cylinder in m/s
    power(J)=Px(ind); %power required to spin cylinder NM/s
    Ux(J)=U;
end
volc=2*pi*(ro^3).*rm; %(m^3) volume of two cylinders used to compare
to conventional airship

Lift=waci-wci; %lbs buoyancy-weight
Lm=wci./waci;
zeta=43.15*10^6; %(Nm/kg) energy density of fuel

%calculate C27 evk
fuel=4000; %kg of fuel used by C-27J to go 4074 km
dist=4459616; %distance traveled (m)
velocity=150; %m/s cruise speed of C-27J
c27=fuel*zeta*velocity/dist;
ec27=c27/(10000*9.8*velocity);

x=0:max(rom);
    rc=6; %ft radius of cylindrical gondola cabin
    lc=60; %ft length of gondola cabin
    vc=pi*rc^2*lc*0.0283168466 ; %volume of gondola m^3
    mc=11*vc; %mass of gondola (kg) based on 11 kg/m^3 Ref 11
    mb=26*4; %mass of bearings (kg) Ref A 6

figure()

```

```

lambda=2.5; %fineness ratio
Vol=volc(5);
r=((3/4)*Vol/(pi*lambda))^(1/3);
rho10=.406; %(kg/m^3) Ref 2
Dc=.5*rho*Ux.^2.*pi*rc^2*0.012; %Drag of cabin Cd=.012 Ref 12
b=Vol*.85*da*9.8; %(N) buoyancy volume of lifting gas is .85 of total
airship volume
CD=.0169 %CD of BLC airship Ref 3 .0162 +.0007 for tail surfaces
U=(1/1.9438)*[10:10:350]; %m/s, velocity
k=1/.855; %.59 is propeller efficiency with 45% improvement
Ap=pi*(r/4.64)^2; % m^2, propeller area (propeller radius= max
radius/4.64)
range=1852000; % m
zeta=43.15*10^6; %Nm/kg, energy density of Jet A
Px=(k*Dc.^2./(2*rho*Ap*Ux)); %Power required to overcome cabin drag
Lx=2*Lift-(2*1.5*9.8*(power+Px)).*0.00134-
2*9.8*range./Ux.*(power+Px).^3/zeta ; %N, Useful Load of rotating
cylinder LTA vehicle 1.5 kg/hp Ref 6
ex=3*power./(Ux.*Lx); %Von Karman Efficiency of rotating cylinder LTA
%vehicle assuming 33 percent efficient engines
for I=1:length(U)
    t(I)=range/U(I); %time enroute
    D(I)=.5*rho10*U(I)^2*Vol^(2/3)*CD; %(N) Drag
    P(I)=k*sqrt(D(I)^3/(2*rho*Ap)); %Power required
    L(I)=b*.7-(1.7*9.8*P(I))*0.00134-9.8*t(I)*P(I)^3/zeta ; %(N)
useful load assuming 30% structure to useful load ratio and 1.7 kg/hp
engine and ducted fan weight as well as 33% engine efficiency and
energy density of Jet A
    e(I)=3*P(I)/(U(I)*L(I)); %Von Karman efficiency at each velocity
assuming 33 percent efficient engines
end

%von Karman efficiency of zeppelin NT
eznt=147000/(1900*9.8*34);

%Gabrielli von Karman limit
A=.000175;
V=1:10:1010; %mph
effk=A*V;

% Plot von Karman efficiency graph
loglog(V*0.869,effk,U*1.944,e,Ux*1.944,ex,'k',velocity*1.944,ec27,'b*',
34*1.944,eznt,'r.') %mph*.869=knots m/s*1.944=knots
text(velocity*1.6,ec27*1.5,'C-27')
hold on
data3=[ 1/3.9 22.4; 1/.42 75.8; 1/.21 8.9; 1/.4 15.6; 1/.62 7.5;
1/36.68 26.8; 1/1.86 29.5; 1/2.54 290.5; 1/320 8.9; 1/21 24.6];%Ref 1
eff=data3(:,1)./(data3(:,2)*2.237) ;
scatter(data3(:,2)*1.944,data3(:,1),'.') %m/s*1.944=knots
text(1.1*Ux(10)*1.944,ex(10),'Rotating Cyl')
text(1.1*0.8*U(length(U))*1.944,0.8*e(length(U)),'BLC Airship')
text(34*1.6,eznt*1.5,'Zeppelin NT')
text(data3(1,2)/1.5,data3(1,1),'Motorcycle')
text(data3(2,2)/1.2,data3(2,1),'N99VE')
text(data3(3,2)/3,data3(3,1),'Automobile in City')

```

```

text(data3(4,2)/3,data3(4,1),'Commuter Train')
text(data3(5,2),data3(5,1),'Bus')
text(data3(6,2)/2,data3(6,1) ,'Freight Train')
text(data3(7,2)/2,data3(7,1) ,'Airship 1936')
text(data3(8,2)*1.6,data3(8,1)*1.5, '747')
text(data3(9,2)/1.5 ,data3(9,1), 'Tanker')
text(data3(10,2),data3(10,1), 'Truck')

xlabel({'Velocity (knots)'}, 'fontsize',14);
ylabel({'Von Karman Efficiency'}, 'fontsize',14);
legend('Von Karman Limit', 'BLC Airship', 'Rotating Cylinder LTA
Vehicle', 'Location', 'Best')
axis([1 1000 10^-4 10])

```

## A.10 Optimization of Isogrid Stiffened Sphere (LTAsphere.m)

```

%LTAsphere
%Capt Metlen
clc; clear all; close all;

global t r v sc E P rs

% atmospheric properties
da=1.225; %kg/m^3, density of air at sea level
P=1500*101.325 %Pa, air pressure sea level and

% properties of skin
% Dupont E-130-x
E=.5*895e9; %Pa, Young's modulus of elasticity
v=0.3; % Poisson's ratio
sc=1786e6; %Pa, compressive strength
s=3445e6; %Pa, tensile strength
dens=1522; %kg/m^3, density

r=0.33; %m, radius of sphere
ti=linspace(.000001,0.0001,100); %m, thickness of skin
xo=[0.013 0.0001 0.0004]; %initial guess xo=[d b h]
for I=1:length(ti)
t=ti(I);
x(I,:) = fsolve(@LTAspheref,xo, optimset('Display','off')); %solve for
[d b h] at each thickness
xo=x(I,:);
end

d=abs(x(:,1))';
b=abs(x(:,2))';
h=abs(x(:,3))';

a=2*h/sqrt(3); %m, triangle leg length
te=ti+3*d.*b./h; %m, smeared thickness
tes=ti+d.*b./h;
scrit=P*r./(2*te); %stress in cross section due to uniform external
pressure

```

```

te=te-te.*(scrit>sc)+(scrit>sc).*P*r./(2*sc); %make sure material
compressive strength not exceeded. If stress is greater than material
compressive strength then thickness is defined by material compressive
strength, otherwise it is defined by buckling of sphere

alpha=b.*d./(ti.*h);
del=d./ti;
beta=(3*alpha.*(ones(size(del))+del).^2+(ones(size(alpha))+alpha).*(one
s(size(alpha))+alpha.*del.^2)).^5;
ts=ti.*beta./(ones(size(alpha))+alpha); % m, equivalent thickness
Es=E*((ones(size(alpha))+alpha).^2)./beta; % Pa, equivalent stiffness

tsmooth=r*sqrt(P*sqrt(1-v^2)/(.8*E)); % m, thickness required of
unstiffened sphere
scrits=P*r./(2*tsmooth); %stress in unstiffened sphere
tsmooth=tsmooth-tsmooth*(scrits>sc)+(scrits>sc).*P*r./(2*sc) %make sure
material compressive strength not exceeded
A=4*pi.*r^2;% (m^2) area of sphere
V=4/3*pi*(r+.5*te).^3;% m^3, volume of air displaced by sphere
W=A*te*dens*9.8; % N, Weight of skin
bo=9.8*V*da; % N, buoyant force
Mb=W./bo; %weight to buoyancy ratio
L=(bo-W); %(N) Lift
Wsmooth=A*tsmooth*dens*9.8; % N, Weight of skin
Mbsmooth=(Wsmooth./bo); %weight to buoyancy ratio of unstiffened sphere
beam=min(find(a./d>5));

figure();
plot(ti,Mb,ti(length(ti)),Mb(length(ti)), 'r', ti, Mbsmooth);
xlabel('Skin Thickness, meters'); ylabel('W/B')
%title('Weight to Buoyancy Ratio of Be Blade Stiffened Sphere')
legend('Grid Stiffened Sphere', 'Unstiffened Sphere', 'Location', 'Best')
%axis([ti(1) ti(length(ti)) min(Mb)*.8 max(Mb)])

function F = LTAspheref(x)
global t r v sc E P
d=abs(x(1)); %blade depth
b=abs(x(2)); %blade width
h=abs(x(3)); %triangle height
a=2*h/sqrt(3); %triangle leg length
te=t+3*d*b/h; %smearred thickness
tes=t+d*b/h;
scrit=P*r/(2*te); %stress in cross section due to uniform external
pressure

alpha=b*d/(t*h);
del=d/t;
beta=(3*alpha*(1+del)^2+(1+alpha)*(1+alpha*del^2))^5;
ts=t*beta/(1+alpha);
Es=E*((1+alpha)^2)/beta;

if (a/d)>5 % solve buckling of beam for rib buckling
F=[scrit-(pi^2)*E*(b^2)/(12*a^2);P-0.8*Es*ts^2/((r^2)*sqrt(1-
v^2));scrit-5*(pi^2)*E*((t/a)^2)/(12*(1-v^2))];

```

```

Else % solve buckling of plate for rib buckling
    F=[scrit-0.456*(pi^2)*E*(b^2)/(12*(d^2)*(1-v^2));P-
0.8*Es*(ts^2)/((r^2)*sqrt(1-v^2)); scrit-5*(pi^2)*E*((t/a)^2)/(12*(1-
v^2))];
end

```

## A.11 Partial Vacuum Study (LTAspherepv.m)

```

%Capt Metlen
%LTAspherepv
clc; clear; close all;

ni=logspace(0,3,1000);
E=0.0795*450*10^9; %0.0795 from LTAsphere gives E* at optimal stiffener
setting
patm=1.5*1.01325*10^5; %1 bar = 10^5 Pa (N/m2)
mu=.3; %Poisson's ratio
r=1; %m radius of sphere
rhos=1522; %kg/m^3 density of surface of sphere
rhoair=1.225; %kg/m^3 density of air at sea level
for I=1:length(ni)
    n=ni(I);
    t=sqrt((r^2)*(patm-patm/n)*sqrt(1-mu^2)/(0.8*E)); %m thickness of
sphere based on E* gives t*
    ts=t*0.1128; %from LTAsphere gives tsmeared value vs t*
    mb(I)=(rhos*ts^4*pi*r^2+((4/3)*pi*(r-
.5*ts)^3)*rhoair/n)/((4/3)*pi*((r+.5*ts)^3)*rhoair); %mass/buoyancy
ratio

end
figure()
plot(1./ni,mb,1./ni,ones(size(ni))*1,'k:')
xlabel('Fraction of Sea Level Pressure Inside Sphere')
ylabel('W/B')
% title('Effect of Decreasing Internal Pressure')

%%
%M=[pressure/sea level pressure, density/sea level density, elevation
(m)]
M=[1      1      0
0.94211695    0.9529    500
0.887046632    0.9075    1000
0.834542314    0.8638    1500
0.784603997    0.8217    2000
0.737132988    0.7812    2500
0.692030595    0.7423    3000
0.649198125    0.7048    3500
0.608536886    0.6689    4000
0.569948187    0.6343    4500
0.533432026    0.6012    5000
0.498791019    0.5694    5500
0.466025167    0.5389    6000
0.435035776    0.5096    6500

```

```

0.405724155      0.4817  7000
0.377991611      0.4549  7500
0.351838145      0.4292  8000
0.327165063      0.4047  8500
0.303972366      0.3813  9000
0.28206267       0.3589  9500
0.261534666      0.3376 10000
0.24219097       0.3172 10500
0.224031582      0.2978 11000
0.207056501      0.2755 11500
0.191463114      0.2546 12000
0.176955342      0.2354 12500
0.163631878      0.2176 13000
0.151295337      0.2012 13500
0.139847027      0.186   14000
0.129286948      0.172   14500
0.119516408      0.159   15000
0.110535406      0.147   15500
0.102146558      0.1359 16000
0.094468295      0.1256 16500
0.087342709      0.1162 17000
0.080750062      0.1074 17500
0.074660745      0.0993 18000
0.069035283      0.09182 18500
0.063824328      0.08489 19000
0.059018011      0.0785 19500
0.054566987      0.07258 20000
0.039940785      0.05266 22000
0.029331359      0.03832 24000
0.021593881      0.02797 26000
0.01594868       0.02047 28000
0.011813472      0.01503 30000];
for I=1:length(M(:,1))
t3=sqrt((r^2)*(patm*M(I,1))*sqrt(1-mu^2)/(0.8*E));
t3s=t3*0.1128; %from LTAsphere gives tsmeared value vs t*
t2(I)=t3s;
mb2(I)=(rhos*t2(1)*4*pi*r^2)/((4/3)*pi*(r^3)*rhoair*M(I,2));
mb3(I)=(rhos*t3s*4*pi*r^2)/((4/3)*pi*(r^3)*rhoair*M(I,2));
end
figure()
plot(M(1:4,3)*3.28084,mb3(1:4),M(1:4,3)*3.28084,mb2(1:4),M(1:4,3)*3.280
84,ones(4,1)*1,'k:')
xlabel('Pressure Altitude, ft')
ylabel('W/B')
% title('Effect of Increasing Designed Deployment Elevation')
legend('Designed For Specific Altitude','Designed for Sea Level
Pressure')

```

## A.12 Altitude Effect on W/B (LTAspherealt.m)

```

%Capt Metlen LTAspherealt
clc; clear all; close all;

% properties of air

```

```

da=1.225; %kg/m^3, density of air at sea level

%M=[pressure/sea level pressure, density/sea level density, elevation
(m)]
M=[same as Appendix A.11];
diameter=6.5;
index=find(ro*2>diameter);index=index(1);
diameter=ro(index)*2;
mb=[0.9 0.8 0.5 0.25 0.09];
for I=1:5
Mb(:,I)=mb(I)*b(index)./(4/3*pi*(diameter/2)^3*M(:,2)*rho);
end
figure()
plot(M(1:end,3)*3.28084,Mb(1:end,1),M(1:end,3)*3.28084,Mb(1:end,2),M(1:
end,3)*3.28084,Mb(1:end,3),M(1:end,3)*3.28084,Mb(1:end,4),M(1:end,3)*3.
28084,Mb(1:end,5)) %*3.28084 to convert to feet
hold on
[x,y]=meshgrid(0:1000:65000,0.05:0.1:1.4);
cv = [0 0];
[cont,h] = contourf(x,y,y-1,cv);
% Set the figure Renderer to OpenGL, which supports transparency
set(gcf, 'Renderer', 'OpenGL');
% Find all the objects that are children of the contourgroup that have
the FaceAlpha property
a1 = findobj(h, '-property', 'FaceAlpha');
k = .3;
% Change the FaceAlpha property, which will change the
objects'transparency
set(a1, 'FaceAlpha', k, 'FaceColor', [0 0 1]);%red

title('Effect of Altitude on Weight/Buoyancy Ratio')
xlabel('Density Altitude, ft')
ylabel('Weight/Buoyancy Ratio')
legend('W/B=0.9', 'W/B=0.8', 'W/B=0.5', 'W/B=0.25', 'W/B=0.09', 'Location', '
NorthEastOutside')
axis([0,65000,0.05,1.2])

```

### A.13 Optimization of Isogrid (LTaisogrid\_opt.m)

```

%Capt Metlen LTaisogrid_opt
clc; clear all; close all;

%% Optimization

% variables x=[h t b d]
% Set your upper and lower bounds
r=.33; % m, radius of sphere
scaling = [1e-003 1e-005 1e-005 1e-003];
ub=[1e-1 1e-2 1e-2 1e-1]./scaling;
lb=[1e-5 1e-7 1e-7 1e-5]./scaling;

% Set your initial guess

```

```

xo=[ 1.4296e-003  3.2317e-005  1.4625e-005  1.2734e-003]./scaling;

% Atmospheric conditions
rho_air=1.225; % kg/m^3, density of air
P_atm=1500*101.325;% Pa, pressure air

% Material Properties
E=895*10^9; % Pa, skin stiffness UHM carbon fiber
v=0.3; % Poisson's ratio
sc=1786e6; % Pa, compressive strength epoxy
Em=3.5*10^9; % Pa, stiffness epoxy
thetai=0:pi/50:pi; % fiber orientation angles
rho_skin=1522; % kg/m^3, skin density

% calculate angle and Ex of each ply add together to get composite Ex
(Ec)
for I=1:length(thetai)
theta=thetai(I);
theta1=theta+pi/2; %90 degrees
theta2=theta+pi/4; % 45 degrees
theta3=theta+3*pi/4; % -45 degrees
Ec(I)=0.6*(.25*(cos(theta))^4+.25*(cos(theta1))^4+.25*(cos(theta2))^4+.
25*(cos(theta3))^4)*E+.4*Em;
end
E=E*.6+Em*.4;
Eiso=min(Ec); %min fiber stiffness angle for quasi-isotropic [90/+
45/0]s

%% fmincon Optimization
% This section runs a fmincon optimization routine

constants=[r,rho_air,P_atm,E,Eiso,rho_skin,sc,v];
options=optimset('algorithm','interior-point','display','iter');
[x,fval] = fmincon(@(x)
LTAisogrid_cost(x,constants,scaling),xo,[],[],[],[],lb,ub,@(x)
LTAisogrid_constraints(x,constants,scaling),options);

x=x.*scaling
f=2*1.05*.33/(sqrt(3)*x(1)) %calculate geometric frequency
f=round(f)
% Basic information on geodesic shape
nV=10*f^2+2 %number of vertices
nt=20*f^2 %number of triangles
ne=30*f^2 %number of edges

```

#### A.14 Optimization of Isogrid Sub-Routine: (LTAisogrid\_constraints.m)

```

% Capt Metlen
function [ c,ceq ] = LTAisogrid_constraints(x,constants,scaling)
x=x.*scaling;

```

```

%x=[h t b d]
%constants=[r,rho_air,P_atm,E,Eiso,rho_skin,sc,v];
h=x(1);
t=x(2);
b=x(3);
d=x(4);
a=2*h/sqrt(3);
t_bar=t+3*b*d/h;

r=constants(1);
P_atm=constants(3);
E=constants(4);
Eiso=constants(5);
sc=constants(7);
v=constants(8);
bs=(E/Eiso)*b;

alpha=bs*d/(t*h);
del=d/t;
beta=(3*alpha*(1+del)^2+(1+alpha)*(1+alpha*del^2))^0.5;
ts=t*beta/(1+alpha);
Es=Eiso*((1+alpha)^2)/beta;

sigma=P_atm*r/(2*t_bar); %stress in skin and ribs
sc_rib=0.456*(pi^2)*E*((b/d)^2)/(1-v^2); %rib buckling pressure
sc_skin=(5/12)*(pi^2)*Eiso*((t/a)^2)/(1-v^2); %skin crippling pressure
P_crit=0.8*Es*((ts/r)^2)/sqrt(1-v^2); % global sphere buckling

%constraints
g1=sigma-sc;
g2=sigma-sc_rib;
g3=sigma-sc_skin;
g4=P_atm-P_crit;

c = [g1;g2;g3;g4];
ceq = [];
end

```

## A.15 Optimization of Isogrid Sub-Routine: (LTAisogrid\_cost.m)

```

% Capt Metlen
function [ cost ] = LTAisogrid_cost( x,constants,scaling)
x=x.*scaling;
%x=[h t b d]
%constants=[r,rho_air,P,E,Eiso,rho_skin,sc,v];
h=x(1);
t=x(2);
b=x(3);
d=x(4);
r=constants(1);
rho_air=constants(2);
rho_skin=constants(6);
a_s=4*pi*r^2; % m^2, surface area of sphere

```

```
v_s=(4/3)*pi*r^3; % m^3, volume of sphere
t_bar=t+3*b*d/h;
cost = rho_skin*t_bar*a_s/(rho_air*v_s); %W/B of sphere
end
```

## Bibliography

- [1] C. R. Nave, "HyperPhysics," Georgia State University, 2012. [Online]. Available: <http://hyperphysics.phy-astr.gsu.edu/hbase/pbuoy.html>. [Accessed 3 June 2013].
- [2] J. MacDonnell, "Francesco Lana-Terzi, S.J." "The Father of Aeronautics", " [Online]. Available: <http://www.faculty.fairfield.edu/jmac/sj/scientists/lana.htm>. [Accessed 2 April 2013].
- [3] F. Lana de Terzi, "Wikipedia," 1670. [Online]. Available: [http://en.wikipedia.org/wiki/File:Flying\\_boat.png](http://en.wikipedia.org/wiki/File:Flying_boat.png). [Accessed 7 June 2013].
- [4] W. D. Pilkey, *Formulas for Stress, Strain, and Structural Matrices*, 2nd ed., Hoboken: John Wiley and Sons, Inc, 2005.
- [5] A. Akhmeteli, A. Gavrilin, Pennington, Moore, Wilkonson, Bell and Dunbar, "Layered Shell Vacuum Balloons". Tallahassee, FL Patent US 2007/0001053A1, 8 September 2006.
- [6] Defense Industry Daily Staff, "Pocket Gunship: From AC-XX to the MC-27J," 12 July 2012. [Online]. Available: <http://www.defenseindustrydaily.com/AC-XX-Gunship-Lite-A-C-27J-Baby-Spooky-05001/>. [Accessed 4 May 2013].
- [7] D. Mottl, Artist, *Alenia C-27J (Pratica di Mare) edit1*. [Art]. Wikipedia, 2007.
- [8] E. R. Moomey, *Technical Feasibility of Loitering Lighter-Than-Air Near-Space Maneuvering Vehicles*, Air Force Institute of Technology, 2005.
- [9] D. Grossman, "Airships: The Hindenburg and other Zeppelins," 2008. [Online]. Available: <http://www.airships.net/>. [Accessed 1 March 2012].
- [10] Naval Historic Center, "Online Library of Historic Images," Naval Historic Center, 2 December 2002. [Online]. Available: <http://www.history.navy.mil/photos/ac-usn22/z-types/zr1-v.htm>. [Accessed 10 May 2013].
- [11] Aeros, "Aeros," Aeros, 2012. [Online]. Available:

- <http://www.aeroscraft.com/#/aeroscraft/4567337667>. [Accessed 10 May 2013].
- [12] R. Krul, "Krul Antiquarian Books," Nederlandshe Vereeniging van Antiquaren, 2012. [Online]. Available: <http://www.nvva.nl/renekrul/catalogs/0000airships.htm>. [Accessed 10 May 2013].
- [13] G. Khoury and J. Gillett, *Airship Technology*, London: Cambridge University Press, 2012.
- [14] J. Melton, "Airships 101: Rediscovering the Potential of Lighter-Than-Air (LTA)," 2011. [Online]. Available: <http://event.arc.nasa.gov/airships/sites/default/files/pdf/Dr.JohnMelton.pdf>. [Accessed 7 June 2013].
- [15] ZLT Zeppelin Luftschifftechnik GmbH & Co KG, "Zeppelin Flight Adventure," ZLT Zeppelin Luftschifftechnik GmbH & Co KG, 2011. [Online]. Available: <http://www.zepplinflug.de/technik-356.html>. [Accessed 29 April 2013].
- [16] J. Pishock, "Using Lighter Than Air Vehicles as Tactical Communications Relays," Air University, Maxwell Air Force Base, 2007.
- [17] Goodyear, "Goodyear Blimp," Goodyear, 2010. [Online]. Available: <http://www.goodyearblimp.com/cfm/web/blimp/>. [Accessed 10 May 2013].
- [18] NTSB, "Aviation Accident Database and Synopsis," 2013. [Online]. Available: <http://www.nts.gov/aviationquery/index.aspx>. [Accessed 29 April 2013].
- [19] H. Walker, "Mooring and Ground Handling Rigid Airships," in *Proceedings of the Interagency Workshop on Lighter Than Air Vehicles*, Cambridge, 1975.
- [20] J. Bearman, "A Plan For Airships that Might Finally Take Off," 2 July 2012. [Online]. Available: <http://www.popsci.com/technology/article/2012-06/plan-airships-might-finally-take>. [Accessed 10 May 2013].
- [21] DuPont Teijin Films, "Mylar Polyester Film Product Information," [Online]. Available: [http://usa.dupontteijinfilms.com/informationcenter/downloads/Physical\\_And\\_Th](http://usa.dupontteijinfilms.com/informationcenter/downloads/Physical_And_Th)

ermal\_Properties.pdf. [Accessed 28 May 2013].

- [22] M. Lucibella, "Congress Weighs Action to Ease Helium Crisis," *American Physical Society*, vol. 22, no. 4, pp. 1,6, April 2013.
- [23] Inter-American Corporation Helium, "Inter-American Corporation Helium Exploration and Production," Inter-American Corporation Helium, 2013. [Online]. Available: <http://www.helium-corp.com/facts/heliumvalue.html>. [Accessed 29 April 2013].
- [24] F. Goldschmied, "Integrated Hull Design, Boundary-Layer Control, and Propulsion of Submerged Bodies," *AIAA Journal of Hydronautics*, vol. 1, no. 1, 1967.
- [25] G. Leishman, *Principles of Helicopter Aerodynamics*, Cambridge: Cambridge University Press, 2006.
- [26] J. Radtke, "The Energetic Performance of Vehicles," *Neodynamics*, 2008.
- [27] C. McLemore, "Wind-Tunnel Tests of a 1/20 Scale Airship Model," NASA, VA, 1962.
- [28] NOAA; NASA; USAF, "US Standard Atmosphere 1976," NASA, Washington DC, 1976.
- [29] D. Bushnell, "Buckling of Shells-Pitfall for Designers," *AIAA Journal*, vol. 19, no. 9, pp. 1183-1226, 1981.
- [30] V. I. Weingarten and P. Seide, "Buckling of Thin-Walled Doubly Curved Shells," NASA, 1969.
- [31] M. Krenzke, "The Inelastic Buckling Strength of Near-Perfect Deep Spherical Shells With Ideal Boundaries," US Navy, 1963.
- [32] T. T. Metlen and A. N. Palazotto, "Design of a Structure that Achieves Positive Buoyancy in Air Using a Vacuum," 2012.
- [33] "MatWeb," 2013. [Online]. Available: <http://www.matweb.com/>. [Accessed 18

January 2013].

- [34] C. T. Herakovich, *Mechanics of Fibrous Composites*, Danvers, MA: John Wiley & Sons, Inc, 1998.
- [35] D. Richardson, "Estimation of Composite Mechanical Properties," in *Composite Design Materials Workshop*, Bristol, England, 2011.
- [36] R. R. Meyer, M. B. Harmon, O. P. Harwood and J. I. Orlando, "Isogrid Design Handbook," NASA, 1973.
- [37] R. B. Fuller, "Building Construction". United States of America Patent 2,682,235, 12 December 1951.
- [38] Mathworks, *sph2cart.m Help File*, 2005.
- [39] J. Clinton and J. Salsburg, "Geodesic Math," [Online]. Available: <http://mr-fusion.hellblazer.com/pdfs/geodesicmath.pdf>. [Accessed 27 May 2013].
- [40] E. W. Weisstein, "Wolfram MathWorld," [Online]. Available: <http://mathworld.wolfram.com/Pyramid.html>. [Accessed 27 May 2013].
- [41] W. A. Ackel, "Geodesics are Built by Subdividing Regular Solids," 2001. [Online]. Available: <http://home.comcast.net/~wackel/Geometry,GeoSubdivision.html>. [Accessed 04 February 2013].
- [42] M. R. Spiegel, *Mathematical Handbook of Formulas and Tables*, McGraw-Hill Book Co., 1968.
- [43] C. Teunissen, "The Physics of Rotation," 09 July 2012. [Online]. Available: [http://www.cleonis.nl/physics/phys256/angular\\_momentum\\_2.php](http://www.cleonis.nl/physics/phys256/angular_momentum_2.php). [Accessed 25 May 2013].
- [44] E. H. Baker, A. P. Cappelli, L. Kovalevsky, F. L. Rish and R. M. Verette, "Shell Analysis Manual," NASA, Washington D.C., 1968.
- [45] A. Chan, P. Dewey, A. Jameson, C. Liang and A. Smits, "Vortex Suppression and Drag Reduction in the Wake of Counter-Rotating Cylinders," *Cambridge*

*University Press*, 2011.

- [46] The Engineering Toolbox, "The Engineering Toolbox," [Online]. Available: <http://www.engineeringtoolbox.com/index.html>. [Accessed 6 June 2013].
- [47] T. Theodorson and A. Regier, "Experiments on Drag of Revolving Disks, Cylinders and Streamline Roads at High Speeds," NACA, 1944.
- [48] J. Saari, *Thermal analysis of high speed induction machines*, Espoo: Helsinki University of Technology, 1998.
- [49] J. Pyrhönen, T. Jokinen and V. Hrabovcová, *Design of Rotating Electrical Machines*, Chippenham: John Wiley & Sons, 2008.
- [50] Medias, "Medias Product Catalogue," Schaeffler, [Online]. Available: [http://medias.schaeffler.com/medias/hp.ec.br.pr/203\\*20330-MB;b12t8vIkj8fd?clrsb=1](http://medias.schaeffler.com/medias/hp.ec.br.pr/203*20330-MB;b12t8vIkj8fd?clrsb=1). [Accessed 4 May 2013].
- [51] A. Flippone, "Aerodynamic Database," 2004. [Online]. Available: [http://web.archive.org/web/20070715171817/http://aerodyn.org/Drag/tables.html#Top of Page](http://web.archive.org/web/20070715171817/http://aerodyn.org/Drag/tables.html#Top%20of%20Page). [Accessed 12 May 2013].
- [52] T. Metlen and A. Palazotto, "Design of a Structure that Achieves Positive Buoyancy in Air Using a Vacuum," in *AIAA, SDM Conference*, Boston, 2013.
- [53] J. Mason and J. Black, *Analyze\_beam.m*, Dayton: AFIT, 2013.
- [54] J. Mason and J. Black, *Datcreate.m*, Dayton: AFIT, 2013.
- [55] J. Mason and J. Black, *Datread\_beam.m*, Dayton: AFIT, 2013.
- [56] Mathworks, *fmincon*, Mathworks, 2010.
- [57] Air BP Ltd, "Air BP," 2000. [Online]. Available: [http://en.wikipedia.org/wiki/Aviation\\_fuel#Energy\\_content](http://en.wikipedia.org/wiki/Aviation_fuel#Energy_content). [Accessed 4 May 2013].

- [58] G. Tsoukleri, J. Parthenios, K. Papagelis, R. Jalil, A. C. Ferrari, A. K. Geim, K. Novoselov and C. Galiotis, "Subjecting a Graphene Monolayer to Tension and Compression," *Small*, vol. 5, no. 21, pp. 2397-2402, 2009.
- [59] Lockheed Martin, "Lockheed Martin," [Online]. Available: <http://www.lockheedmartin.com/us/products/lighter-than-air-vehicles/haa.html>. [Accessed 2 June 2013].
- [60] Sigma Aldrich, [Online]. Available: <http://www.sigmaaldrich.com/chemistry/chemical-synthesis/learning-center/technical-bulletins/al-1430/molecular-sieves.html>. [Accessed 3 January 2013].
- [61] "sci-toys," [Online]. Available: <http://sci-toys.com/scitoys/scitoys/mathematics/dome/dome.html>. [Accessed 28 January 2013].
- [62] C. Mazza, "The Effects of Selected Modern Technological Concepts on the Performance and Handling Characteristics of LTA Vehicles," in *Interagency Workshop on Lighter Than Air Vehicles*, Cambridge, 1975.
- [63] W. A. Althoff, *Sky Ships: A History of the Airship in the United States Navy*, Orion Books, 1998.
- [64] Alenia Aermacchi, "Alenia Aermacchi - A Finmeccanica Company," 2013. [Online]. Available: <http://www.alenia.com/c-27j-spartan-tactical-transport-aircraft>. [Accessed 10 May 2013].
- [65] R. B. Fette and M. F. Sovinski, "Vectran Fiber Time-Dependent Behavior and Additional Static Loading Properties," NASA, Greenbelt, 2004.

<b>REPORT DOCUMENTATION PAGE</b>				<i>Form Approved</i> <i>OMB No. 074-0188</i>	
<p>The public reporting burden for this collection of information is estimated to average 1 hour per response, including the time for reviewing instructions, searching existing data sources, gathering and maintaining the data needed, and completing and reviewing the collection of information. Send comments regarding this burden estimate or any other aspect of the collection of information, including suggestions for reducing this burden to Department of Defense, Washington Headquarters Services, Directorate for Information Operations and Reports (0704-0188), 1215 Jefferson Davis Highway, Suite 1204, Arlington, VA 22202-4302. Respondents should be aware that notwithstanding any other provision of law, no person shall be subject to any penalty for failing to comply with a collection of information if it does not display a currently valid OMB control number.</p> <p><b>PLEASE DO NOT RETURN YOUR FORM TO THE ABOVE ADDRESS.</b></p>					
1. REPORT DATE (DD-MM-YYYY) 13 Jun 2013		2. REPORT TYPE Master's Thesis		3. DATES COVERED (From - To) 22 Aug 2011 - 13 Jun 2013	
4. TITLE AND SUBTITLE Design of a Lighter Than Air Vehicle That Achieves Positive Buoyancy in Air Using a Vacuum				5a. CONTRACT NUMBER	
				5b. GRANT NUMBER	
				5c. PROGRAM ELEMENT NUMBER	
6. AUTHOR(S) Metlen, Trent, Captain, USMC				5d. PROJECT NUMBER 736 /239	
				5e. TASK NUMBER	
				5f. WORK UNIT NUMBER	
7. PERFORMING ORGANIZATION NAMES(S) AND ADDRESS(S) Air Force Institute of Technology Graduate School of Engineering and Management (AFIT/EN) 2950 Hobson Way, Building 640 WPAFB OH 45433				8. PERFORMING ORGANIZATION REPORT NUMBER AFIT-ENY-13-J-02	
9. SPONSORING/MONITORING AGENCY NAME(S) AND ADDRESS(ES) Matthew Johnson                      David Stargel CEO Aerovar                              AFOSR/RTA 3021 Holmes Avenue South,        875 N. Randolph Street #304    Suite 325, Room 3112 Minneapolis, MN 55408              Arlington VA, 22203-1768 (612) 607-3651                              (703) 696-6961 (DSN 426-)				10. SPONSOR/MONITOR'S ACRONYM(S) AFOSR/RTA	
				11. SPONSOR/MONITOR'S REPORT NUMBER(S)	
12. DISTRIBUTION/AVAILABILITY STATEMENT APPROVED FOR PUBLIC RELEASE; DISTRIBUTION UNLIMITED.					
13. SUPPLEMENTARY NOTES					
14. ABSTRACT Three designs for a Lighter Than Air (LTA) structure that achieve positive buoyancy using a vacuum in place of a lifting gas were proposed and evaluated. The ratio of structure weight to the weight of displaced air was termed Weight/Buoyant Force (W/B) where a W/B<1 corresponds to positive buoyancy. Two methods of geometrically stiffening a sphere were investigated and their W/B evaluated. A thin shelled sphere of beryllium stiffened with an isogrid of blade type stiffeners using Ultra High Modulus (UHM) carbon epoxy was predicted to give a W/B=0.79. A geodesic sphere composed of a frame of cylindrical, UHM, carbon epoxy, pultruded rods with a thin external membrane was evaluated using Finite Element Analysis. A W/B=0.57 was calculated for the frame. The skin was predicted to add 0.37 to the W/B if Zylon was used to reinforce a Mylar membrane, which resulted in a predicted structure W/B=0.94. These structures were optimized using a non-linear programming optimization routine in Matlab. A unique LTA vehicle concept composed of twin counter-rotating cylinders that made use of a virtual elliptical body to reduce drag and maintain structural integrity with a vacuum was also investigated and found to be infeasible.					
15. SUBJECT TERMS Vacuum, Lighter Than Air, Buckling, Optimization, Geodesic Sphere					
16. SECURITY CLASSIFICATION OF:			17. LIMITATION OF ABSTRACT	18. NUMBER OF PAGES	19a. NAME OF RESPONSIBLE PERSON
a. REPORT	b. ABSTRACT	c. THIS PAGE			Dr. Anthony Palazotto (ENY)
U	U	U	UU	188	19b. TELEPHONE NUMBER (Include area code) (937) 255-3636, x4599 (Anthony.palazotto@afit.edu)